1997

Nonlinear response of superconductors to alternating fields and currents

Jason R. McDonald
Iowa State University

INFORMATION TO USERS

This manuscript has been reproduced from the microfilm master. UMI films the text directly from the original or copy submitted. Thus, some thesis and dissertation copies are in typewriter face, while others may be from any type of computer printer.

The quality of this reproduction is dependent upon the quality of the copy submitted. Broken or indistinct print, colored or poor quality illustrations and photographs, print bleedthrough, substandard margins, and improper alignment can adversely affect reproduction.

In the unlikely event that the author did not send UMI a complete manuscript and there are missing pages, these will be noted. Also, if unauthorized copyright material had to be removed, a note will indicate the deletion.

Oversize materials (e.g., maps, drawings, charts) are reproduced by sectioning the original, beginning at the upper left-hand corner and continuing from left to right in equal sections with small overlaps. Each original is also photographed in one exposure and is included in reduced form at the back of the book.

Photographs included in the original manuscript have been reproduced xerographically in this copy. Higher quality 6" x 9" black and white photographic prints are available for any photographs or illustrations appearing in this copy for an additional charge. Contact UMI directly to order.

UMI

A Bell & Howell Information Company
300 North Zeeb Road, Ann Arbor MI 48106-1346 USA
313/761-4700 800/521-0600

Nonlinear response of superconductors to alternating fields and currents

by

Jason R. McDonald

A dissertation submitted to the graduate faculty

in partial fulfillment of the requirements for the degree of

DOCTOR OF PHILOSOPHY

Major: Condensed Matter Physics

Major Professor: John R. Clem

Iowa State University

Ames, Iowa

1997

Graduate College
Iowa State University

This is to certify that the Doctoral dissertation of

Jason R. McDonald

has met the dissertation requirements of Iowa State University

Signature was redacted for privacy.

Committee Member

Signature was redacted for privacy.

Committee Member

Signature was redacted for privacy.

Committee Member

Signature was redacted for privacy.

Committee Member

Signature was redacted for privacy.

Major Professor

Signature was redacted for privacy.

For the Major Program

Signature was redacted for privacy.

For the Graduate College

TABLE OF CONTENTS

LIST OF TABLES

LIST OF FIGURES

1 INTRODUCTION

1.1 Brief historical review of superconductivity

Superconductivity was discovered by Kamerlingh Onnes in 1911 [Kamerlingh Onnes, 1911]. He observed that the electrical resistance of certain metals vanished at a finite temperature T_c (see Fig. 1.1), which was characteristic of the particular metal. Perfect conductivity is one of the characteristic features of the superconducting state. A second important feature, perfect diamagnetism (see Fig. 1.2), was discovered by Meissner and Ochsenfeld in 1933 [Meissner and Ochsenfeld, 1933]. A phenomenological explanation of these two effects was provided in 1935 by the London brothers [London, 1935]. They proposed two equations relating the electric and magnetic fields to the current density flowing in a superconductor,

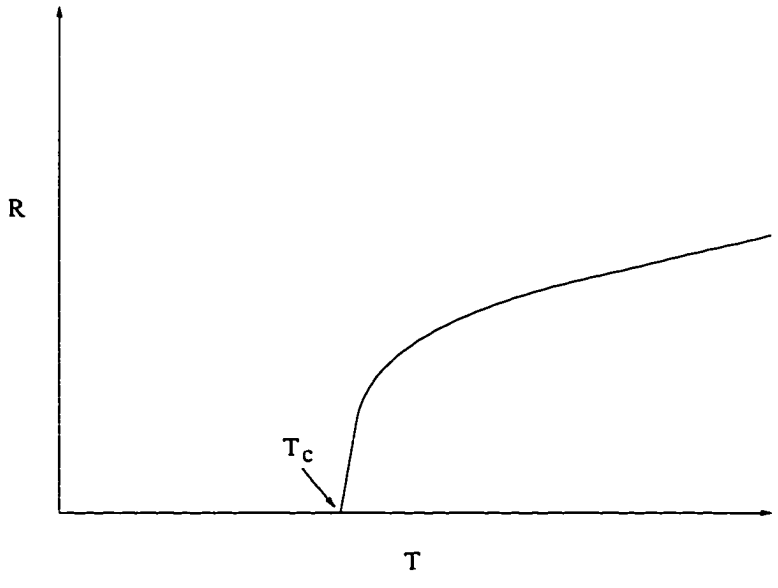

Figure 1.1 Resistance versus temperature for a superconductor. Perfect conductivity is achieved (R=0) at a finite temperature T_c called the critical temperature.

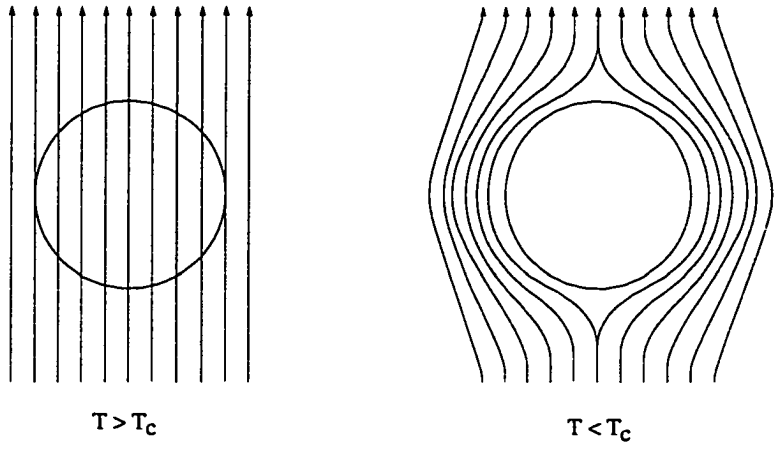

Figure 1.2 The expulsion of a weak magnetic field from a superconducting sphere cooled below its critical temperature T_c. This is commonly refered to as the Meissner effect. When the field at the equator reaches the critical field H_c, the sphere will divide into a mixed state of superconducting and normal regions.

$$\mathbf{E} = \mu_0 \lambda^2 \frac{\partial}{\partial t} \mathbf{J} , \tag{1.1}$$

and

$$\mathbf{B} = -\mu_0 \lambda^2 (\nabla \times \mathbf{J}) , \tag{1.2}$$

where $\mu_0 = 4\pi \times 10^{-7} \mathrm{N/A}^2$ is the permeability of free space, and λ is called the London penetration depth. Equation (1.1) states that any electric field present in the superconductor will accelerate the current rather than doing work against a non-conservative force (perfect conductivity), and Eq. (1.2) can be combined with the Maxwell equation $\nabla \times \mathbf{B} = \mu_0 \mathbf{J}$ to yield

$$\nabla^2 \mathbf{B} = \frac{1}{\lambda^2} \mathbf{B} , \tag{1.3}$$

which implies that a magnetic field is screened exponentially, within a distance λ, of the surface of a superconducting cylinder in a parallel field (perfect diamagnetism), as shown in Fig. 1.3.

The next landmark in the understanding of superconductivity came in 1950 with the phenomenological Ginzburg-Landau theory [Ginzburg and Landau, 1950]. In this theory, the superconducting electrons are represented by a complex order parameter ψ with a magnitude given by $|\psi|^2 = n_s$, where n_s is the number density of superconducting electrons. The order parameter also has a definite phase angle θ which is related to the quantum coherence of the superconducting electrons. In this theory, superconductors can be characterized by a dimensionless parameter $\kappa = \lambda/\xi$, where λ is the magnetic screening length (London penetration depth) and ξ is the coherence length (the characteristic length

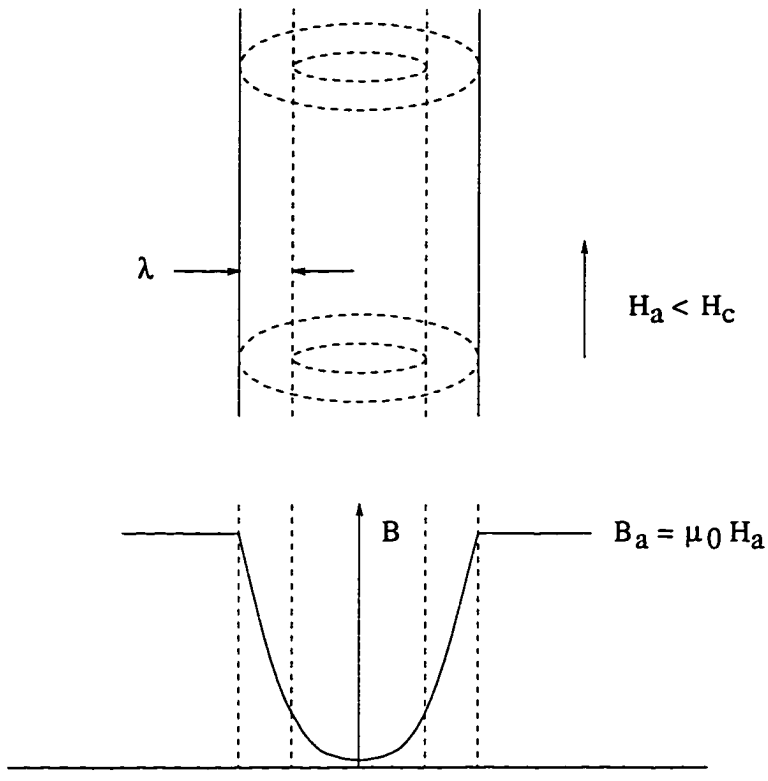

Figure 1.3 Screening of a weak magnetic field, $H_a < H_c$, by a superconducting cylinder. Inside the superconductor the field decreases exponentially within a distance λ of the surface. When $H_a > H_c$, superconductivity will be destroyed and the cylinder will be in the normal state.

for spatial variations in $|\psi|$) (see Fig1.4). Superconductors with $\kappa < 1/\sqrt{2}$ are called type-I and those with $\kappa > 1/\sqrt{2}$ are known as type-II. In 1957 Abrikosov predicted [Abrikosov, 1957] that the structure of the intermediate state, the state where normal and supercondcuting regions coexist (see Fig. 1.4), is different in type-I superconductors than in type-II superconductors. For a type-I superconducting sample with a significant demagnetizing factor (eg., a sphere or flat plate in a perpendicular field), when the field at the surface or edge reaches H_c the sample will divide into normal and superconducting regions. For a type-I superconductor there is a positive surface energy associated with a domain wall between normal and superconducting regions; therefore, a laminar structure tends to form to reduce the surface energy contribution to the free energy. A type-II superconducting sample will enter the intermediate state when the field at the surface or edge reaches the lower critical field H_{c1}. For a type-II superconductor there is a negative surface energy associated with domain walls; therefore, the normal regions tend to divide up into narrow filaments or flux tubes (with radius roughly equal to ξ) in order to take

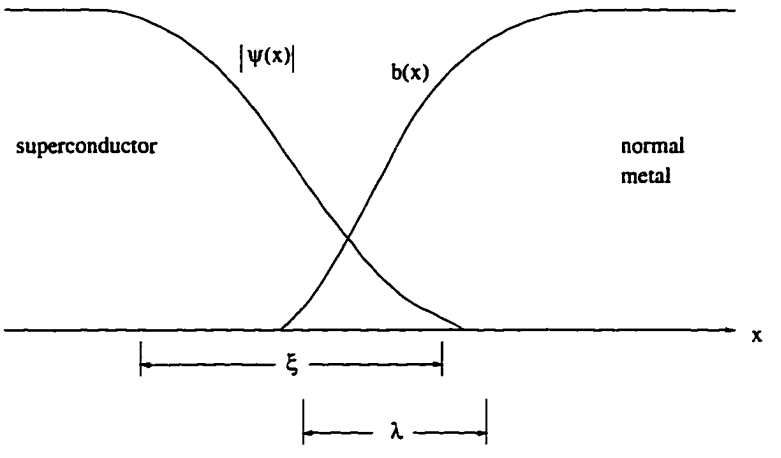

Figure 1.4 Domain wall between a superconducting and normal metal domains in the intermediate state. The microscopic magnetic field $b(x)$ decays exponentially inside the superconductor within a distance λ. The magnitude of the order parameter $|\psi(x)|$ decays exponentially inside the normal metal within a distance ξ. If $\sqrt{2}\lambda < \xi$ then the superconductor is called type-I, and if $\sqrt{2}\lambda > \xi$ it is called type-II.

advantage of the negative surface energy. Each of these flux tubes constitutes an Abrikosov vortex with supercurrents circulating around it, and a flux quantum $\phi_0 = 2.07 \times 10^{-7}\,\mathrm{G\,cm^2}$ of magnetic flux is associated with it (see Fig. 1.5). The density of vortices becomes greater as the surface or edge field increases, until the field reaches the upper critical field H_{c2} when the vortices begin to overlap and superconductivity is destroyed. If there are no significant demagnetizing effects (eg., a long cylinder in a parallel field), then a type-II superconductor will still exist in the critical state between the fields H_{c1} and H_{c2}, but a type-I superconductor will no longer enter the intermediate state; superconductivity will simply be quenched at the field H_c. The relation between the fields B and H, for both type-I and type-II superconductors, in the absence of demagnetizing effects, is shown in Fig. 1.6.

Another landmark development occurring in 1957 was the emergence of the BCS theory [Bardeen et al., 1957] which explains conventional superconductivity on the microscopic level. In this theory the superconducting charge carriers consist of bound electron pairs called Cooper pairs. The BCS theory was able to quantitatively reproduce experimental results for the energy gap (the energy needed to break a Cooper pair), the superconducting transition temperature, and many other physical properties for which the energy gap and excitation spectrum play an important role [Tinkham, 1996]. It was even shown by Gorkov in 1959 [Gorkov, 1959] that the Ginzburg-Landau theory is a limiting case of the BCS theory for temperatures near T_c.

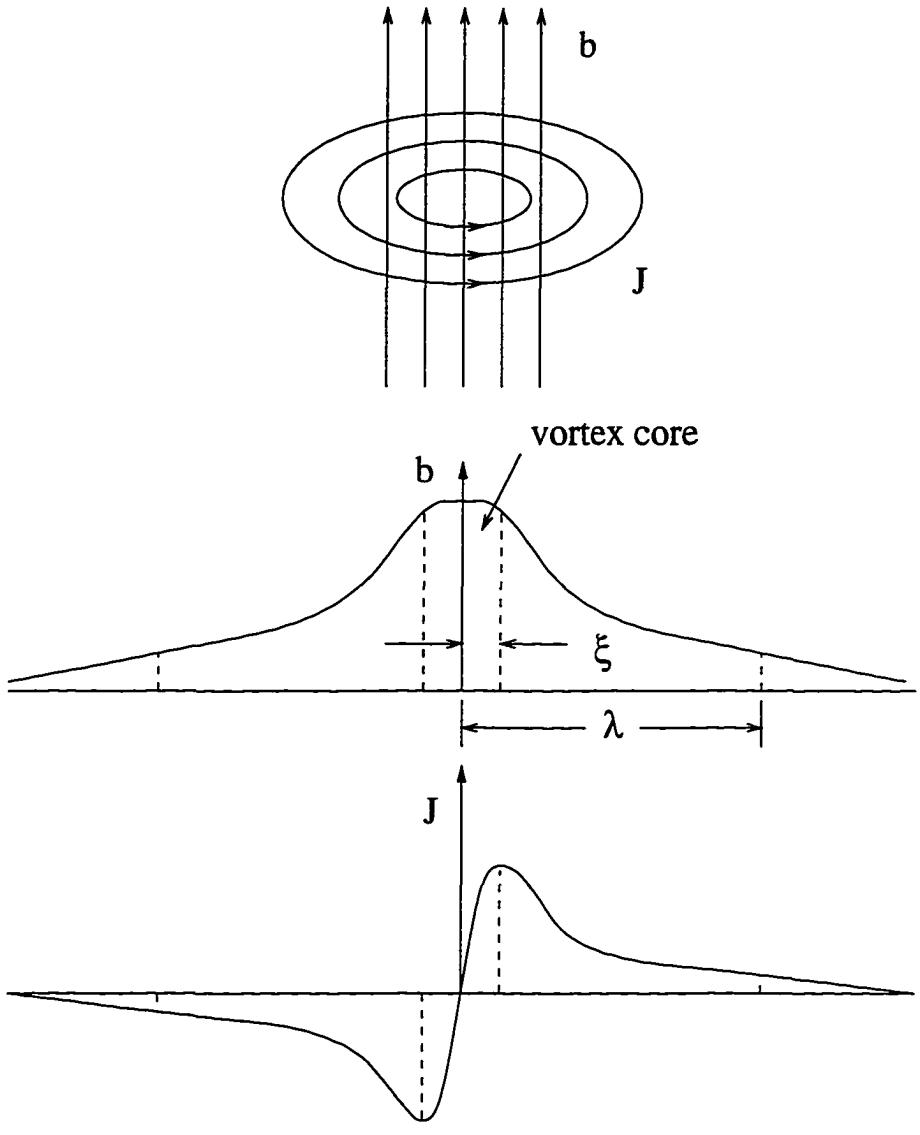

Figure 1.5 Microscopic current **J** and field **b** distributions for an Abrikosov vortex in a type-II superconductor. The core of the vortex is not superconducting and has a radius of ξ. Both **J** and **b** decay exponentially within a distance λ away from the core. The magnetic flux through the surface of an arbitrarily large contour encircling the vortex is equal to $\phi_0 = 2.07 \times 10^{-7}\,\mathrm{G\,cm^2}$.

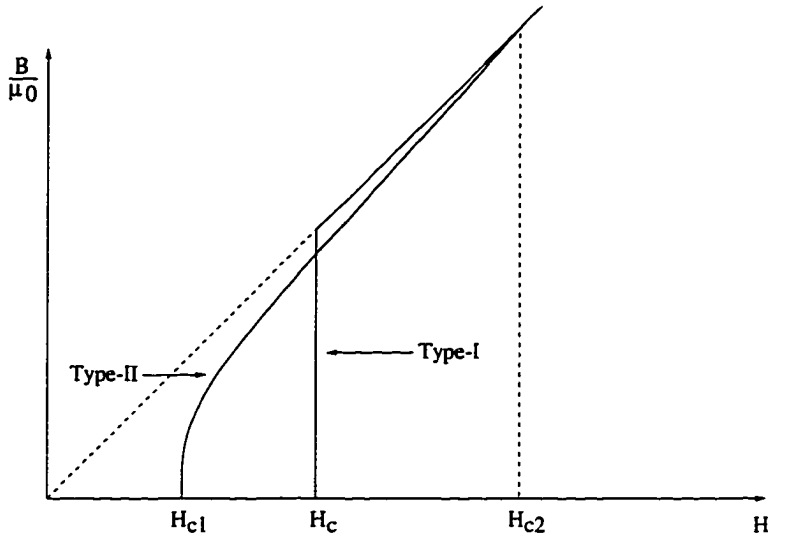

Figure 1.6 The relation between the fields B and H in type-I and type-II superconductors in the absence of demagnetizing effects. In a type-I superconductor, $B = 0$ for $H < H_c$ and $B = \mu_0 H$ for $H > H_c$. In a type-II superconductor, $B = 0$ for $H < H_{c1}$ and $B = \mu_0 H$ for $H > H_{c2}$ but $0 < B < \mu_0 H$ in the intermediate state $H_{c1} < H < H_{c2}$. If $\kappa \gg 1$, then $B \simeq \mu_0 H$ over most of the intermediate state region and $B = \mu_0 H$ is an excellent approximation.

The next major discovery came in 1962 when Josephson [Josephson, 1962] was able to predict a peculiar type of tunneling of Cooper pairs between two superconductors which are weakly coupled together. He found that even in the absence of any voltage drop, there would be a supercurrent, which depends on the phase difference of their order parameters, flowing between the two superconductors. This discovery has led to numerous applications including the development of extremely precise voltmeters and magnetometers.

The last major landmark in the history of superconductors occured in 1986 when Bednorz and Muller [Bednorz and Muller, 1986] discovered superconductivity, with a $T_c \simeq 35$K, in the ceramic compound LBCO. This important find was followed by the discoveries of other oxide superconductors such as YBCO, BSCCO, and TBCCO, with T_c's > 80K. These high-temperature superconductors (HTS's) have revitalized interest in applications of superconductivity because they can operate at liquid nitrogen temperatures ($T \simeq 77K$), and have very high upper critical fields; however, they also present researchers with significant challenges such as trying to understand the pairing mechanism, the order parameter symmetry, fluctuation effects, and many other novel phenoma. These materials are also challenging from the materials science and applications standpoint because they are not malleable and typically

contain many defects, such as grain boundaries, which cause nonlinear behavior not present in ohmic materials.

1.2 Applications of high-temperature superconductors in microwave devices

There is presently considerable interest in the use of HTS's in passive microwave devices such as filters for wireless communication [Liang et al. 1995, Lubkin, 1995, Oates et al., 1995, Shen, 1994]. It is generally believed that this will be one of the first wide-spread applications for HTS's [Lubkin, 1995]. Much of this belief stems from the superior performance (narrower bandwidth) of recent prototypes of HTS filters [Liang et al., 1995, Lubkin, 1995, Shen, 1994]. This improvement is due to the lower conductor losses in HTS's as compared with conventional conductors such as copper. These lower losses lead to a larger Q, and narrower bandwidth, for resonators and filters.

There are, however, many obstacles to overcome before HTS filters become a marketable technology. One major problem is the inherent nonlinearity of HTS's. This nonlinearity manifests itself in a dependence of the surface impedance on the input power [Golosovsky, 1995, Nguyen, 1995]. One consequence of this non-ohmic behavior is that the low-power surface impedance is no longer a sufficient figure of merit for the material. Instead, the surface impedance must be determined at the specific power at which the device will be operated [Nguyen, 1995]. Nonlinearities can also lead to harmonic generation (HG) and to two-frequency intermodulation. In HG, an input signal with a single frequency ω leads to an output signal with components at integer multiples of ω. In IM, an input signal with two closely spaced frequencies ω_1 and ω_2 leads to an output signal with components at frequencies which are linear combinations of ω_1 and ω_2. The occurrence of IM in filters can cause various problems such as the generation of spurious targets in radar receivers [Nguyen, 1995]. A thorough understanding of all these effects is essential before high-quality devices can be successfully designed and constructed.

Nonlinear effects occur at both low and high powers; however, the power and frequency dependence of these effects changes upon moving from the low-power to the high-power regimes [Halbritter, 1990, 1995, Nguyen, 1995]. It is believed that in the low-power regime the nonlinearity is caused by grain boundaries which act as weak links or Josephson junctions, while at higher powers it is suspected that vortex pinning is the dominant mechanism [Oates, 1995].

1.3 Sources of nonlinearity in superconductors

1.3.1 Weak links

Bulk HTS's are granular in structure. They consist of strongly superconducting grains which are weakly coupled to each other by non-superconducting interface material. This granularity creates many weak links or Josephson junctions which can cause nonlinearities in HTS samples.

In general, a Josephson junction or weak link is any region of strongly suppressed order parameter (weakened superconductivity) between two superconducting electrodes. One example of a weak link is pictured in Fig. 1.7.

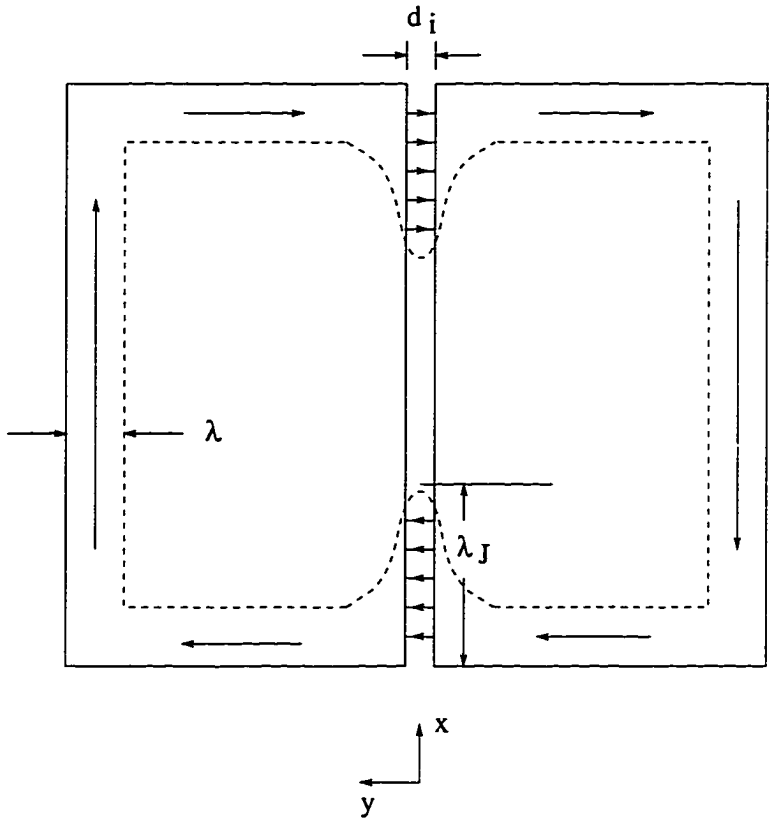

Figure 1.7 A Josephson junction formed by two superconducting electrodes, infinitely tall in the z direction, with a slab of thickness d_i and infinite resistivity placed between them. A weak magnetic field applied in the z direction will penetrate a distance λ into the superconductors, and a distance λ_J along the junction. There will be supercurrents circulating around the perimeter of the superconductors, within a thickness λ of the surface, and Josephson currents flowing across the junction, within a distance λ_J of the edges. The arrows indicate the directions of current flow.

The figure shows two superconducting electrodes with a an infinite-resistivity region sandwiched between them (the electrodes are not electrically connected). Each of the superconductors has an averaged wavefunction of the form $\psi = |\psi| \exp(i\theta)$, where θ is the phase associated with the coherence of the Cooper pairs [Van Duzer and Turner, 1981]. When the separation between the superconductors is small enough ($\lesssim \xi$), their averaged wavefunctions can overlap, and Cooper pairs can tunnel across the barrier. This Josephson tunneling can be described by the equations

$$J_y(x) = J_0 \sin\Delta\gamma(x,t)\,, \tag{1.4}$$

and

$$e_y(x,t) = \frac{\phi_0}{2\pi d_i}\frac{\partial}{\partial t}\Delta\gamma(x,t)\,, \tag{1.5}$$

where $\Delta\gamma$ is the gauge-invariant phase difference between the superconductors, and J_0 is the Josephson critical current density (a measure of the coupling strength between the superconductors). The relation between $\Delta\gamma$ and $\Delta\theta$ is [Tinkham, 1996]

$$\Delta\gamma(x,t) = \Delta\theta(x,t) - \frac{2\pi}{\phi_0}\int A_y dy\,, \tag{1.6}$$

where A_y is the magnetic vector potential, and the integral is along a line connecting the two superconductors. Equation (1.4) is interesting because it predicts a tunneling current between the two superconductors even in the absence of any voltage difference. This is very different from the case of tunneling of normal electrons through an energy barrier, which requires the application of a finite bias voltage to induce the tunneling. When the non-superconducting region between the syperconductors has a finite resistivity ρ_i, Eq. (1.4) must be modified by adding a term, e_y/ρ_i, to account for the tunneling of quasi-particles or normal electrons between the superconductors.

Since it is believed that the grain boundaries in HTS samples act as Josephson junctions, it is useful to study the model pictured in Fig.1.7. A thorough understanding of the nonlinearities encountered in this simple model may lead to a much better understanding of the nonlinearities found in actual HTS devices. However, actual grain boundaries undoubtedly are nonuniform, and this would probably need to be incorporated into the model to achieve accurate results.

1.3.2 Vortex pinning and the critical state model

When the field at the suface of a HTS exceeds the lower critical field H_{c1}, magnetic flux will begin penetrating into the interior of the sample in the form of vortices (see Fig. 1.5). In HTS's there are many inpurities and defects which tend to pin these vortices. This feature is actually advantageous because

an external current will exert a force on a vortex which tends to make it move. A moving vortex creates an electric field and dissipates energy. Therefore, dissipationless current flow is only possible if there is a force, the pinning force, which is equal and opposite to the force of the external current. Superconductors with strong pinning are called hard superconductors because of their mechanical properties. Hard superconductors exhibit strong nonlinearities such as magnetic irreversiblity and hysteresis in their magnetization curves.

Magnetic hysteresis in hard type-II superconductors can be understood in terms of the critical state model [Bean, 1962, Brandt and Indenbom, 1993, Norris, 1970, Zeldov et al., 1994]. In this model the density of vortices n is assumed large enough ($n\lambda^2 \gg 1$) that the vortices essentially form a continuum with average magnetic-flux density parallel to the vortices given by $B = n\phi_0$ [Zeldov et al., 1994]. The force per unit volume that tends to drive the vortices in from the surface is the Lorentz-force density $\mathbf{F} = \mathbf{J} \times \mathbf{B}$, where $\mathbf{J} = \nabla \times \mathbf{H}$. In the absence of a surface barrier, $\mathbf{B}$ and $\mathbf{H}$ satisfy the Maxwell boundary conditions at the sample surface (continuity of the normal component of $\mathbf{B}$ and the tangential component of $\mathbf{H}$). In critical-state models, it is typically assumed that, to good approximation, $\mathbf{B} = \mu_0 \mathbf{H}$. This is an excellent approximation when $B \gg \mu_0 H_{c1}$ (see. Fig. 1.6), which is often satisfied in HTS's. A force balance obtains when the Lorentz-force density on the vortex array is balanced by the pinning force density. The maximum pinning-force density is characterized by a critical current density J_c. When the magnitude of $\mathbf{J}$ exceeds J_c, the distribution of vortices, and hence $\mathbf{B}$, changes until the force balance is restored [Zeldov et al., 1994]. There is an important distinction in critical-state models between parallel and perpendicular geometries. An example of the parallel geometry is shown in Fig. 1.8. In this geometry, the penetrating vortices are nearly parallel to the sample surface. Figure 1.9 shows an example of the perpendicular geometry. In this geometry the vortices are curved in the neighborhood of the sample surface because of the large demagnetizing effects [Brandt and Indenbom, 1993, Zeldov et al., 1994]. This difference can be observed by examining the equation $\nabla \times \mathbf{B} = \mu_0 \mathbf{J}$, where I have assumed that $\mathbf{B} = \mu_0 \mathbf{H}$. This equation can be written as $(\nabla B) \times \hat{\mathbf{B}} + B\left(\nabla \times \hat{\mathbf{B}}\right) = \mu_0 \mathbf{J}$, where $\hat{\mathbf{B}} = \mathbf{B}/B$ [Brandt and Indenbom, 1993, Clem, 1990, 1994]. The first term on the left-hand side depends on the spatial gradient of the flux density, while the second term depends on the curvature of the flux lines. In the parallel geometry the Lorentz force stems mainly from gradients in magnetic pressure. In the perpendicular geometry, however, the magnetic-field lines bend around the sample and the tangential component has opposite signs on opposite sides of the sample. This leads to a large vortex curvature so that the second term on the left-hand side of the equation becomes dominant. Since the dominant terms are different in the two geometries, the structure of the critical state is also different.

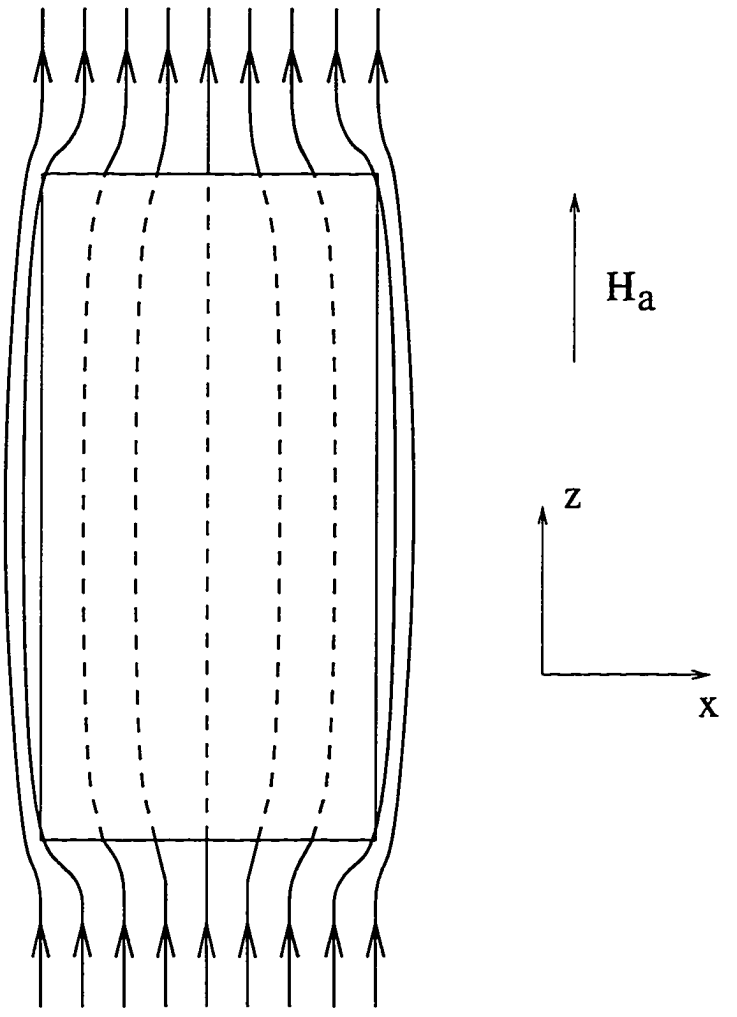

Figure 1.8 Cross-sectional view of a superconducting slab (infinite in the y direction) in a parallel field. All vortex lines are essentially parallel to the faces of the slab.

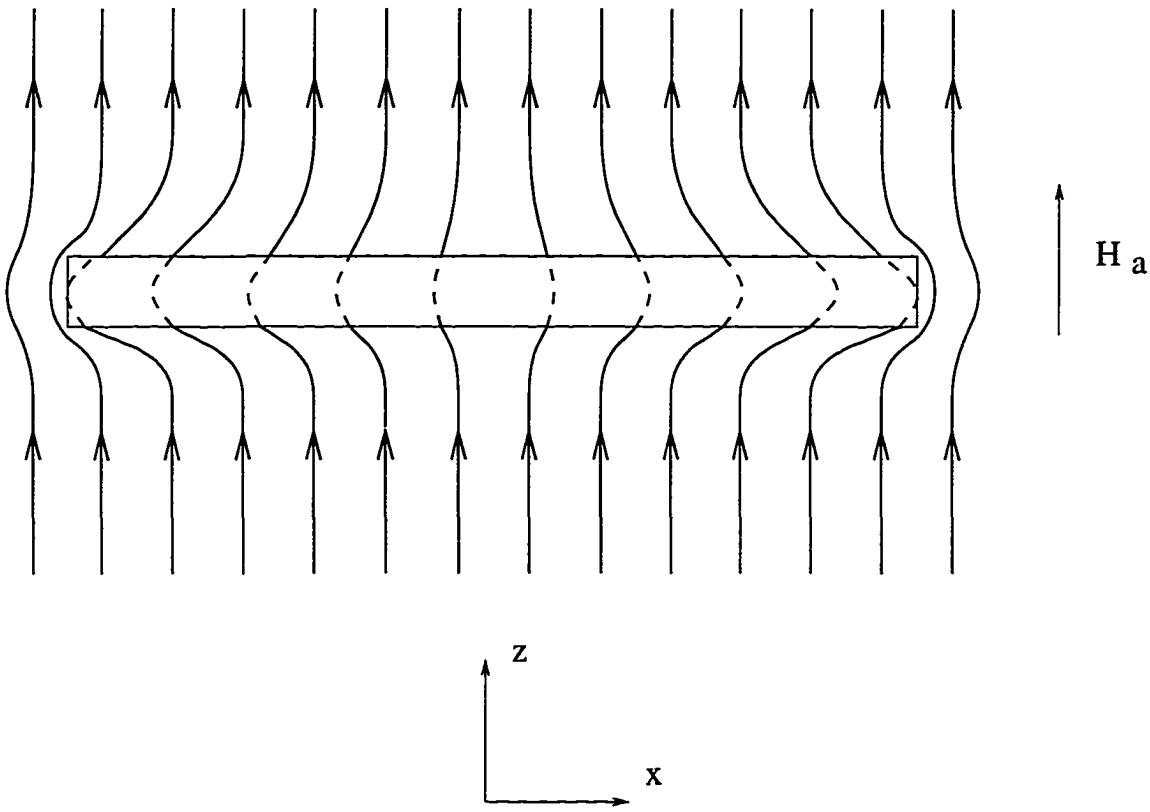

Figure 1.9 Cross-sectional view of a superconducting strip (infinite in the y direction) in a perpendicular field. The vortex lines near the edges of the strip are curved because of demagnetizing effects.

2 NONLINEARITIES IN HARD SUPERCONDUCTORS

2.1 Critical state model

2.1.1 Introduction

In this chapter I will investigate the role of vortex pinning on the generation of nonlinearities in type-II superconductors. In Sec. 2.1 I will discuss the structure of the critical state (assuming no surface barriers) in a half space, a thin-film strip, and a wire of elliptical cross section. I will then use these results in Secs. 2.2 and 2.3 to calculate the nonlinear surface impedance in a superconducting half space, and harmonic generation and intermodulation distortion in a superconducting transmission line.

2.1.2 Superconducting half space in an applied field

In this section I consider the superconducting half space pictured in Fig. 2.1. The region $x > 0$ is occupied by a type-II superconductor with London penetration depth λ. There is an applied magnetic field $\mathbf{B}_a = B_a\hat{z}$ in the region $x < 0$. The applied field induces currents in the superconductor. When B_a is less than the lower critical field $\mu_0 H_{c1}$, the induced current consists of an equilibrium screening current concentrated in a layer of thickness λ near the surface of the superconductor. When $B_a \gg \mu_0 H_{c1}$ many vortices penetrate into the superconductor inducing a nonequilibrium current density $\mathbf{J} = \nabla \times \mathbf{H}$. The magnitude of $\mathbf{J}$ is much larger than the magnitude of the screening current density, which means that to good approximation $\mathbf{B} = \mu_0\mathbf{H}$. Therefore, one can write $\nabla \times \mathbf{B} = \mu_0\mathbf{J}$, which in this geometry reduces to

$$\frac{dB_z(x)}{dx} = -\mu_0 J_y(x)\,. \tag{2.1}$$

Once vortices have penetrated in from the surface, the sample can be divided into two regions. There is a vortex-occupied outer region $0 < x < a_1$, which is in the critical state with $J_y = J_c$. There is also an inner region $x > a_1$, which is screened from the applied field with $J_y(x) = 0$ and $B_z(x) = 0$. Using Eq. (2.1), and assuming that J_c is a constant, the critical-state profiles obtained are [Bean, 1962.

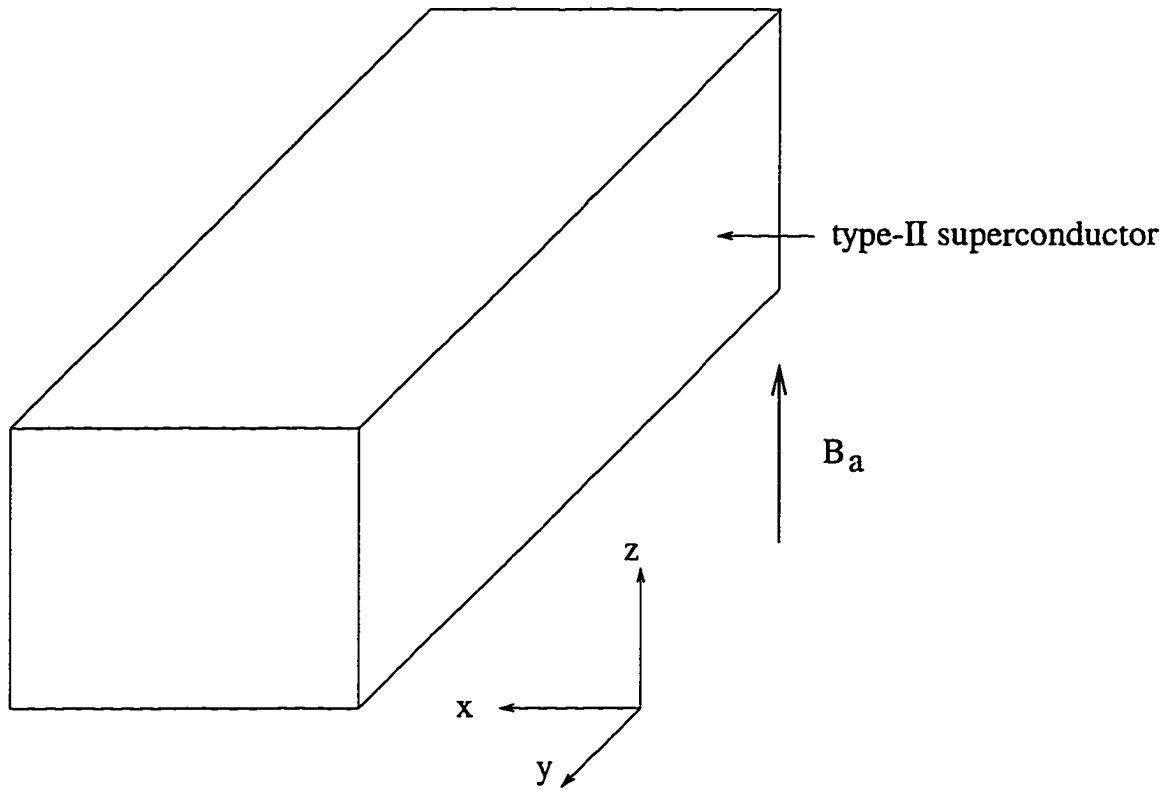

Figure 2.1 Superconducting half space (infinite along the y and z directions and semi-infinite along the x direction) with an external magnetic field $\mathbf{B}_a$ applied along the z direction.

Zeldov et al., 1994]

$$J_y(x) = \begin{cases} J_c\,, & 0 < x < a_1\,, \\ 0\,, & x > a_1\,, \end{cases} \tag{2.2}$$

$$B_z(x) = \begin{cases} B_a(1 - x/a)\,, & 0 < x < a_1\,, \\ 0\,, & x > a_1\,, \end{cases} \tag{2.3}$$

where the distance a_1 is given by

$$a_1 = \frac{B_a}{\mu_0 J_c}\,. \tag{2.4}$$

Figure 2.2 shows a typical current and field distribution.

I now consider the case when the applied field is decreased from an initial value B_{a0} to a new value B_a. Initially the current and flux densities are nonzero only in the outer region $0 < x < a_0$ [the profiles are given by Eqs. (2.2-2.4) with B_a replaced by B_{a0} and a_1 replaced by a_0]. After the field is decreased, there will be an outer region $0 < x < a_1$, where the current density and flux density will change, and a field-invariant inner region $x > a_1$, where the current density and flux density remain the same. The

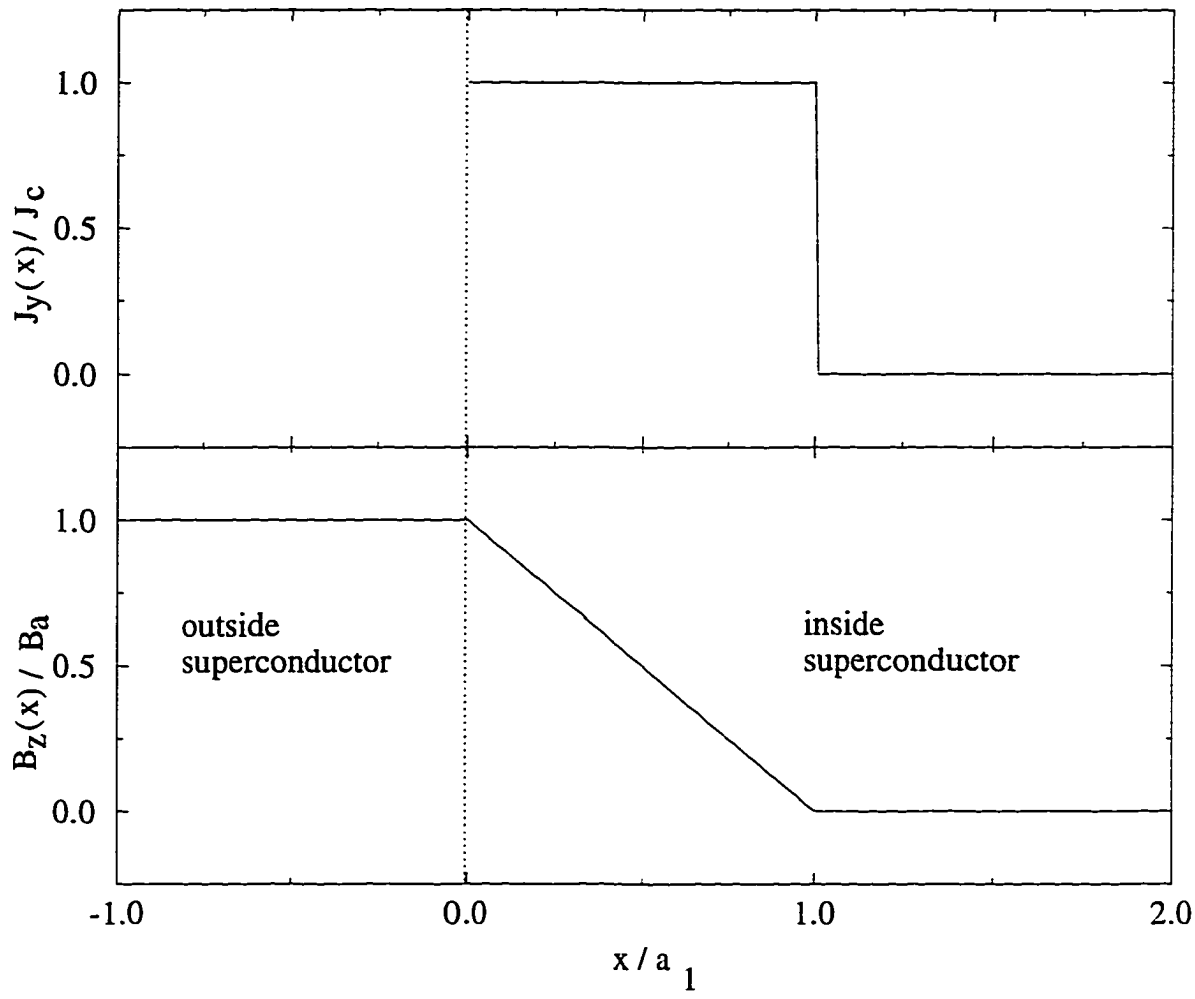

Figure 2.2 Typical current-density and flux-density profiles for flux penetration into a type-II superconducting half space initially in the virgin state.

current density in the outer region is $J_y(x) = -J_c$ and the flux density can be calculated from

$$\frac{dB_z(x)}{dx} = -\mu_0 J_c . \tag{2.5}$$

The resulting current and field profiles are

$$J_y(x) = \begin{cases} -J_c , & 0 < x < a_1 , \\ J_c , & a_1 < x < a_0 , \\ 0 , & x > a_0 . \end{cases} \tag{2.6}$$

$$B_z(x) = \begin{cases} B_{a0}\,(1 + (x - 2a_1)/a_0) , & 0 < x < a_1 , \\ B_{a0}(1 - x/a_0) , & a_1 < x < a_0 , \\ 0 , & x > a_0 , \end{cases} \tag{2.7}$$

where the distances a_0 and a_1 are given by

$$a_0 = \frac{B_{a0}}{\mu_0 J_c} , \tag{2.8}$$

and

$$a_1 = \frac{B_{a0} - B_a}{2\mu_0 J_c} . \tag{2.9}$$

Figure 2.3 shows the current and field distributions for several values of B_a between B_{a0} and $-B_{a0}$. If the applied field is then increased starting from $B_a = -B_{a0}$, the profiles are given by [Bean, 1962. Zeldov et al., 1994]

$$J_y(x) = \begin{cases} J_c , & 0 < x < a_1 , \\ -J_c , & a_1 < x < a_0 , \\ 0 , & x > a_0 , \end{cases} \tag{2.10}$$

$$B_z(x) = \begin{cases} -B_{a0}\,(1 + (x - 2a_1)/a_0) , & 0 < x < a_1 , \\ B_{a0}(-1 + x/a_0) , & a_1 < x < a_0 , \\ 0 , & x > a_0 , \end{cases} \tag{2.11}$$

with

$$a_1 = \frac{B_{a0} + B_a}{2\mu_0 J_c} . \tag{2.12}$$

These profiles are shown in Fig. 2.4.

2.1.3 Superconducting strip in a perpendicular applied field

In this section I consider the superconducting strip pictured in Fig. 2.5. The region $|x| < W$ and $|z| < d/2$ is occupied by a type-II superconductor with London penetration depth λ. It is assumed that

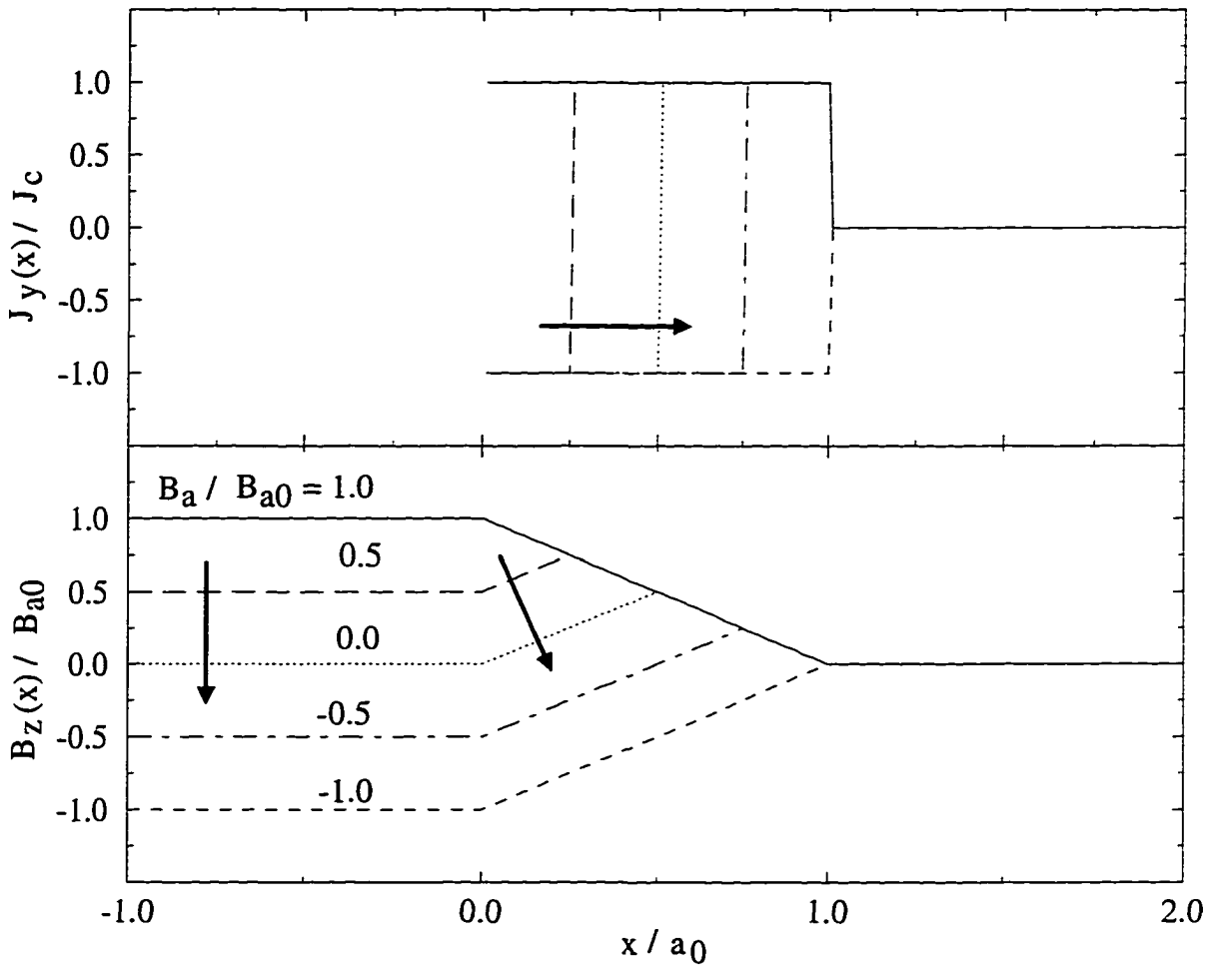

Figure 2.3 Current-density and flux-density profiles for flux penetration into a type-II superconducting half space as the applied field is decreased from B_{a0} to $-B_{a0}$. The arrows indicate the progression of the profiles as the applied field is decreased.

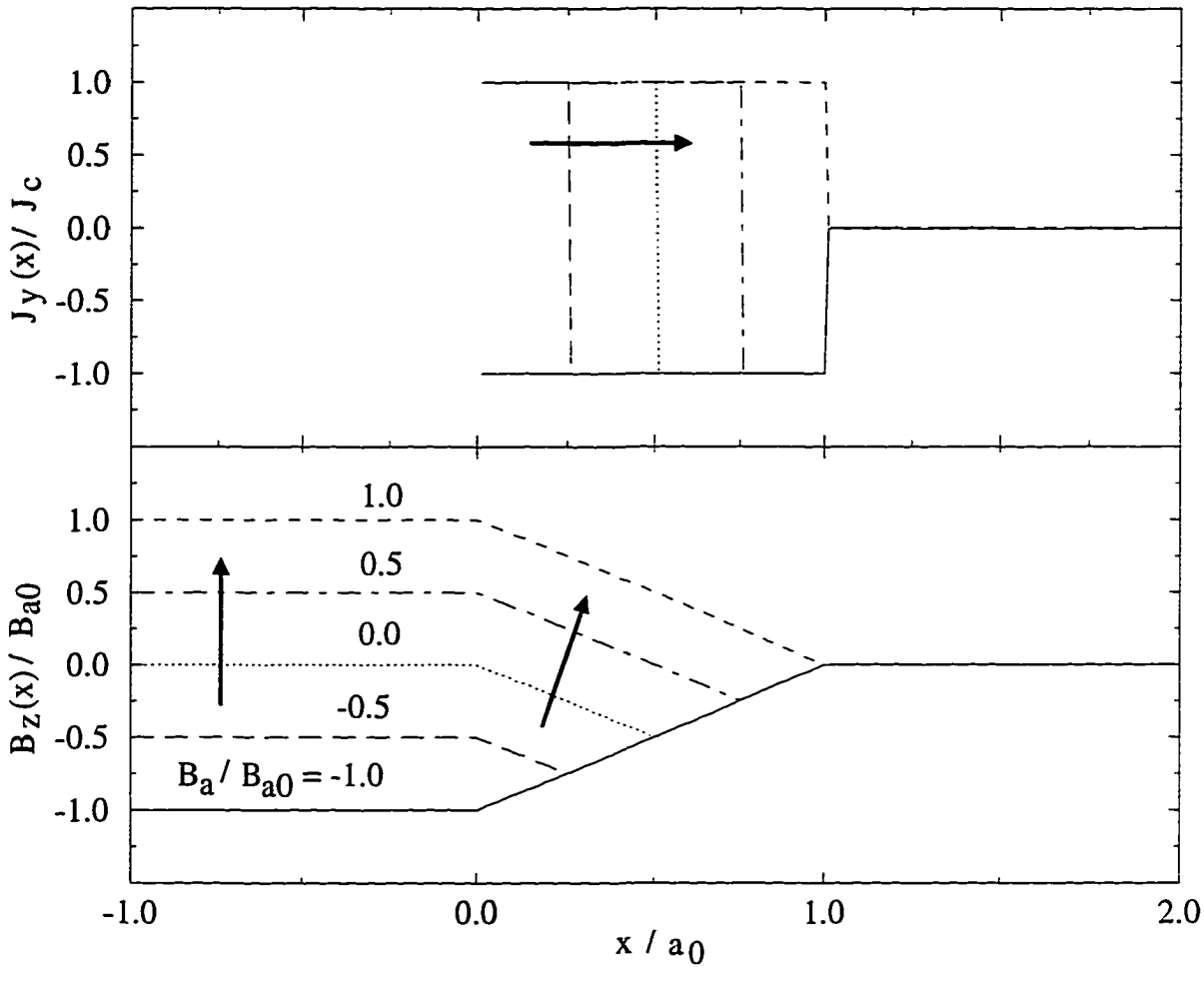

Figure 2.4 Current-density and flux-density profiles for flux penetration into a type-II superconducting half space as the applied field is increased from $-B_{a0}$ to B_{a0}. The arrows indicate the progression of profiles as the applied field is increased.

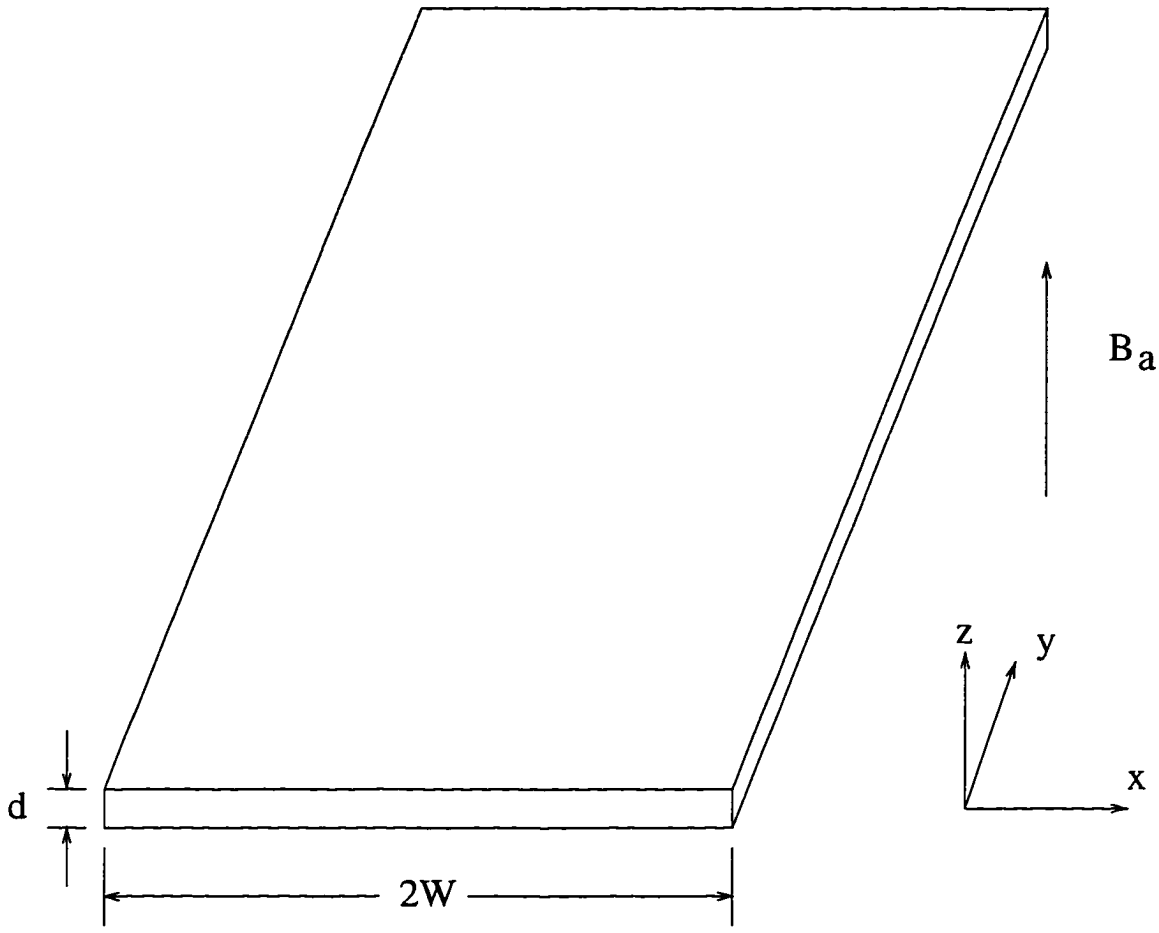

Figure 2.5 Superconducting strip (infinite along the y direction) of width $2W$ and thickness d with an external magnetic field $\mathbf{B}_a$ applied along the z direction.

$d \ll W$ and $\lambda \ll W$. There is an applied magnetic field $\mathbf{B}_a = B_a \hat{z}$. The applied field induces currents in the superconductor. When the magnetic field at the edge of the strip, which is approximately equal to $B_a\sqrt{W/d}$ [Brandt and Indenbom, 1993, Zeldov et al., 1994], is less than the lower critical field $\mu_0 H_{c1}$, the induced current consists of an equilibrium screening current given by

$$J_y(x) = -\frac{2B_a}{\mu_0 d}\frac{x}{\sqrt{W^2 - x^2}}, \qquad |x| < W, \tag{2.13}$$

which leads to the flux density

$$B_z(x) = \begin{cases} 0, & |x| < W, \\ B_a \frac{|x|}{\sqrt{x^2 - W^2}}, & |x| > W. \end{cases} \tag{2.14}$$

Equations (2.13) and (2.14), which can be obtained by conformal mapping methods [Huebener et al., 1972, Swan, 1968], are exact in the limit $d \to 0$. The apparent square root divergence is an artifact of

the assumption of infinitesimal film thickness [Zeldov et al., 1994]. In the case of finite d, J_y and B_z are understood to be averaged over the film thickness, and the expressions in Eqs. (2.13) and (2.14) fail when the edges of the strip are approached to within a distance d if $d \gtrsim \lambda$ or $\Lambda = 2\lambda^2/d$ if $d \ll \lambda$ [Zeldov et al., 1994].

When $B_a\sqrt{W/d} \gg \mu_0 H_{c1}$ many vortices penetrate into the film, and to good approximation $\mathbf{B} = \mu_0\mathbf{H}$. In this regime one may write $\nabla \times \mathbf{B} = \mu_0\mathbf{J}$, which reduces in the strip geometry to

$$\frac{B_x(x, z = d/2) - B_x(x, z = -d/2)}{d} = \mu_0 J_y(x)\,. \tag{2.15}$$

Equation (2.15) should be compared with Eq. (2.1) for the half space geometry.

Once vortices have penetrated in from the edge, the strip can be divided into three regions. There are two vortex-occupied outer regions $a_1 < |x| < W$, which are in the critical state with $J_y = -\frac{x}{|x|}J_c$. There is also an inner region $|x| < a_1$, which is screened from the applied field with $B_z(x) = 0$. Both $J_y(x)$ and $B_z(x)$ must be determined by solving the boundary value problem $B_z(|x| < a_1) = 0$ and $J_y(a_1 < |x| < W) = -\frac{x}{|x|}J_c$. This problem has been solved for a constant J_c using conformal mapping [Norris, 1970, Brandt and Indenbom, 1993, Zeldov et al., 1994],

$$J_y(x) = \begin{cases} J_c\,, & -W < x \le -a_1\,, \\ -\frac{2J_c}{\pi}\arctan\left(\frac{x}{W}\sqrt{\frac{W^2-a_1^2}{a_1^2-x^2}}\right), & |x| < a_1\,, \\ -J_c\,, & a_1 \le x < W\,, \end{cases} \tag{2.16}$$

$$B_z(x) = \begin{cases} 0\,, & |x| \le a_1\,, \\ B_f \ln\frac{|x|\sqrt{W^2-a_1^2}+W\sqrt{x^2-a_1^2}}{a_1\sqrt{|x^2-W^2|}}, & |x| > a_1\,, \end{cases} \tag{2.17}$$

and

$$a_1 = \frac{W}{\cosh(B_a/B_f)}\,, \tag{2.18}$$

where $B_f = \mu_0 J_c d/\pi$. Figure 2.6 shows current and field profiles for several values of B_a.

I now consider the case when the applied field is decreased from an initial value B_{a0} to a new value B_a. Initially the current and flux densities are given by Eqs. (2.16-2.18) with B_a replaced by B_{a0} and a_1 replaced by a_0. After the field is decreased, there will be two outer regions $a_1 < |x| < W$, where the current density and flux density will change, and a field-invariant inner region $|x| < a_1$, where the current density will change but the flux density will remain the same; this is in contrast to the half space geometry where the current density only changed in the region near the surface. The current and flux-density profiles have been determined previously using a superposition method [Brandt and Indenbom, 1993, Zeldov et al., 1994]

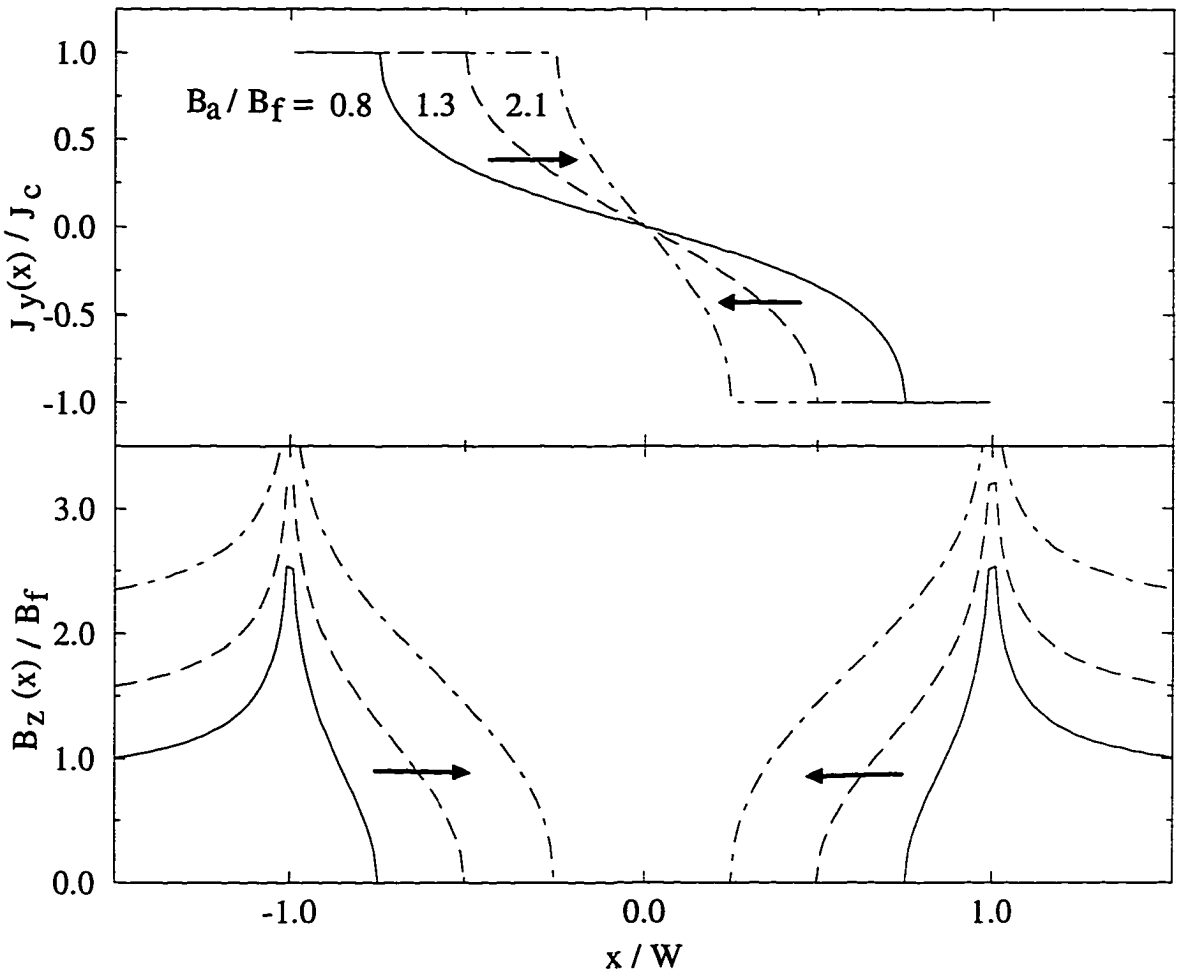

Figure 2.6 Current-density and flux-density profiles for flux penetration into a type-II superconducting strip initially in the virgin state. The arrows indicate the progression of profiles as the applied field is increased.

$$J_y(x) = \begin{cases} -J_c\,, & -W < x \le -a_1\,, \\ J_c\left[1+\frac{4}{\pi}\arctan\left(\frac{x}{W}\sqrt{\frac{W^2-a_1^2}{a_1^2-x^2}}\right)\right], & -a_1 < x \le -a_0\,, \\ \frac{2J_c}{\pi}\left[2\arctan\left(\frac{x}{W}\sqrt{\frac{W^2-a_1^2}{a_1^2-x^2}}\right)-\arctan\left(\frac{x}{W}\sqrt{\frac{W^2-a_0^2}{a_0^2-x^2}}\right)\right], & |x| < a_0\,, \\ -J_c\left[1-\frac{4}{\pi}\arctan\left(\frac{x}{W}\sqrt{\frac{W^2-a_1^2}{a_1^2-x^2}}\right)\right], & a_0 \le x < a_1\,, \\ J_c\,, & a_1 \le x < W\,, \end{cases} \tag{2.19}$$

and

$$B_z(x) = \begin{cases} 0\,, & |x| \le a_0\,, \\ B_f \ln\frac{|x|\sqrt{W^2-a_0^2}+W\sqrt{x^2-a_0^2}}{a_0\sqrt{W^2-x^2}}, & a_0 < |x| \le a_1\,, \\ B_f\left(\ln\frac{|x|\sqrt{W^2-a_0^2}+W\sqrt{x^2-a_0^2}}{a_0\sqrt{|x^2-W^2|}}-2\ln\frac{|x|\sqrt{W^2-a_1^2}+W\sqrt{x^2-a_1^2}}{a_1\sqrt{|x^2-W^2|}}\right), & |x| > a_1\,, \end{cases} \tag{2.20}$$

where

$$a_0 = \frac{W}{\cosh(B_{a0}/B_f)}\,, \tag{2.21}$$

and

$$a_1 = \frac{W}{\cosh\left((B_{a0}-B_a)/2B_f\right)}\,. \tag{2.22}$$

Figure 2.7 shows the current and field profiles for several values of B_a between B_{a0} and $-B_{a0}$. If the applied field is then increased starting from $B_a = -B_{a0}$, the profiles are given by

$$J_y(x) = \begin{cases} J_c\,, & -W < x \le -a_1\,, \\ -J_c\left[1+\frac{4}{\pi}\arctan\left(\frac{x}{W}\sqrt{\frac{W^2-a_1^2}{a_1^2-x^2}}\right)\right], & -a_1 < x \le -a_0\,, \\ -\frac{2J_c}{\pi}\left[2\arctan\left(\frac{x}{W}\sqrt{\frac{W^2-a_1^2}{a_1^2-x^2}}\right)-\arctan\left(\frac{x}{W}\sqrt{\frac{W^2-a_0^2}{a_0^2-x^2}}\right)\right], & |x| < a_0\,, \\ J_c\left[1-\frac{4}{\pi}\arctan\left(\frac{x}{W}\sqrt{\frac{W^2-a_1^2}{a_1^2-x^2}}\right)\right], & a_0 \le x < a_1\,, \\ -J_c\,, & a_1 \le x < W\,, \end{cases} \tag{2.23}$$

$$B_z(x) = \begin{cases} 0\,, & |x| \le a_0\,, \\ -B_f \ln\frac{|x|\sqrt{W^2-a_0^2}+W\sqrt{x^2-a_0^2}}{a_0\sqrt{W^2-x^2}}, & a_0 < |x| \le a_1\,, \\ -B_f\left(\ln\frac{|x|\sqrt{W^2-a_0^2}+W\sqrt{x^2-a_0^2}}{a_0\sqrt{|x^2-W^2|}}-2\ln\frac{|x|\sqrt{W^2-a_1^2}+W\sqrt{x^2-a_1^2}}{a_1\sqrt{|x^2-W^2|}}\right), & |x| > a_1\,, \end{cases} \tag{2.24}$$

where

$$a_1 = \frac{W}{\cosh\left((B_{a0}+B_a)/2B_f\right)}\,. \tag{2.25}$$

These profiles are shown in Fig. 2.8.

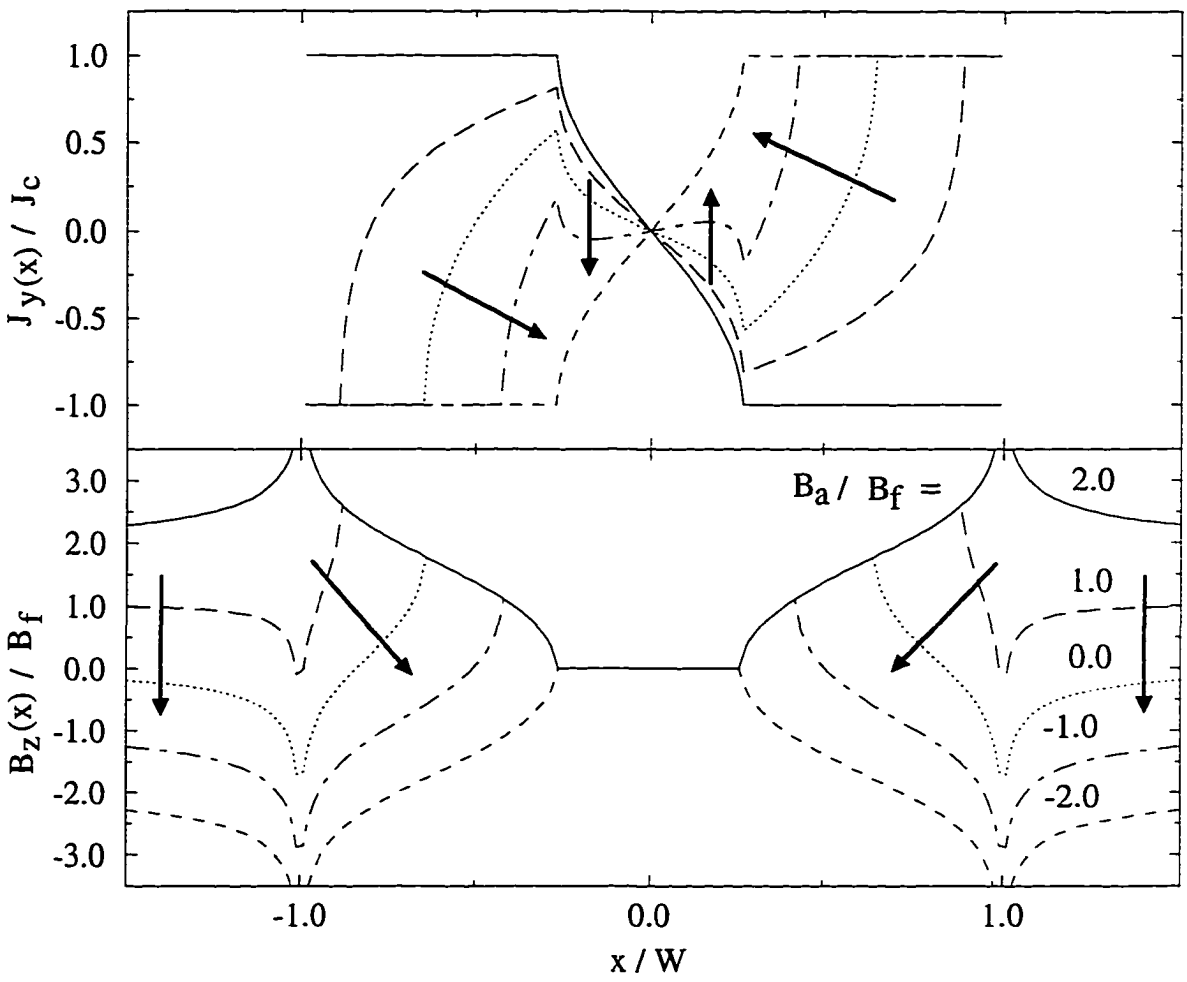

Figure 2.7 Current-density and flux-density profiles for flux penetration into a type-II superconducting strip as the applied field is decreased from B_{a0} to $-B_{a0}$. The arrows indicate the progression of profiles as the applied field is decreased.

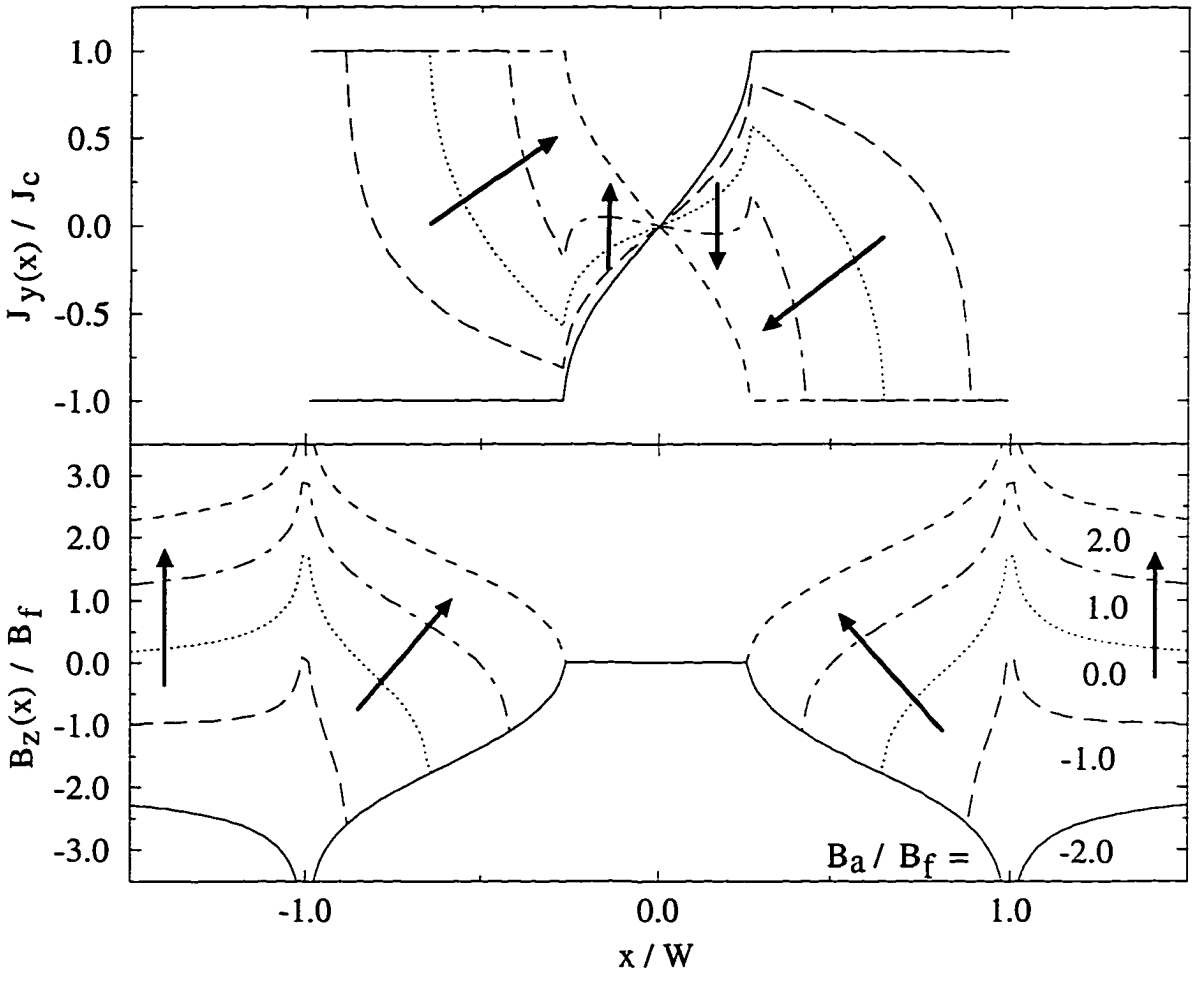

Figure 2.8 Current-density and flux-density profiles for flux penetration into a type-II superconducting strip as the applied field is increased from $-B_{a0}$ to B_{a0}. The arrows indicate the progression of profiles as the applied field is increased.

2.1.4 Superconducting strip carrying a transport current

In this section I consider the superconducting strip pictured in Fig. 2.9. There is a transport current I_T flowing along the strip in the positive y direction. When the magnitude of the induced magnetic field at the edge of the strip, which is approximately equal to $\mu_0 I_T/2\pi\sqrt{Wd}$ [Zeldov et al., 1994], is less than $\mu_0 H_{c1}$, the transport current is carried by an equilibrium screening current density given by

$$J_y(x) = \frac{I_T}{\pi d\sqrt{W^2 - x^2}}, \qquad |x| < W, \tag{2.26}$$

which induces a flux density

$$B_z(x) = \begin{cases} 0, & |x| < W, \\ -\frac{\mu_0 I_T}{2\pi}\frac{x}{|x|\sqrt{x^2-W^2}}, & |x| > W. \end{cases} \tag{2.27}$$

Equations (2.26) and (2.27) can be obtained by conformal mapping methods [Huebener et al., 1972, Swan, 1968] in the limit $d \to 0$. The apparent square root divergence is an artifact of the assumption of infinitesimal film thickness. In the case of finite d, J_y and B_z are understood to be averaged over the film thickness, and the expressions in Eqs. (2.26) and (2.27) fail when the edges of the strip are approached to within a distance d if $d \gtrsim \lambda$ or $\Lambda = 2\lambda^2/d$ if $d \ll \lambda$ [Zeldov et al., 1994].

When $\mu_0 I_T/2\pi\sqrt{Wd} \gg \mu_0 H_{c1}$ many vortices penetrate into the film and to good approximation $\mathbf{B} = \mu_0\mathbf{H}$, which means that Eq. (2.15) applies. The strip can now be divided into three regions. The vortex-occupied outer regions $a_1 < |x| < W$ are in the critical state with $J_y = J_c$, and the inner region $|x| < a_1$ is screened from the induced magnetic field with $B_z = 0$. These two conditions define a boundary value problem which must be solved to determine $J_y(x)$ and $B_z(x)$. This problem has been solved for a constant J_c using conformal mapping methods [Norris, 1970],

$$J_y(x) = \begin{cases} \frac{2J_c}{\pi}\arctan\left(\sqrt{\frac{W^2-a_1^2}{a_1^2-x^2}}\right), & |x| < a_1, \\ J_c, & a_1 \le |x| < W, \end{cases} \tag{2.28}$$

$$B_z(x) = \begin{cases} 0, & |x| \le a_1, \\ -\frac{x}{|x|}B_f \ln\frac{\sqrt{W^2-x^2}}{\sqrt{W^2-a_1^2}-\sqrt{x^2-a_1^2}}, & a_1 < |x| < W, \\ -\frac{x}{|x|}B_f \ln\frac{\sqrt{x^2-W^2}}{\sqrt{x^2-a_1^2}-\sqrt{W^2-a_1^2}}, & |x| > W, \end{cases} \tag{2.29}$$

where

$$a = W\sqrt{1-(I_T/I_c)^2}, \tag{2.30}$$

and $I_c = J_c 2Wd$ is the saturation current of the strip. Figure 2.10 shows current and field profiles for several values of I_T. I now consider the case when the transport current is decreased from an initial

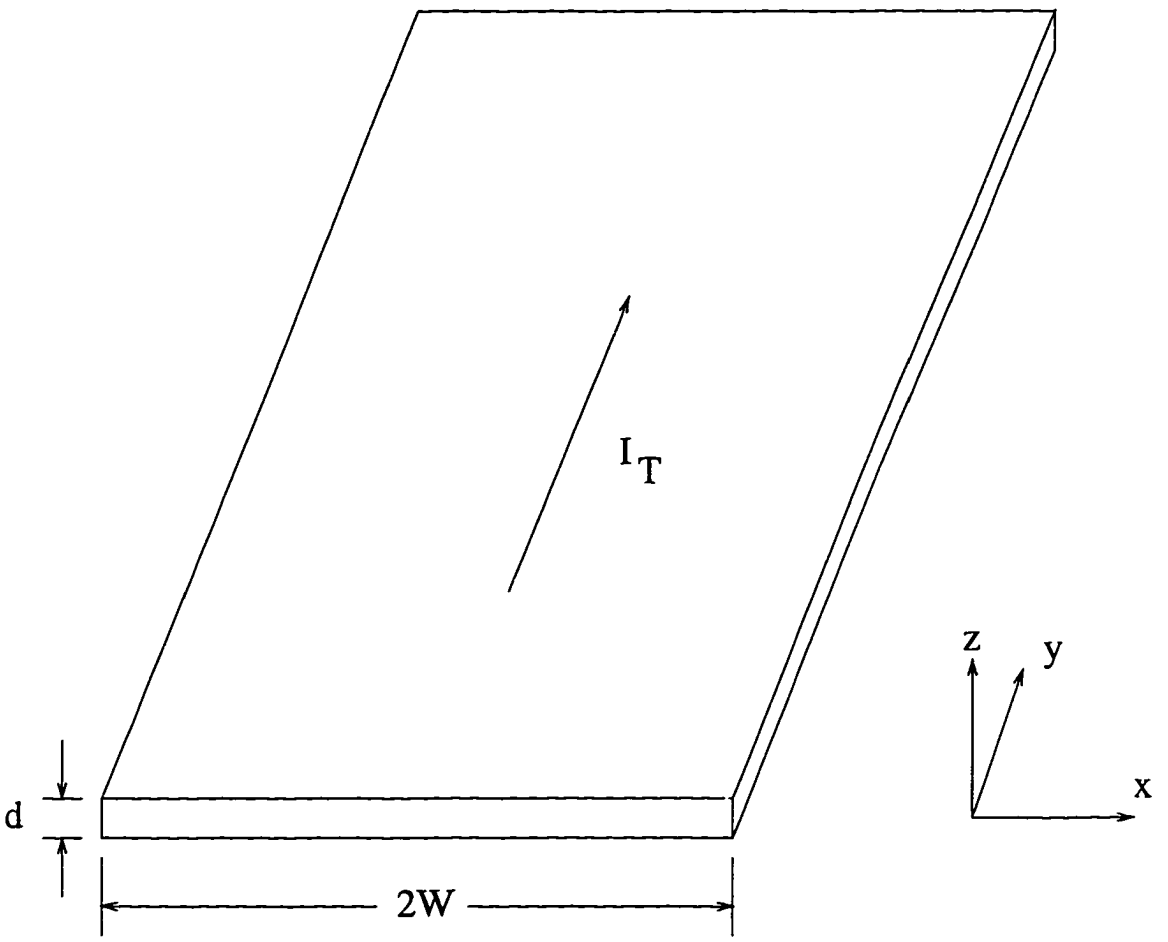

Figure 2.9 Superconducting strip (infinite along the y direction) of width $2W$ and thickness d carrying a transport current I_T in the positive y direction.

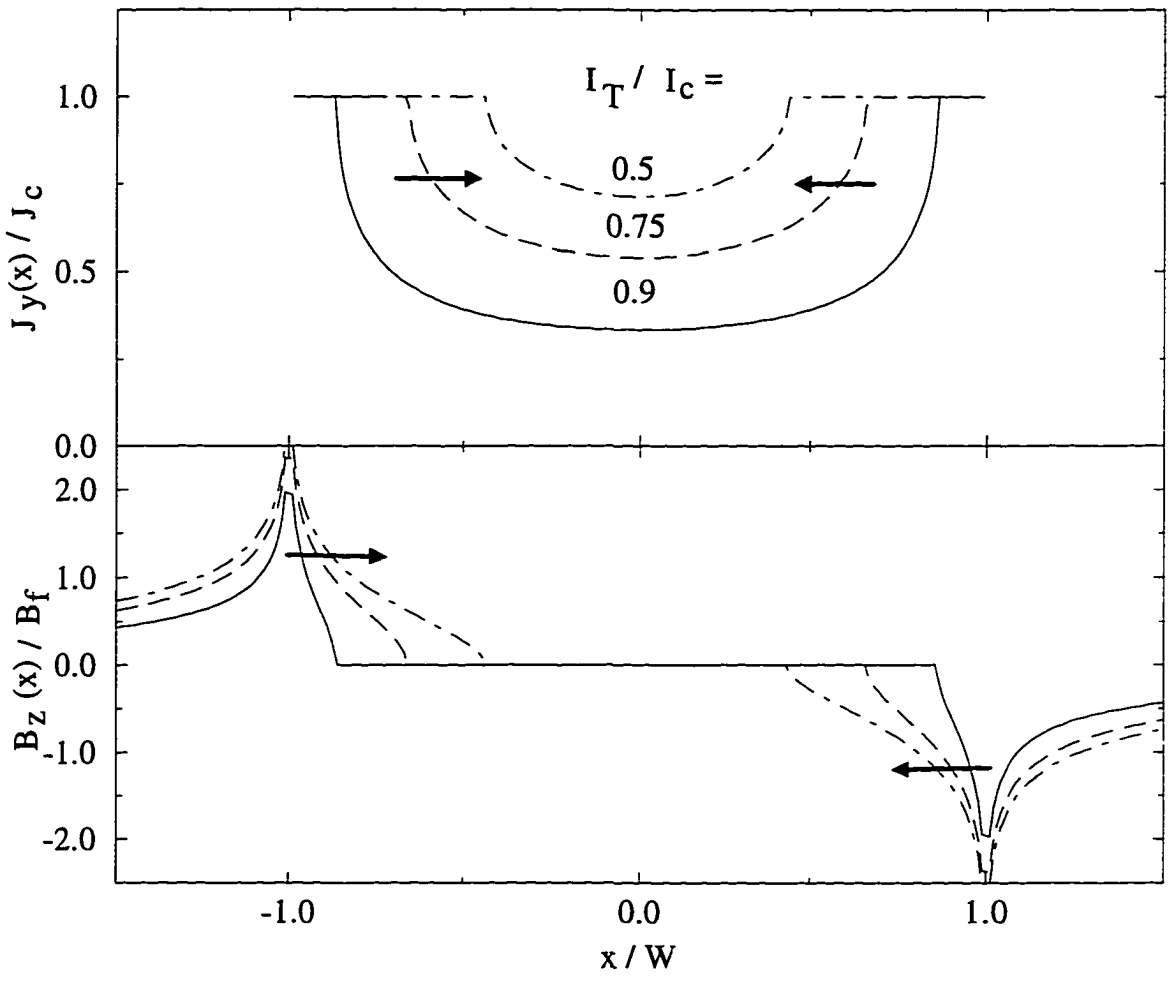

Figure 2.10 Current-density and flux-density profiles for flux penetration into a current carrying type-II superconducting strip initially in the virgin state. The arrows indicate the progression of profiles as the transport current is increased.

value I_{T0} to a new value I_T. Initially the current and flux densities are given by Eqs. (2.28-2.30) with I_T replaced by I_{T0} and a_1 replaced by a_0. After the current is decreased, the flux density will change in the two outer regions $a_1 < |x| < W$ but will remain the same in the inner region $x < a_1$. The current density will change across the entire width of the strip. The current and flux density profiles have been determined previously by a superposition method [Brandt and Indenbom, 1993, Zeldov et al., 1994]

$$J_y(x) = \begin{cases} \frac{2J_c}{\pi}\left[\arctan\left(\sqrt{\frac{W^2-a_0^2}{a_0^2-x^2}}\right) - 2\arctan\left(\sqrt{\frac{W^2-a_1^2}{a_1^2-x^2}}\right)\right], & |x| \le a_0, \\ J_c\left[1 - \frac{4}{\pi}\arctan\left(\sqrt{\frac{W^2-a_1^2}{a_1^2-x^2}}\right)\right], & a_0 < |x| \le a_1, \\ -J_c, & a_1 \le |x| < W, \end{cases} \tag{2.31}$$

and

$$B_z(x) = \begin{cases} 0, & |x| \le a_0, \\ -\frac{x}{|x|}B_f \ln\frac{\sqrt{W^2-x^2}}{\sqrt{W^2-a_0^2}-\sqrt{x^2-a_0^2}}, & a_0 < |x| \le a_1, \\ -\frac{x}{|x|}B_f\left(\ln\frac{\sqrt{|x^2-W^2|}}{\left|\sqrt{x^2-a_0^2}-\sqrt{W^2-a_0^2}\right|} - 2\ln\frac{\sqrt{|x^2-W^2|}}{\left|\sqrt{x^2-a_1^2}-\sqrt{W^2-a_1^2}\right|}\right), & |x| > a_1, \end{cases} \tag{2.32}$$

where

$$a_0 = W\sqrt{1-(I_{T0}/I_c)^2}, \tag{2.33}$$

and

$$a_1 = W\sqrt{1-\left(\frac{I_{T0}-I_T}{2I_c}\right)^2}. \tag{2.34}$$

Figure 2.11 shows the current and field profiles for several values of I_T between I_{T0} and $-I_{T0}$. If the transport current is then increased starting from $-I_{T0}$, the profiles are given by

$$J_y(x) = \begin{cases} -\frac{2J_c}{\pi}\left[\arctan\left(\sqrt{\frac{W^2-a_0^2}{a_0^2-x^2}}\right) - 2\arctan\left(\sqrt{\frac{W^2-a_1^2}{a_1^2-x^2}}\right)\right], & |x| \le a_0, \\ -J_c\left[1 - \frac{4}{\pi}\arctan\left(\sqrt{\frac{W^2-a_1^2}{a_1^2-x^2}}\right)\right], & a_0 < |x| \le a_1, \\ J_c, & a_1 \le |x| < W, \end{cases} \tag{2.35}$$

and

$$B_z(x) = \begin{cases} 0, & |x| \le a_0, \\ \frac{x}{|x|}B_f \ln\frac{\sqrt{W^2-x^2}}{\sqrt{W^2-a_0^2}-\sqrt{x^2-a_0^2}}, & a_0 < |x| \le a_1, \\ \frac{x}{|x|}B_f\left(\ln\frac{\sqrt{|x^2-W^2|}}{\left|\sqrt{x^2-a_0^2}-\sqrt{W^2-a_0^2}\right|} - 2\ln\frac{\sqrt{|x^2-W^2|}}{\left|\sqrt{x^2-a_1^2}-\sqrt{W^2-a_1^2}\right|}\right), & |x| > a_1, \end{cases} \tag{2.36}$$

where

$$a_1 = W\sqrt{1-\left(\frac{I_{T0}+I_T}{2I_c}\right)^2}. \tag{2.37}$$

These profiles are shown in Fig. 2.12.

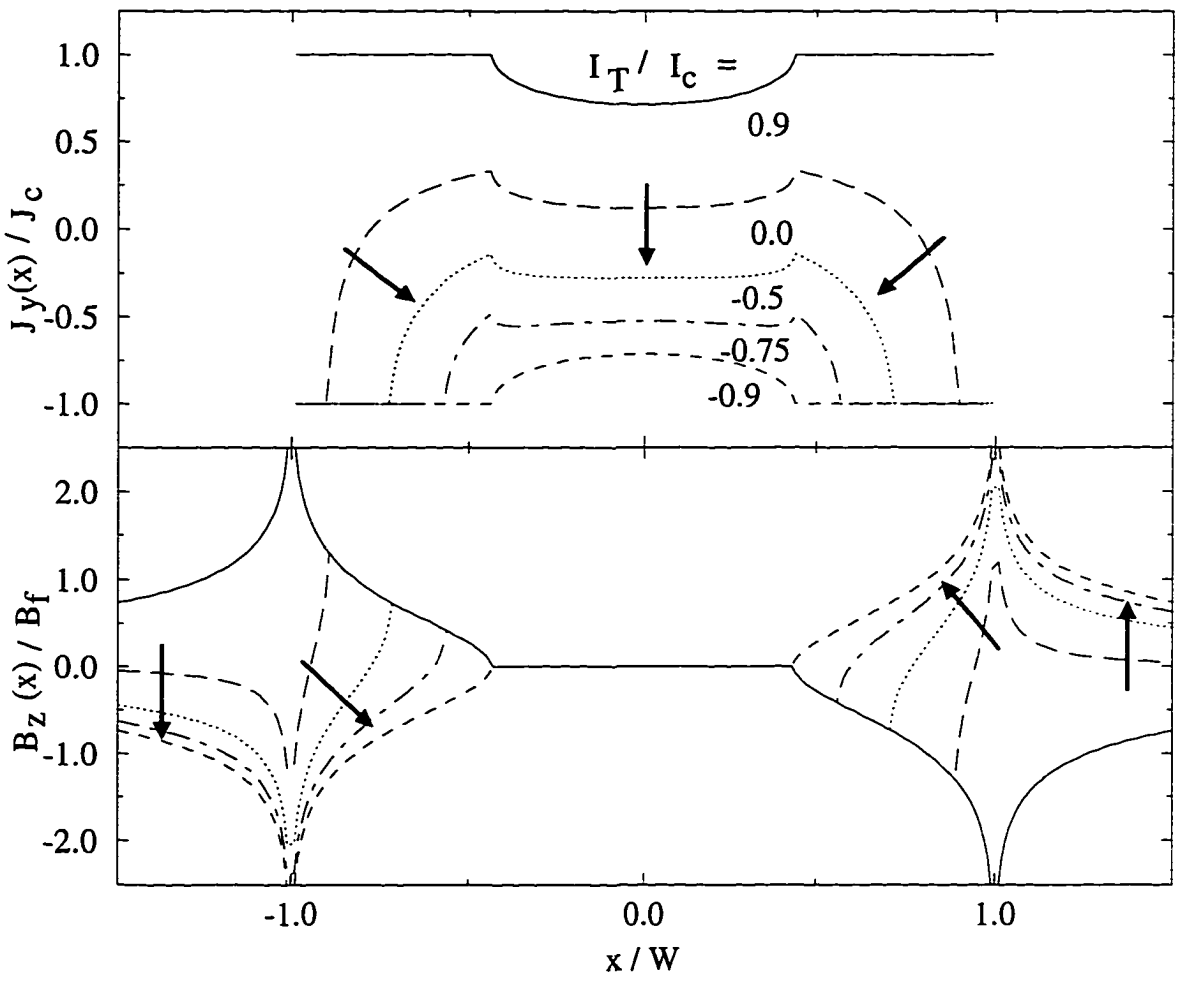

Figure 2.11 Current-density and flux-density profiles for flux penetration into a current carrying type-II superconducting strip as the transport current is decreased from I_{T0} to $-I_{T0}$. The arrows indicate the progression of profiles as the transport current is decreased.

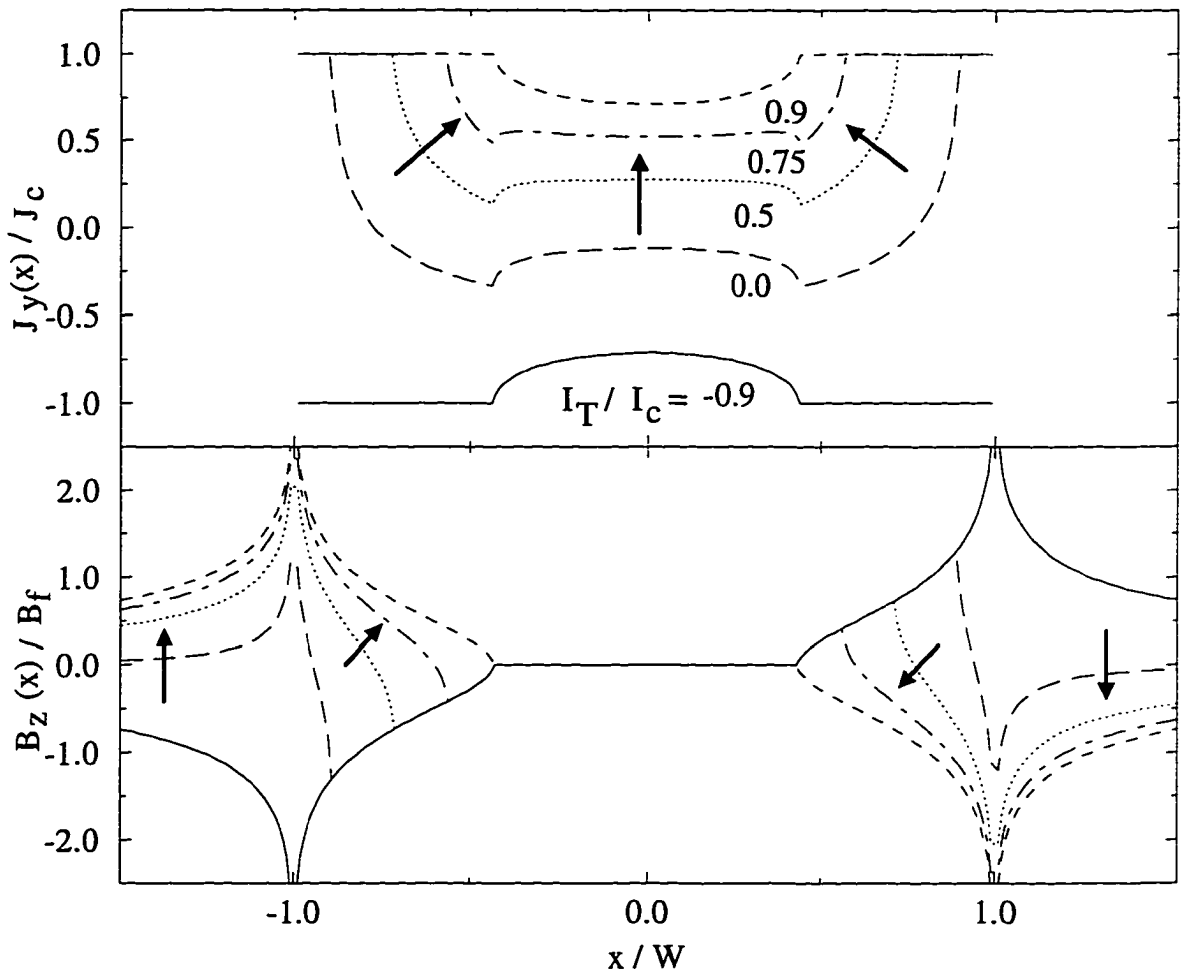

Figure 2.12 Current-density and flux-density profiles for flux penetration into a current carrying type-II superconducting strip as the transport current is increased from $-I_{T0}$ to I_{T0}. The arrows indicate the progression of profiles as the transport current is increased.

2.1.5 Superconducting wire of elliptical cross section carrying a transport current

In this section I consider the superconducting wire of elliptical cross section pictured in Fig. 2.13. The wire is infinitely long in the y direction (into the page) and has an elliptical cross section in the $x-z$ plane with semi-major axis a and semi-minor axis b. The aspect ratio of the ellipse is defined as $\alpha = b/a$ (when $\alpha = 1$ the wire is circular in cross section, while when $\alpha \ll 1$ the wire resembles a

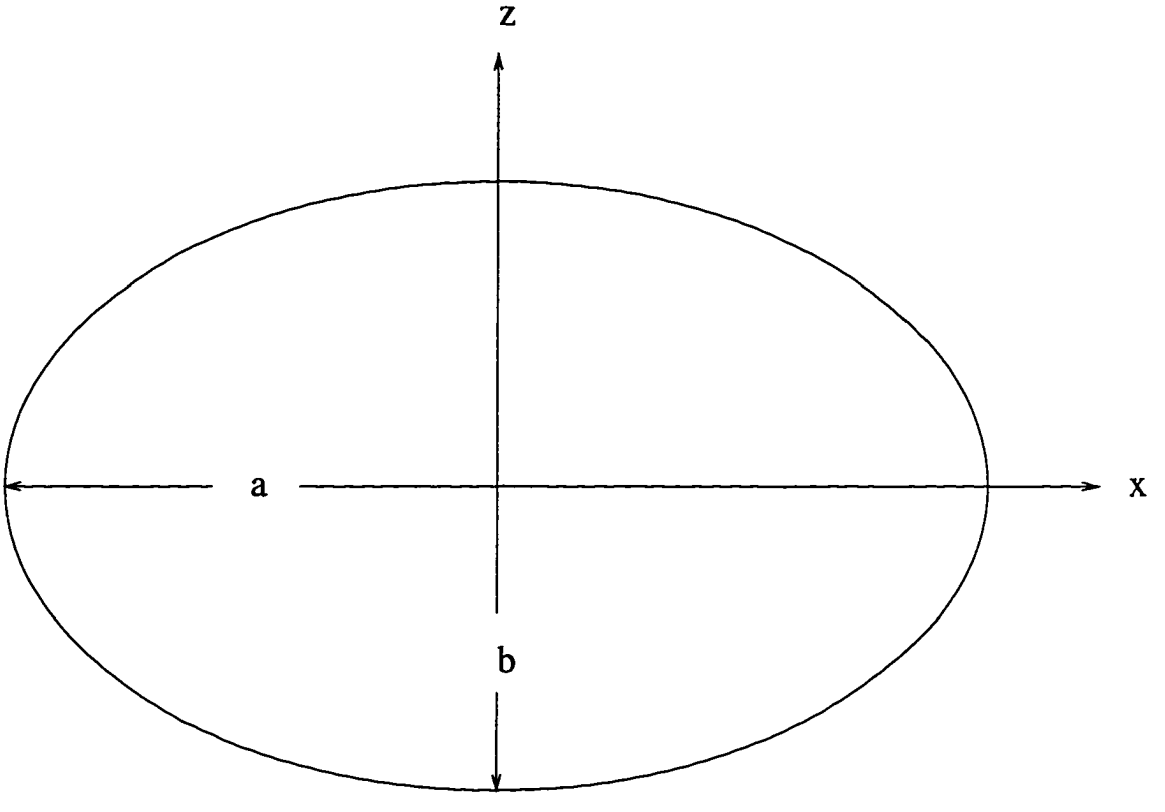

Figure 2.13 Cross section of an elliptical superconducting wire. The y axis is directed into the page. The wire is infinite in the y direction and has semi-major axis a and semi-minor axis b. There is a transport current I_T flowing along the wire in the positive y direction.

thin strip with elliptical rather than rectangular cross section). There is a transport current flowing along the wire in the y direction. I will assume that $H_{c1} = 0$, so that vortex penetration occurs for any $I_T > 0$, and that the London penetration depth λ satisfies the relation $\lambda \ll a, b$. When J_c is a constant the flux fronts will be ellipses which are concentric to the cross section of the wire (the aspect ratio of the flux front is $\alpha = b/a$) [Norris, 1970]. The wire can be divided into two regions. The outer region $a_1^2 < x^2 + y^2/\alpha^2 < a^2$ is in the critical state with $J_y = J_c$. The inner region $x^2 + y^2/\alpha^2 < a_1^2$ is screened from the induced magnetic field with $J_y = 0$ and $\mathbf{B} = 0$. The current-density and flux-density profiles

along the x axis have been determined previously [Norris, 1970]

$$J_y(x) = \begin{cases} 0\,, & 0 < x < a_1\,, \\ J_c\,, & a_1 < x < a\,, \end{cases} \tag{2.38}$$

and

$$B_z(x) = \begin{cases} 0\,, & 0 < x < a_1\,, \\ -B_e\left(\frac{x/a}{1+\alpha} - f(a_1)\right)\,, & a_1 < x < a\,, \\ -B_e\left(f(a) - f(a_1)\right)\,, & a < x\,, \end{cases} \tag{2.39}$$

where

$$f(u) = \frac{(u/a)^2}{x/a + \sqrt{(x/a)^2 - (1-\alpha^2)(u/a)^2}}\,, \tag{2.40}$$

and

$$a_1 = a\sqrt{1 - (I_T/I_c)}\,, \tag{2.41}$$

$I_c = \pi\alpha a^2 J_c$, and $B_e = \mu_0 \alpha J_c a$. Figures 2.14 and 2.15 show these profiles for the two extreme cases, $\alpha = 1$ (circular wire) and $\alpha \ll 1$ (film with elliptical cross section), for several values of I_T.

I now consider the case when the transport current is decreased from an initial value I_{T0} to a new value I_T. Initially the current and flux densities are given by Eqs. (2.38-2.41) with I_T replaced by I_{T0} and a_1 replaced by a_0. After the current is decreased, the current density and flux density will change in the outer region $a_1^2 < x^2 + y^2/\alpha^2$ but not in the inner region $x^2 + y^2/\alpha^2 < a_1^2$. The current-density and flux-density profiles can be determined using a superposition method

$$J_y(x) = \begin{cases} 0\,, & 0 < x < a_0\,, \\ J_c\,, & a_0 < x < a_1\,, \\ -J_c\,, & a_1 < x < a \end{cases} \tag{2.42}$$

and

$$B_z(x) = \begin{cases} 0\,, & 0 < x < a_1\,, \\ -B_e\left(\frac{x/a}{1+\alpha} - f(a_0)\right)\,, & a_0 < x < a_1\,, \\ -B_e\left(2f(a_1) - f(a_0) - \frac{x/a}{1+\alpha}\right)\,, & a_1 < x < a\,, \\ -B_e\left(2f(a_1) - f(a) - f(a_0)\right)\,, & x > a\,, \end{cases} \tag{2.43}$$

where

$$a_0 = a\sqrt{1 - (I_{T0}/I_c)}\,, \tag{2.44}$$

and

$$a_1 = a\sqrt{1 - \left(\frac{I_{T0} - I_T}{2I_c}\right)}\,. \tag{2.45}$$

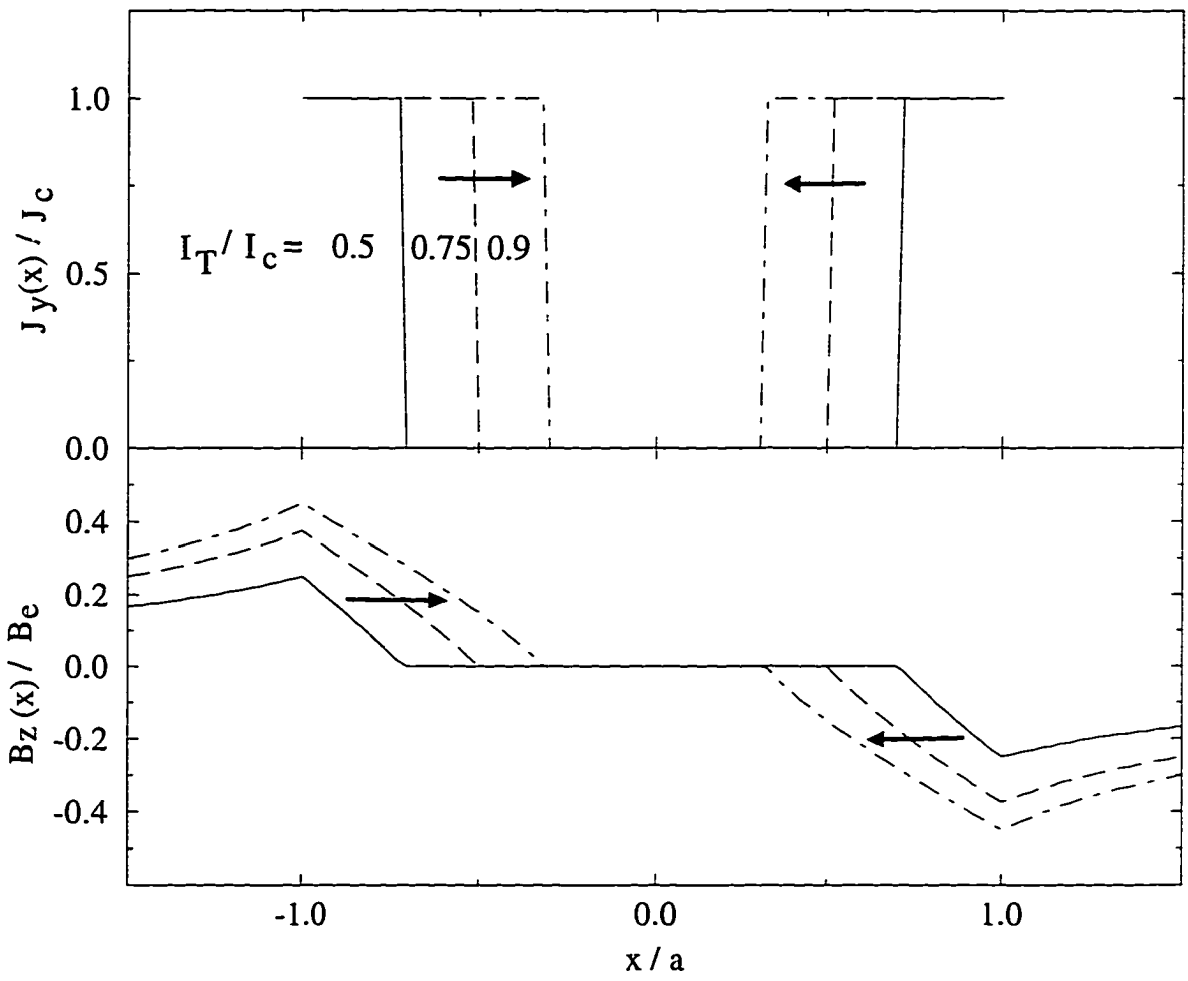

Figure 2.14 Current-density and flux-density profiles for flux penetration into a type-II superconducting wire of circular cross section ($\alpha = 1$) which is initially in the virgin state. The arrows indicate the progression of profiles as the transport current I_T is increased.

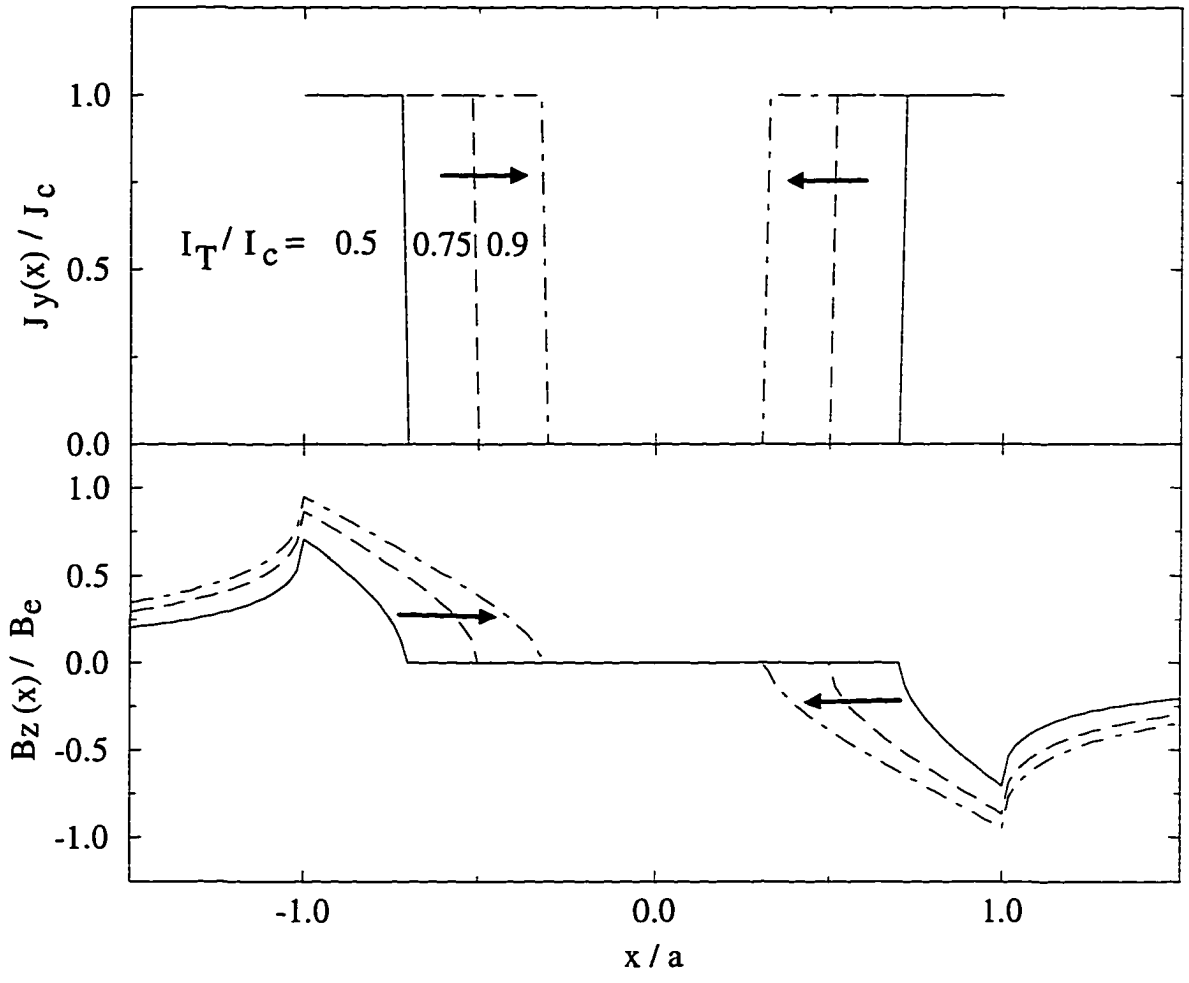

Figure 2.15 Current-density and flux-density profiles for flux penetration into a type-II superconducting strip of elliptical cross section ($\alpha \ll 1$) which is initially in the virgin state. The arrows indicate the progression of profiles as the transport current I_T is increased.

Figures 2.16 and 2.17 show the current and field profiles, when $\alpha = 1$ and $\alpha \ll 1$ respectively, for several values of I_T between I_{T0} and $-I_{T0}$. If the transport current is then increased starting from $-I_{T0}$, the profiles are given by

$$J_y(x) = \begin{cases} 0, & 0 < x < a_0, \\ -J_c, & a_0 < x < a_1, \\ J_c, & a_1 < x < a \end{cases} \tag{2.46}$$

and

$$B_z(x) = \begin{cases} 0, & 0 < x < a_1, \\ B_e\left(\frac{x/a}{1+\alpha} - f(a_0)\right), & a_0 < x < a_1, \\ B_e\left(2f(a_1) - f(a_0) - \frac{x/a}{1+\alpha}\right), & a_1 < x < a, \\ B_e\left(2f(a_1) - f(a) - f(a_0)\right), & x > a, \end{cases} \tag{2.47}$$

where

$$a_1 = a\sqrt{1 - \left(\frac{I_{T0} + I_T}{2I_c}\right)}. \tag{2.48}$$

These profiles are shown in Figs. 2.18 and 2.19 for $\alpha = 1$ and $\alpha \ll 1$ respectively.

2.2 Nonlinear surface impedance of a type-II superconducting half space

The surface impedance of a hard type-II superconductor in an alternating magnetic field can be calculated using the critical-state field profiles determined previously in Sec. 2.1.2. In order for the calculation to be valid it must be assumed that the frequency of the applied field is low enough that the response of the superconductor can be treated quasistatically. The surface impedance of a linear material $Z_s = R_s - iX_s$, where R_s and X_s are the surface resistance and surface reactance respectively, is defined as the proportionality constant between the tangential complex electric field and the tangential complex magnetic field at the surface of a half space of the material [Jackson, 1975]. The tangential magnetic field at the surface is equal to the applied magnetic field which is assumed to be harmonic. For a linear material, the tangential electric field at the surface will typically have components both in-phase and out-of-phase with the applied magnetic field. The in phase component of the electric field is proportional to R_s while the out of phase component is proportional to X_s. As an example consider a half space of normal metal characterized by a resistivity ρ and subjected to an applied field $H_a(t) = \mathrm{Re}\left[H_{a0}e^{-i\omega t}\right]$. The magnetic field inside of the metal is given by

$$B_z(x,t) = \mathrm{Re}\left[\mu_0 H_{a0} e^{-x/\delta} e^{i(x/\delta - \omega t)}\right], \tag{2.49}$$

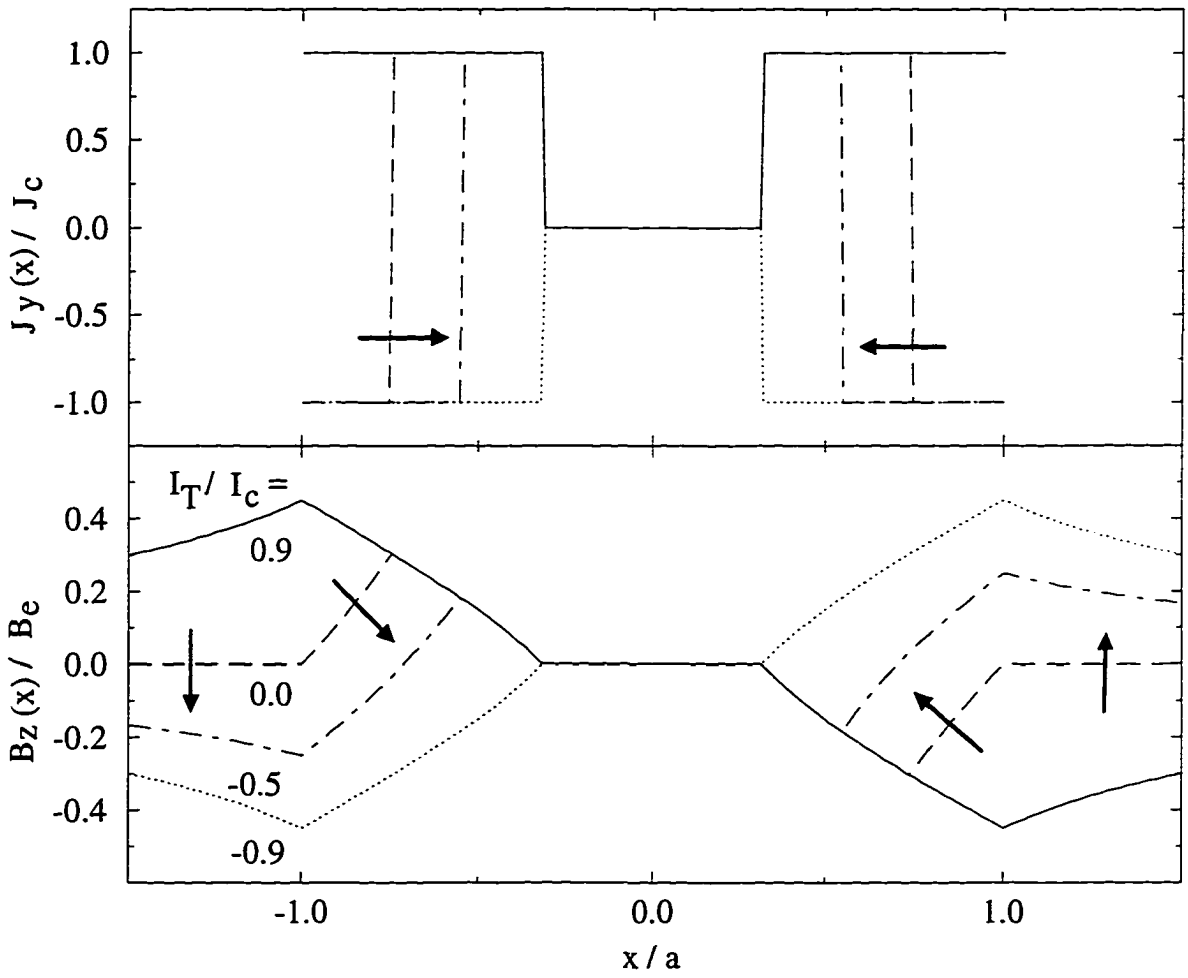

Figure 2.16 Current-density and flux-density profiles for flux penetration into a type-II superconducting wire of circular cross section ($\alpha = 1$) as the transport current is decreased from I_{T0} to $-I_{T0}$. The arrows indicate the progression of profiles as the transport current I_T is decreased.

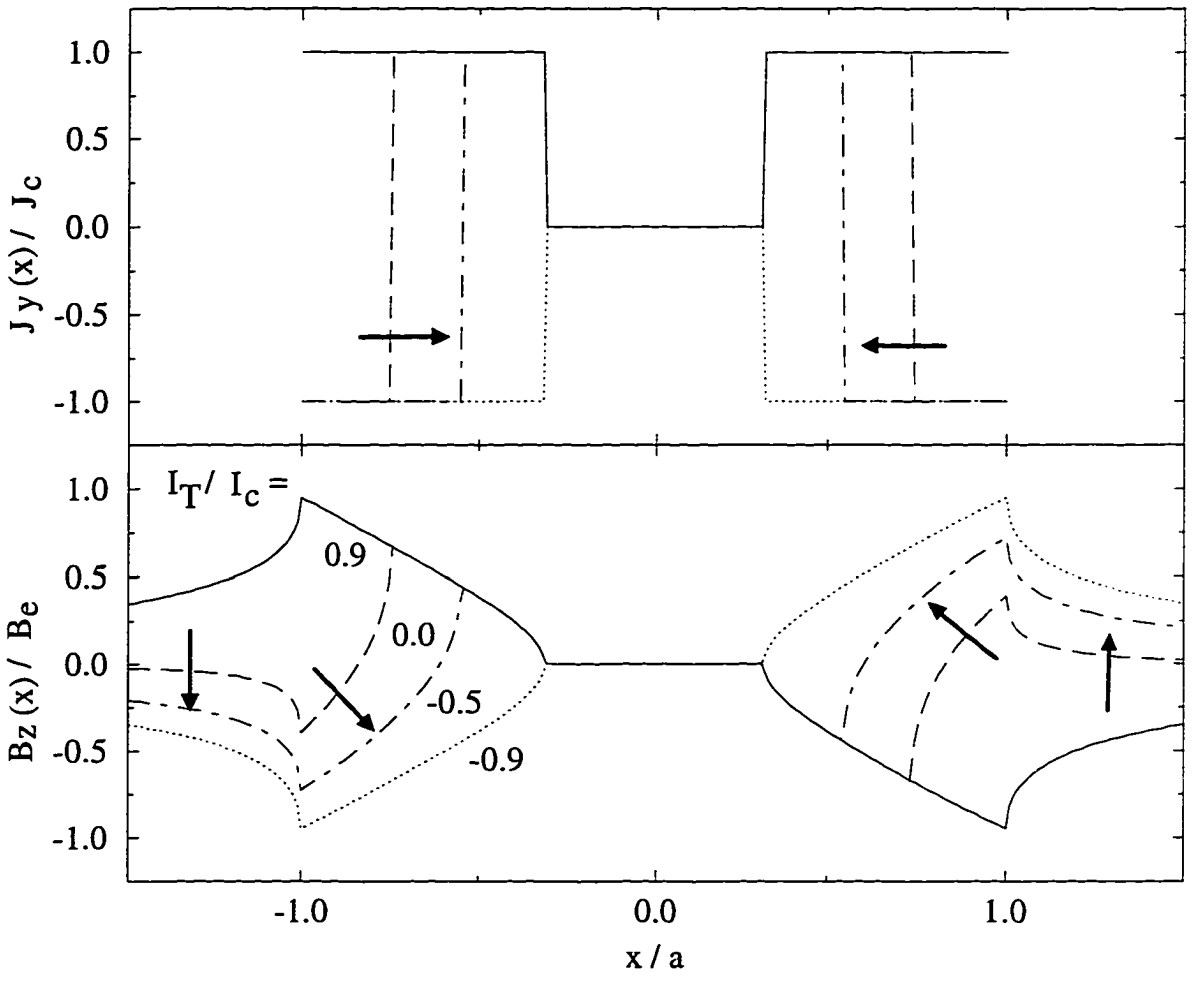

Figure 2.17 Current-density and flux-density profiles for flux penetration into a type-II superconducting strip of elliptical cross section ($\alpha \ll 1$) as the transport current is decreased from I_{T0} to $-I_{T0}$. The arrows indicate the progression of profiles as the transport current I_T is decreased.

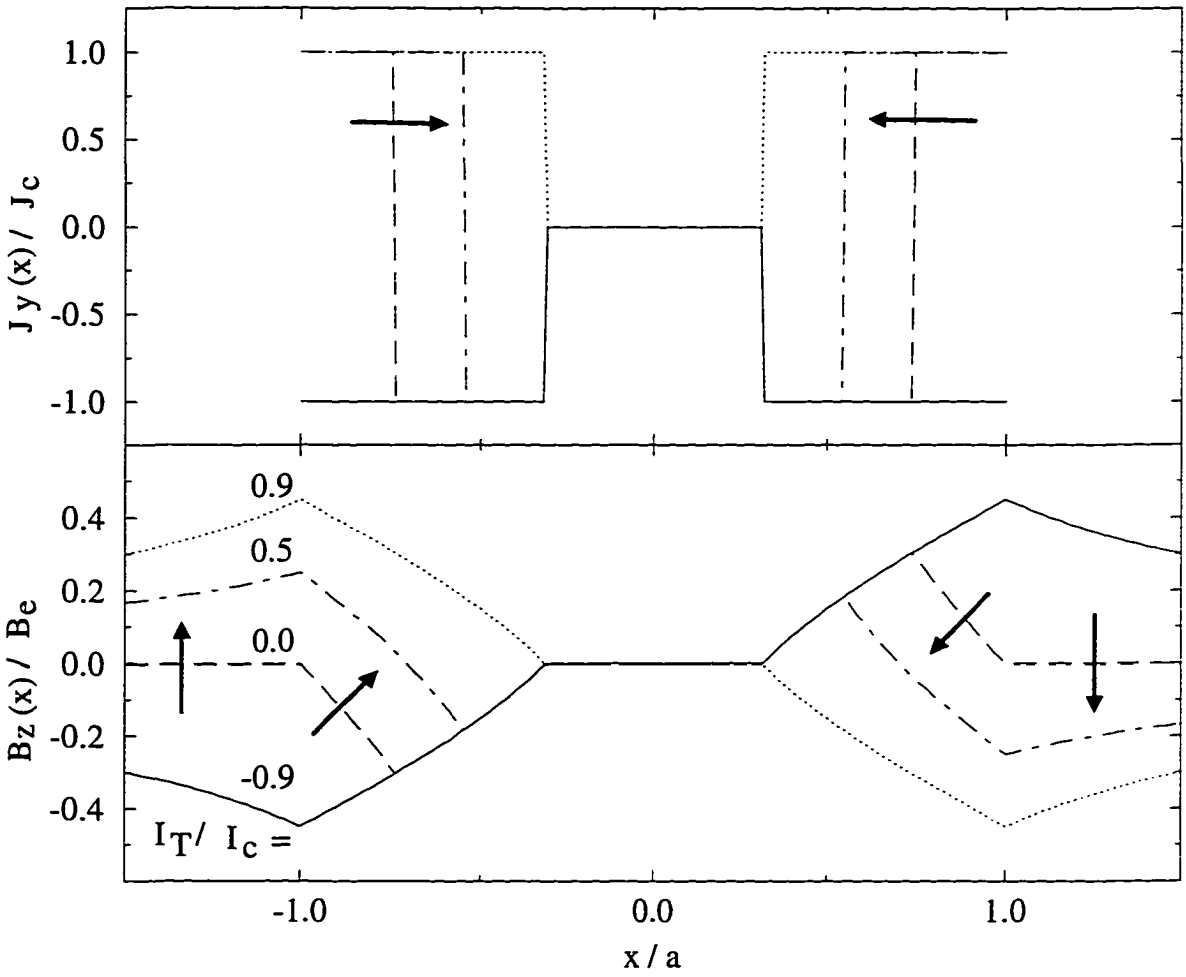

Figure 2.18 Current-density and flux-density profiles for flux penetration into a type-II superconducting wire of circular cross section ($\alpha = 1$) as the transport current is increased from $-I_{T0}$ to I_{T0}. The arrows indicate the progression of profiles as the transport current I_T is increased.

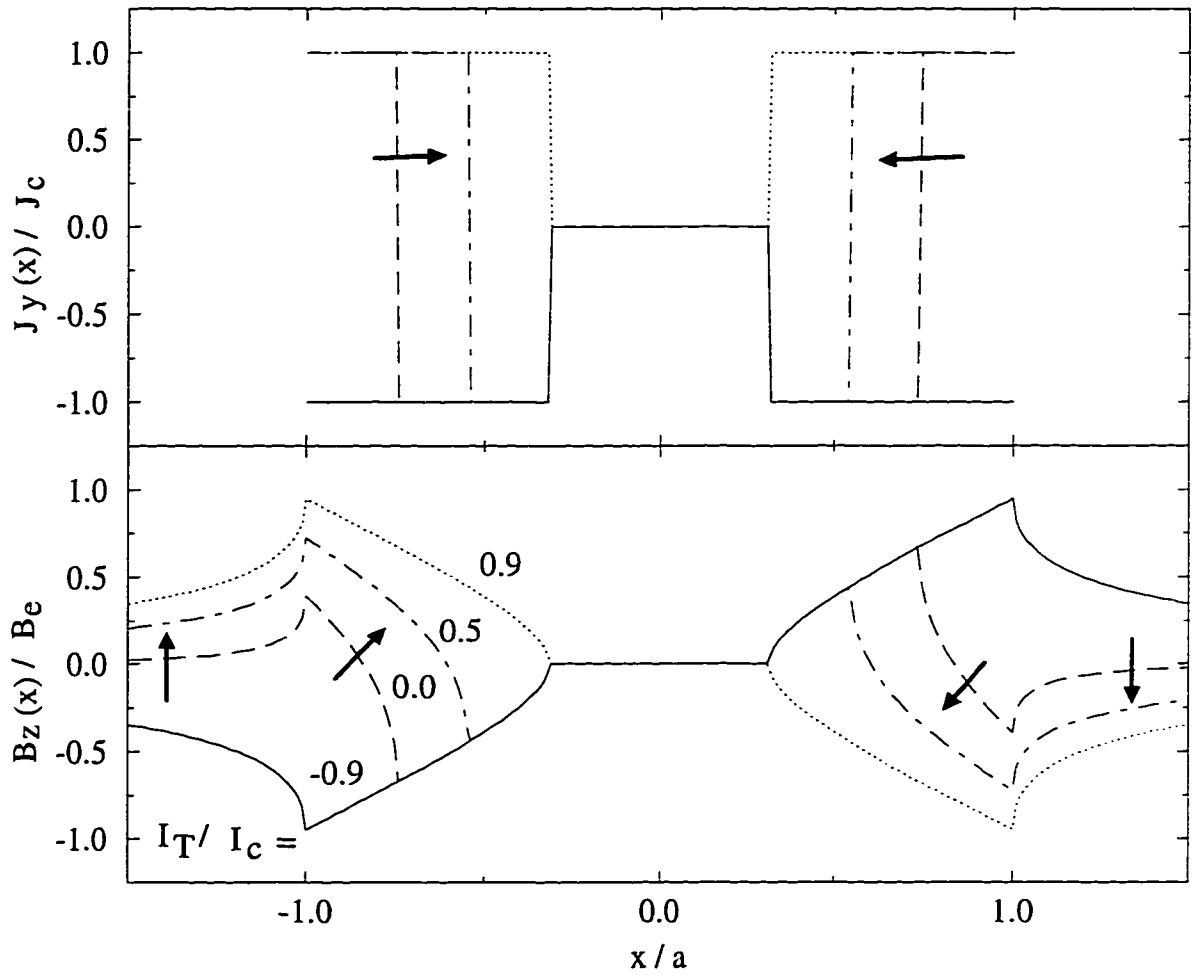

Figure 2.19 Current-density and flux-density profiles for flux penetration into a type-II superconducting strip of elliptical cross section ($\alpha \ll 1$) as the transport current is increased from $-I_{T0}$ to I_{T0}. The arrows indicate the progression of profiles as the transport current I_T is increased.

where $\delta = \sqrt{2\rho/\mu_0\omega}$ is the skin depth [Clem, 1992]. The electric field at the surface can be found by applying Stokes' theorem in the $x-y$ plane to Ampere's law $\nabla \times \mathbf{E} = -\frac{\partial \mathbf{B}}{\partial t}$. The result is

$$E_y(x=0,t) = \frac{d}{dt}\int_0^\infty B_z(x,t)dx\,. \tag{2.50}$$

Inserting the appropriate expression for $B_z(x,t)$ into Eq. (2.50) yields

$$E_y(x=0,t) = \mathrm{Re}\left[\rho/\delta(1-i)H_{a0}e^{-i\omega t}\right]\,. \tag{2.51}$$

The relation between the complex electric field $\tilde{E}_y(x=0,t)$ and the complex magnetic field $\tilde{H}_z(x=0,t)$ is $\tilde{E}_y(x=0,t) = \rho/\delta(1-i)\tilde{H}_z(x=0,t)$. Therefore, $Z_s = (1-i)\rho/\delta$.

In a nonlinear material the application of a harmonic magnetic field will typically generate higher harmonics in the electric field. Therefore, the surface impedance concept must be generalized in nonlinear materials. One method is to expand the electric field at the surface in a Fourier series,

$$E_y(x=0,t) = H_{a0}\sum_{n=0}^{\infty}\left[R_n\cos(n\omega t) - X_n\sin(n\omega t)\right]\,, \tag{2.52}$$

where

$$R_n = \frac{\omega}{\pi H_{a0}}\int_0^{2\pi/\omega}\cos(n\omega t)E_y(x=0,t)dt\,, \tag{2.53}$$

and

$$X_n = -\frac{\omega}{\pi H_{a0}}\int_0^{2\pi/\omega}\sin(n\omega t)E_y(x=0,t)dt\,. \tag{2.54}$$

R_1 and X_1 are the surface resistance and surface reactance of the material respectively, while the coefficients for larger n provide information about the higher harmonics that are generated.

Returning to the superconduting half space, the magnetic flux density is given by Eqs. (2.6-2.12). The resulting electric field, calculated from Eq. (2.52), is

$$E_y(x=0,t) = \begin{cases} \frac{\omega B_{a0}^2}{2\mu_0 J_c}\left(\frac{1}{2}\sin(2\omega t) - \sin(\omega t)\right)\,, & 0 < t < \pi/\omega\,, \\ -\frac{\omega B_{a0}^2}{2\mu_0 J_c}\left(\frac{1}{2}\sin(2\omega t) + \sin(\omega t)\right)\,, & \pi/\omega < t < 2\pi/\omega\,. \end{cases} \tag{2.55}$$

The Fourier coefficients calculated from Eqs. (2.15) and (2.16) are

$$R_n = \begin{cases} -\frac{B_{a0}\omega}{\pi J_c}\frac{1-(-1)^n}{n^2-4}\,, & n \text{ odd}\,, \\ 0\,, & n \text{ even}\,, \end{cases} \tag{2.56}$$

and

$$X_n = \begin{cases} \frac{B_{a0}\omega}{2J_c}\,, & n = 1\,, \\ 0\,, & \text{other } n\,. \end{cases} \tag{2.57}$$

The surface impedance of the superconductor is given by [Fisher et al., 1992]

$$Z_s = \frac{2B_{a0}\omega}{3\pi J_c}(1 - i3\pi/4)\,. \tag{2.58}$$

It is clear from Eq. (2.58) that the surface resistance for a type-II superconductor is proportional to the amplitude of the applied field; this is in contrast to a normal metal where the surface resistance is a constant [Jackson, 1975].

2.3 Harmonic generation and intermodulation due to alternating transport currents

2.3.1 Harmonic generation in strips and elliptical wires

In this section I consider harmonic generation (HG) in a one-dimensional coaxial-type transmission line as shown in Fig. 2.20 [Sridhar, 1994]. The outer conductor is a superconducting cylindrical shell of radius R, and the inner conductor is either a superconducting wire of elliptical cross section or a superconducting thin-film strip. The center conductor carries a transport current $I_T(t) = I_{T0}\cos(\omega_0 t)$. I will assume that R is large enough that the center conductor can be treated as if it were isolated. It can be shown that this is not a very restrictive assumption [Campbell, 1995, Clem et al., 1996, Fleshler et al., 1995]. When I_{T0} becomes large enough, vortices will penetrate into the center conductor. In these calculations I will assume that $H_{c1} = 0$ and that there are no surface barriers, so vortex penetration occurs for all $I_{T0} > 0$. For simplicity I will neglect any flux penetration into the outer conductor. I will also assume that ω_0 is small enough that the vortex motion can be treated quasistatically, which will allow me to use the results of Secs. 2.1.4 and 2.1.5.

The voltage drop per unit length is given by Faraday's law

$$V(t) = -\frac{d}{dt}\int_0^R dx B_z(x,t)\,, \tag{2.59}$$

where B_z is the z component of the flux density in the $x-y$ plane. Since $I_T(t)$ is periodic with period $T = 2\pi/\omega_0$, $V(t)$ is periodic with the same period. I may, therefore, express $V(t)$ as a Fourier series

$$V(t) = I_{T0}\sum_{n=1}^{\infty}\left[R_n\cos(n\omega_0 t) - X_n\sin(n\omega_0 t)\right]\,, \tag{2.60}$$

where the coefficients R_n and X_n are given by

$$R_n = \frac{\omega_0}{\pi I_{T0}}\int_0^{2\pi/\omega_0} dt V(t)\cos(n\omega_0 t)\,, \tag{2.61}$$

$$X_n = -\frac{\omega_0}{\pi I_{T0}}\int_0^{2\pi/\omega_0} dt V(t)\sin(n\omega_0 t)\,, \tag{2.62}$$

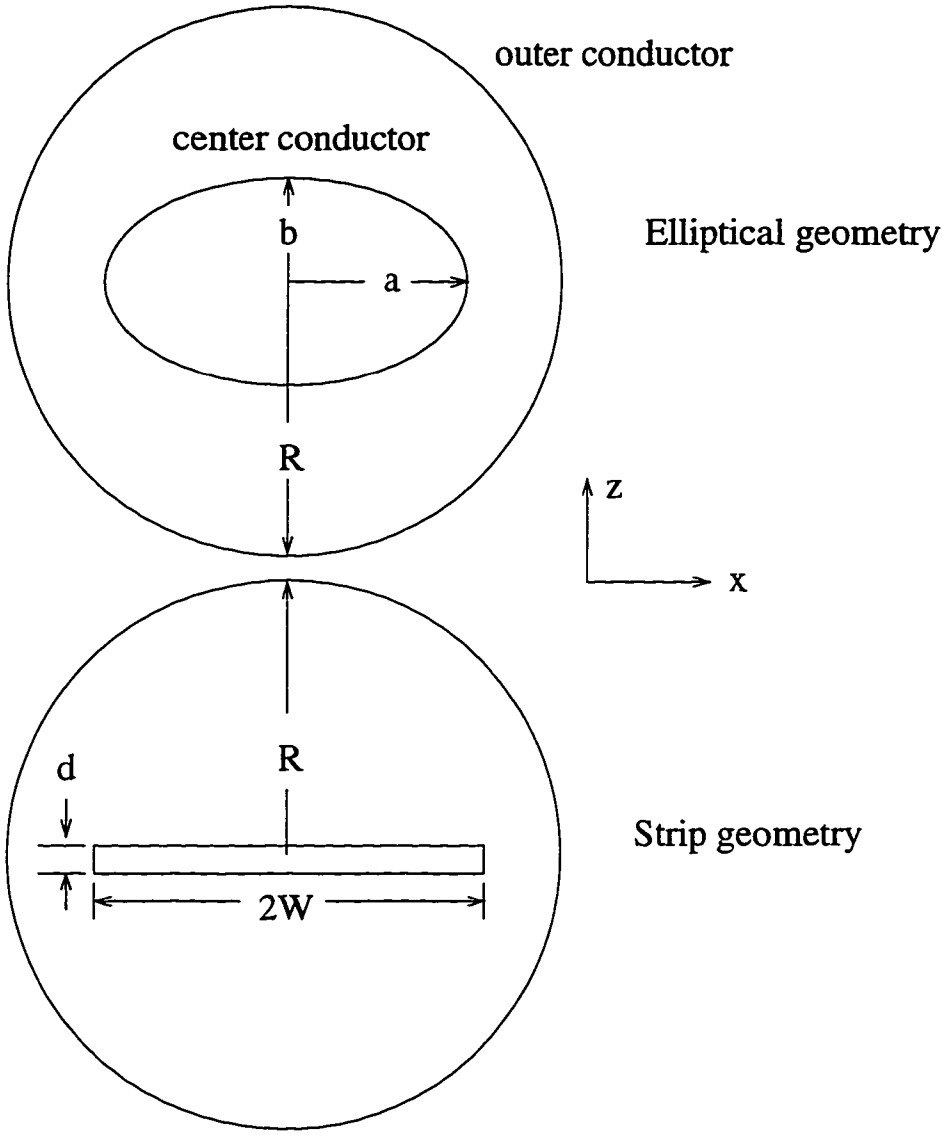

Figure 2.20 Picture of superconducting coaxial-type transmission lines. The outer conductor is a cylindrical shell of radius R. The center conductor is either an elliptical wire with aspect ratio $\alpha = b/a$ or a thin-film strip of width $2W$ and thickness d, where $a, W \ll R$. The y axis points into the page.

respectively. The dissipated power per unit length is given by

$$P_{diss} = \frac{\omega_0}{2\pi}\int_0^{2\pi/\omega_0} dt I_T(t)V(t)\,. \tag{2.63}$$

Inserting Eq. (2.60) into Eq. (2.63) yields

$$P_{diss} = \frac{1}{2}I_{T0}^2 R_1\,. \tag{2.64}$$

Equation (2.64) implies that R_1 is the resistance per unit length. X_1 is the reactance per unit length, which is related to the inductance and to the resonant frequency. When $I_{T0} \to 0$, $V(t)$ becomes purely inductive; therefore, $X_1 \to X_0$, where X_0 is the geometric reactance per unit length. For $n > 1$, R_n and X_n yield information on the generation of higher harmonics in the transmission line.

I will first consider the strip geometry. During the half cycle when I_T is decreasing from I_{T0} to $-I_{T0}$, the current-density and flux-density profiles are given by Eqs. (2.31-2.34). During the other half cycle I_T is increasing from $-I_{T0}$ to I_{T0}, and the current-density and flux-density profiles are given by Eqs. (2.35-2.37). Inserting $I_T = I_{T0}\cos(\omega_0 t)$ into Eqs. (2.34) and (2.37) results in

$$a_1(t) = \begin{cases} W\sqrt{1 - I^2\sin^4(\omega_0 t/2)}\,, & 0 < t < \pi/\omega_0\,, \\ W\sqrt{1 - I^2\cos^4(\omega_0 t/2)}\,, & \pi/\omega_0 < t < 2\pi/\omega_0\,, \end{cases} \tag{2.65}$$

If the expressions for B_z given in Eqs. (2.32) and (2.36) are used in Eq. (2.59) to calculate $V(t)$, the result is

$$V(t) = -I_{T0}\frac{\mu_0\omega_0}{2\pi}\sin(\omega_0 t)\ln\left(\frac{R + \sqrt{R^2 - a_1(t)^2}}{a_1(t)}\right)\,. \tag{2.66}$$

The logarithm can be expanded around large R to obtain

$$V(t) = I_{T0}\frac{\mu_0\omega_0}{2\pi}\sin(\omega_0 t)\left[-\ln\left(\frac{2R}{W}\right) + \ln\left(\frac{a_1(t)}{W}\right) + O\left(\left(\frac{(a_1(t))}{R}\right)^2\right)\right]\,. \tag{2.67}$$

The first term is the voltage drop per unit length when the strip is in the Meissner state. The second term is the dominant nonlinear term, and the third term leads to small corrections and will be neglected. The expressions for R_1 and X_1 are found to be

$$R_1 = \frac{\mu_0\omega_0}{2\pi}\frac{2}{\pi I^2}\left[(1+I)\ln(1+I) + (1-I)\ln(1-I) - I^2\right]\,, \tag{2.68}$$

which yields Norris' result for the losses in a thin-film strip [Norris, 1970]

$$P_{diss} = \frac{\omega_0}{2\pi}\frac{\mu_0 I_c^2}{\pi}\left[(1+I)\ln(1+I) + (1-I)\ln(1-I) - I^2\right]\,, \tag{2.69}$$

and

$$X_1 = X_0 + \Delta X_1\,, \tag{2.70}$$

where ΔX_1 is given by

$$\Delta X_1 = -\frac{\mu_0\omega_0}{4\pi}\left[1+\frac{2\left(4-(2-I)\sqrt{1-I}-(2+I)\sqrt{1+I}\right)}{I^2} +\ln\left(\frac{(2-I+2\sqrt{1-I})(2+I+2\sqrt{1+I})}{16}\right)\right], \tag{2.71}$$

and

$$X_0 = \frac{\mu_0\omega_0}{2\pi}\ln\left(\frac{2R}{W}\right). \tag{2.72}$$

The coefficients for the higher harmonics can be calculated analytically. The even harmonics vanish

$$R_{2n} = X_{2n} = 0, \tag{2.73}$$

while the expressions for the third harmonics are given by

$$R_3 = \frac{\mu_0\omega_0}{2\pi}\frac{1}{3\pi I^4}\left[2I^4-144I^2+\left(48(1+I)+6I^2\right)(1+I)\ln(1+I) +\left(48(1-I)+6I^2\right)(1-I)\ln(1-I)\right], \tag{2.74}$$

and

$$X_3 = \frac{\mu_0\omega_0}{2\pi}\frac{1}{4I^4}\left[I^4-144I^2-128+32(I^2-3I+2)\sqrt{1-I}+32(2+I)\sqrt{(1+I)^3}\right]. \tag{2.75}$$

The leading order behaviors for $I \ll 1$ are

$$R_1 = \frac{\mu_0\omega_0}{2\pi}\frac{I^2}{3\pi}, \tag{2.76}$$

$$\Delta X_1 = \frac{\mu_0\omega_0}{4\pi}\left(\frac{5I^2}{16}\right), \tag{2.77}$$

$$R_3 = \frac{\mu_0\omega_0}{2\pi}\left(-\frac{I^2}{5\pi}\right), \tag{2.78}$$

$$X_3 = \frac{\mu_0\omega_0}{2\pi}\frac{I^2}{32}. \tag{2.79}$$

Figure 2.21 shows R_1, ΔX_1, R_3, and X_3 as a function of I for the strip geometry.

I now consider the elliptical geometry. When I_T is decreasing from I_{T0} to $-I_{T0}$ the current-density and flux-density profiles are given by Eqs. (2.42-2.45). When I_T is increasing from $-I_{T0}$ to I_{T0} the current-density and flux-density profiles are given by Eqs. (2.46-2.48). Inserting $I_T = I_{T0}\cos(\omega_0 t)$ into Eqs. (2.45) and (2.48) yields

$$a_1(t) = \begin{cases} a\sqrt{1-I\sin^2(\omega_0 t/2)}, & 0 < t < \pi/\omega_0, \\ a\sqrt{1-I\cos^2(\omega_0 t/2)}, & \pi/\omega_0 < t < 2\pi/\omega_0. \end{cases} \tag{2.80}$$

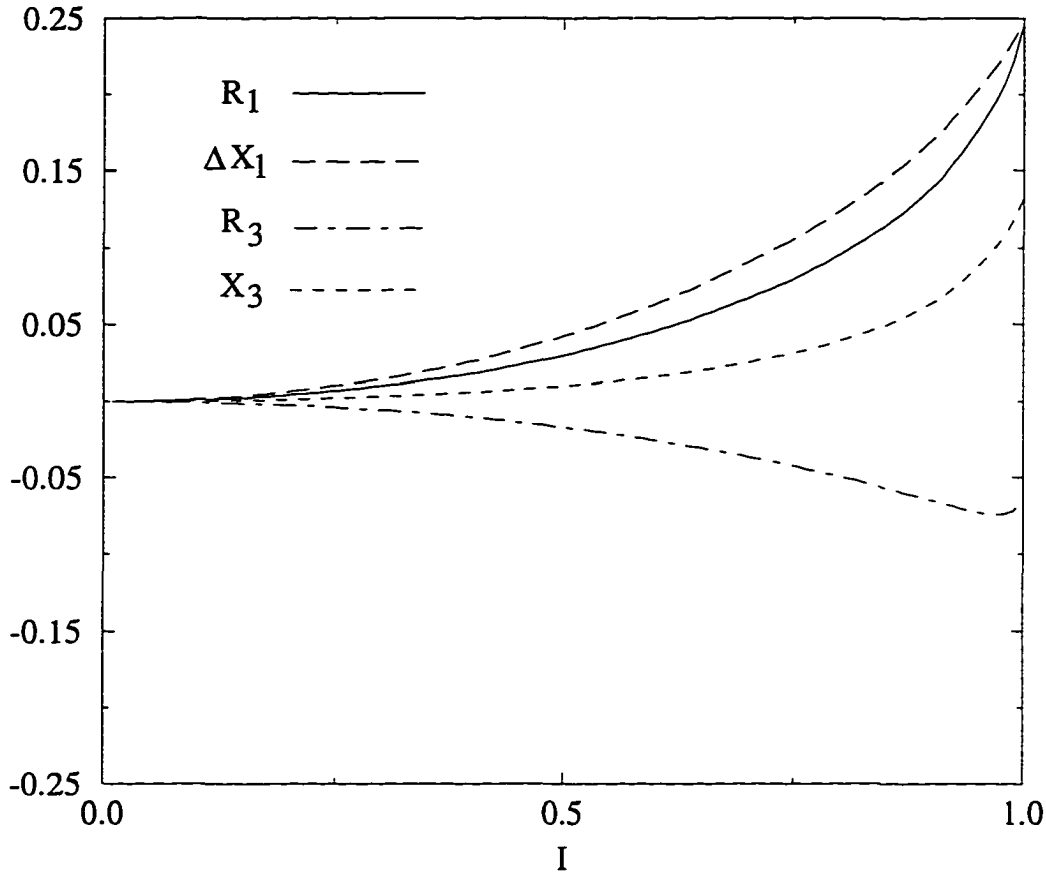

Figure 2.21 The resistance per unit length R_1, power-dependent part of the reactance per unit length ΔX_1, and third harmonics R_3 and X_3, in units of $\mu_0\omega_0/2\pi$, versus $I = I_{T0}/I_c$ for a superconducting strip transmission line.

If the expressions in Eqs. (2.43) and (2.47) are used in Eq. (2.32), then the result for $V(t)$ is

$$V(t) = -I_{T0}\frac{\mu_0\omega_0}{2\pi}\sin(\omega_0 t)\ln\left(\frac{R+\sqrt{R^2-(1-\alpha^2)a_1(t)^2}}{(1+\alpha)a_1(t)}\right) . \tag{2.81}$$

The logarithm can be expanded around large R to obtain

$$V(t) = I_{T0}\frac{\mu_0\omega_0}{2\pi}\sin(\omega_0 t)\left[-\ln\left(\frac{2}{(1+\alpha)}\frac{R}{a}\right)+\ln\left(\frac{a_1(t)}{a}\right)+O\left(\left(\frac{(a_1(t))}{R}\right)^2\right)\right] . \tag{2.82}$$

The first term is the voltage drop per unit length in the absence of vortex penetration ($I_{T0}\to 0$). The second term is the dominant term arising from the quasistatic vortex penetration. It is interesting to note that this term is independent of α. The third term leads to small corrections and will be neglected.

Using Eqs. (2.59) to calculate R_1, we find

$$R_1 = \frac{\mu_0\omega_0}{2\pi}\frac{1}{\pi I^2}\left[I(2-I)+2(1-I)\ln(1-I)\right] . \tag{2.83}$$

Inserting Eq. (2.83) into Eq. (2.62), we obtain Norris' result for the losses in an elliptical wire [Norris. 1970]

$$P_{diss} = \frac{\omega_0}{2\pi}\frac{\mu_0 I_c^2}{\pi}\left[I(1-I/2)+(1-I)\ln(1-I)\right] . \tag{2.84}$$

Using Eq. (2.60) to calculate X_1 we obtain

$$X_1 = X_0 + \Delta X_1 , \tag{2.85}$$

where ΔX_1 is given by

$$\Delta X_1 = \frac{\mu_0\omega_0}{4\pi}\left[-\frac{1}{2}+\frac{2\sqrt{1-I}(2-I-2\sqrt{1-I})}{I^2}-\ln\left(\frac{2-I+2\sqrt{1-I}}{4}\right)\right] , \tag{2.86}$$

and

$$X_0 = \frac{\mu_0\omega_0}{2\pi}\ln\left(\frac{2}{(1+\alpha)}\frac{R}{a}\right) . \tag{2.87}$$

ΔX_1 is the power-dependent or nonlinear part of the reactance, while X_0 is the geometric reactance. The coefficients for all higher harmonics can be calculated analytically. For the even harmonics it is found that

$$R_{2n} = X_{2n} = 0 . \tag{2.88}$$

The expressions for R_3 and X_3 are

$$R_3 = \frac{\mu_0\omega_0}{2\pi}\frac{1}{3\pi I^4}\left[48I-72I^2+22I^3+I^4+\left(48(1-I)+6I^2\right)(1-I)\ln(1-I)\right] , \tag{2.89}$$

and

$$X_3 = \frac{\mu_0\omega_0}{2\pi}\frac{1}{8I^4}\left[I^4+16I^3-144I^2+256I-128+64(2-I)\sqrt{(1-I)^3}\right] , \tag{2.90}$$

respectively. The leading order behaviors for $I \ll 1$ are

$$R_1 = \frac{\mu_0\omega_0}{2\pi}\frac{I}{3\pi}, \tag{2.91}$$

$$\Delta X_1 = \frac{\mu_0\omega_0}{4\pi}\frac{I}{2}, \tag{2.92}$$

$$R_3 = \frac{\mu_0\omega_0}{2\pi}\left(-\frac{I}{5\pi}\right), \tag{2.93}$$

$$X_3 = \frac{\mu_0\omega_0}{2\pi}\frac{I^2}{64}. \tag{2.94}$$

Figure 2.22 shows R_1, ΔX_1, R_3, and X_3 versus I for the elliptical geometry.

2.3.2 Two-frequency intermodulation in strips and elliptical wires

In this section I consider intermodulation (IM) in a one-dimensional coaxial-type transimission line shown in Fig. 2.20. The inner conductor carries a transport current with two closely spaced frequencies ω_1 and ω_2 centered around the resonant frequency ω_0,

$$I_T(t) = \frac{I_{T0}}{2}\left(\cos(\omega_1 t) + \cos(\omega_2 t)\right), \tag{2.95}$$

which can also be written as

$$I_T(t) = I_{T0}\cos(\omega_0 t)\cos(\Delta\omega t), \tag{2.96}$$

where $\omega_1 = \omega_0 + \Delta\omega$ and $\omega_2 = \omega_0 - \Delta\omega$. I will again assume that $H_{c1} = 0$ so that vortex penetration will occur for all $I_{T0} > 0$.

The voltage drop per unit length is again given by Eq. (2.57). If I assume that $\omega_0/\Delta\omega = N =$ integer, then I_T and $V(t)$ are periodic with period $T = 2\pi/\Delta\omega$. Therefore, $V(t)$ may again be written as a Fourier series

$$V(t) = I_{T0}\sum_{n=1}^{\infty}\left[R_n\cos(n\Delta\omega t) - X_n\sin(n\Delta\omega t)\right], \tag{2.97}$$

where the coefficients R_n and X_n are given by

$$R_n = \frac{\Delta\omega}{\pi I_{T0}}\int_0^{2\pi/\Delta\omega} dt V(t)\cos(n\Delta\omega t), \tag{2.98}$$

and

$$X_n = \frac{-\Delta\omega}{\pi I_{T0}}\int_0^{2\pi/\Delta\omega} dt V(t)\sin(n\Delta\omega t), \tag{2.99}$$

respectively. Since $\omega_1 = (N+1)\Delta\omega$ and $\omega_2 = (N-1)\Delta\omega$, the fundamental response will be given by the $n = N+1$ and $n = N-1$ terms in the series. The third order intermodulation response, at

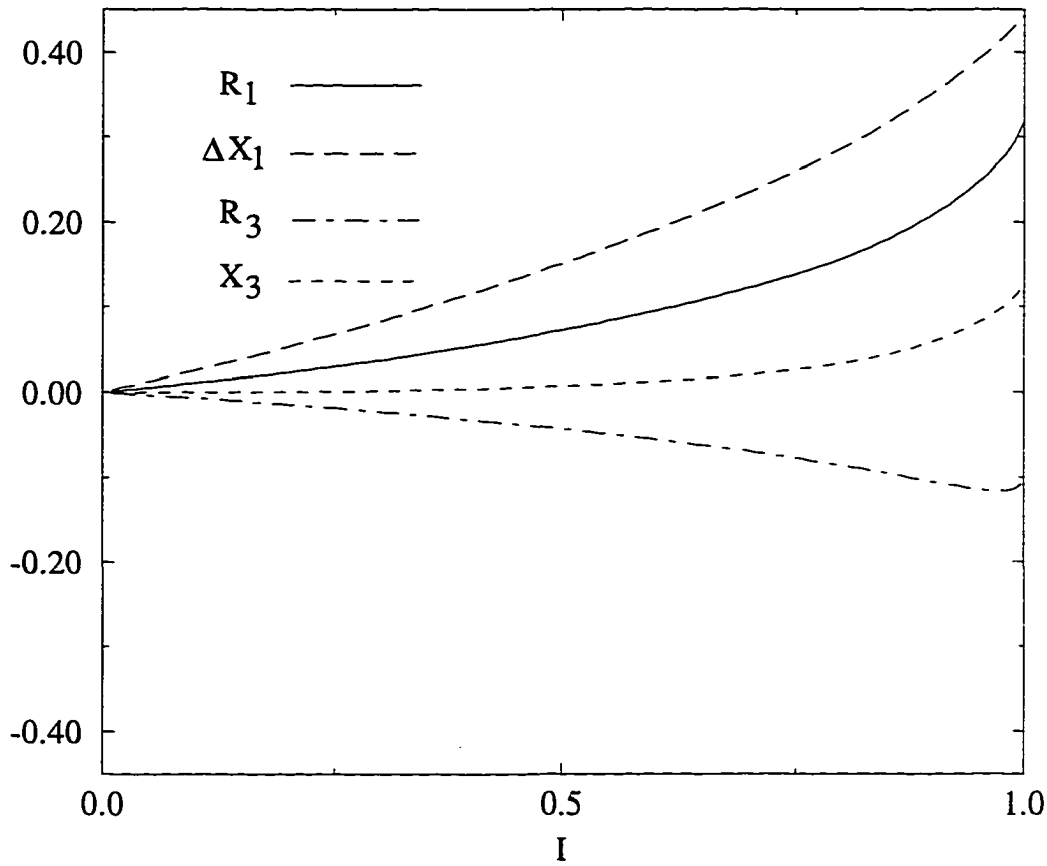

Figure 2.22 The resistance per unit length R_1, power-dependent part of the reactance per unit length ΔX_1, and third harmonics R_3 and X_3, in units of $\mu_0\omega_0/2\pi$, versus $I = I_{T0}/I_c$ for a superconducting elliptical wire transmission line.

frequencies $2\omega_1 - \omega_2$ and $2\omega_2 - \omega_1$, is given by the $n = N+3$ and $n = N-3$ terms of the series. The time-averaged dissipated power per unit length can be found by inserting Eq. (2.97) into Eq. (2.61),

$$P_{diss} = \frac{I_{T0}^2}{4}\left(R_{N+1} + R_{N-1}\right) . \tag{2.100}$$

Equation (2.100) implies that the resistance per unit length of the transmission line is equal to the average of R_{N+1} and R_{N-1}. The reactance per unit length is equal to the average of X_{N+1} and X_{N-1}.

The structure of the critical state in the presence of two frequencies is considerably more complicated than for a single frequency. The simpleist case is when the center conductor is a circular wire [$\alpha = 1$]. The flux fronts will be circular and there will only be one front moving at any given time. Let $a_1(t)$ be the radius of this front. The voltage drop per unit length is given by

$$V(t) = \frac{d}{dt}\left[\int_0^R d\rho B_\phi(\rho,t)\right] = \frac{da_1}{dt}\left[\int_0^R d\rho \frac{\partial}{\partial a_1} B_\phi(\rho,a_1)\right] . \tag{2.101}$$

where $B_\phi(\rho,t)$ is the magnetic flux density at radius ρ measured from the center of the wire. The expression for the magnitude of the partial derivative of B_ϕ is given by

$$\left|\frac{\partial}{\partial a_1} B_\phi(\rho,a_1)\right| = \begin{cases} 0, & \rho < a_1 , \\ 2\mu_0 J_c a_1/\rho , & a_1 < \rho , \end{cases} \tag{2.102}$$

and the sign is opposite to the sign of the current density in the region $a_1 < \rho < a$. The magnitude of $V(t)$ is given by

$$|V(t)| = -2\mu_0 J_c a_1 \frac{da_1}{dt} \ln\left(\frac{R}{a_1}\right) , \tag{2.103}$$

and the sign of $V(t)$ is the same as the sign of the current in the region $a_1 < \rho < a$. Therefore, once $a_1(t)$ is determined, $V(t)$ can be calculated with Eq. (2.103).

To determine $a_1(t)$ we must examine the equation

$$\frac{d}{dt} I_T(t) = 0 . \tag{2.104}$$

The roots of Eq. (2.104) are the values of t at which the previous flux front stops moving and the new flux front starts to penetrate in from the surface. Using Eq. (2.95) for $I_T(t)$ in Eq. (2.104) yields a transcendental equation which can only be solved numerically. However, when $N \gg 1$ the roots deviate only very slightly from integer multiples of π/ω_0. Using this approximation for the roots of Eq. (2.104) allows us to derive analytical exressions for $a_1(t)$. In order to derive the expressions we divide up the period $T = 2\pi/\Delta\omega$ into four equal intervals. Each of these intervals is then divided into $N/2$ equal subintervals. Each subinterval corresponds to a time period π/ω_0. At $t = 0$ the center conductor has

current-density and flux-density profiles given by

$$J_y(\rho) = \begin{cases} 0, & \rho < a_0, \\ J_c, & a_0 < \rho < a, \end{cases} \tag{2.105}$$

and

$$B_\phi(\rho) = \begin{cases} 0, & \rho < a_0, \\ \dfrac{\mu_0 J_c(\rho^2 - a_0^2)}{2\rho}, & a_0 < \rho < a, \\ \dfrac{\mu_0 J_c(r^2 - a_0^2)}{2\rho}, & a < \rho < R, \end{cases} \tag{2.106}$$

where $a_0 = \sqrt{1-I}$ and $I = I_{T0}/I_c$ with $I_c = \pi a^2 J_c$. A new front begins to penetrate in from the surface at $t = 0$ and collapses quasistatically toward the center until $t = \pi/\omega_0$, at which time it stops at radius $a_2 > a_0$. This new front leaves a current density $-J_c$ behind it as it penetrates in. At time $t = \pi/\omega_0$ another front begins to penetrate in and leaves a current density $+J_c$ behind it. This front stops at time $t = 2\pi/\omega_0$ and radius $a_3 > a_2$. This process continues until $t = (N/2-1)\pi/\omega_0$, at which time there is a remnant structure consisting of annular regions with the current density alternating between $+J_c$ and $-J_c$. The outermost annular region contains a current density $-J_c$. At time $t = (N/2-1)\pi/\omega_0$, a new front begins to penetrate into this remnant structure, leaving a current density $+J_c$ behind and it stops at time $t = (N/2+1)\pi/\omega_0$. At time $t = (N/2+1)\pi/\omega_0$ a front begins to penetrate in leaving a current density $-J_c$ and stops at time $t = (N/2+2)\pi/\omega_0$. This process continues until $t = N\pi/\omega_0$, at which time the current density is the same as as in Eq. (2.105) except with a negative sign. This corresponds to time $t = T/2 = \pi/\Delta\omega$. The same process occurs between $t = \pi/\Delta\omega$ and $t = 2\pi/\Delta\omega$, except that the positive and negative current densities are switched. The expression for $a_1(t)$ is derived by writing the expression for $I_T(t)$ in terms of $a_1(t)$ in each subinterval. The resulting expression for the first interval $0 \le t < \pi/2\Delta\omega$ is given by

$$a_1(t)/a = \sqrt{1 - \frac{I}{2}\left(\cos\left(\frac{m\pi}{N}\right) + (-1)^{m+1} I_T(t)/I_{T0}\right)}, \tag{2.107}$$

where m is the index that labels the subintervals, $m\pi \le \omega_0 t < (m+1)\pi$, $m = 0, 1, ..., N/2-1$. The expression for $I_T(t)$ is given by either Eq. (2.95) or Eq. (2.96). For $\pi/2\Delta\omega \le t < \pi/\Delta\omega$, the expressions are

$$a_1(t)/a = \begin{cases} \sqrt{1 - \frac{I}{2}\left(\sin\left(\frac{m\pi}{N}\right) + (-1)^m I_T(t)/I_{T0}\right)}, & (-1)^m I_T(t)/I_{T0} < \sin\left(\frac{m\pi}{N}\right), \\ \sqrt{1 - \frac{I}{2}\left(\sin\left(\frac{(m+1)\pi}{N}\right) + (-1)^m I_T(t)/I_{T0}\right)}, & \text{otherwise}, \end{cases} \tag{2.108}$$

$(N/2+m)\pi \le \omega_0 t < (N/2+m+1)\pi$, $m = 0, 1, ..., N/2-1$. The reason that there are two expressions for $\pi/2\Delta\omega \le t < \pi/\Delta\omega$ is that the flux fronts are penetrating through a remnant state. For $\pi/\Delta\omega \le$

$t < 3\pi/2\Delta\omega$,

$$a_1(t)/a = \sqrt{1 - \frac{I}{2}\left(\cos\left(\frac{m\pi}{N}\right) + (-1)^m I_T(t)/I_{T0}\right)}, \tag{2.109}$$

$(N+m)\pi \leq \omega_0 t < (N+m+1)\pi$, $m = 0, 1, ..., N/2-1$. For $3\pi/2\Delta\omega \leq t < 2\pi/\Delta\omega$,

$$a_1(t)/a = \begin{cases} \sqrt{1 - \frac{I}{2}\left(\sin\left(\frac{m\pi}{N}\right) + (-1)^{m+1} I_T(t)/I_{T0}\right)}, & (-1)^{m+1} I_T(t)/I_{T0} < \sin\left(\frac{m\pi}{N}\right), \\ \sqrt{1 - \frac{I}{2}\left(\sin\left(\frac{(m+1)\pi}{N}\right) + (-1)^{m+1} I_T(t)/I_{T0}\right)}, & \text{otherwise}, \end{cases} \tag{2.110}$$

$(3N/2+m)\pi \leq \omega_0 t < (3N/2+m+1)\pi$, $m = 0, 1, ..., N/2-1$. Using these expressions to calculate da_1/dt, I obtain

$$V(t) = -\frac{\mu_0 I_{T0}}{4\pi}\left(\omega_1 \sin(\omega_1 t) + \omega_2 \sin(\omega_2 t)\right)\left[\ln\left(\frac{R}{a}\right) - \ln\left(\frac{a_1(t)}{a}\right)\right]. \tag{2.111}$$

The first term within the brackets is a linear inductive response and is proportional to the geometric reactance per unit length X_0,

$$X_0 = \frac{\mu_0 \omega_0}{2\pi}\ln\left(\frac{R}{a}\right). \tag{2.112}$$

The second term arises from the hysteretic behavior and leads to nonlinearites.

When $0 < \alpha < 1$ a similar derivation can be performed and the same expressions are obtained for $a_1(t)$. The difference is that the voltage drop per unit length is now given by

$$V(t) = -\frac{\mu_0 I_{T0}}{4\pi}\left(\omega_1 \sin(\omega_1 t) + \omega_2 \sin(\omega_2 t)\right)\ln\left(\frac{R + \sqrt{R^2 - (1-\alpha^2)a_1(t)^2}}{(1+\alpha)a_1(t)}\right), \tag{2.113}$$

which can be expanded around large R to obtain

$$V(t) = -\frac{\mu_0 I_{T0}}{4\pi}\left(\omega_1 \sin(\omega_1 t) + \omega_2 \sin(\omega_2 t)\right)\left[\ln\left(\frac{2R}{(1+\alpha)a}\right) - \ln\left(\frac{a_1(t)}{a}\right) + O\left(\left(\frac{a}{R}\right)^2\right)\right]. \tag{2.114}$$

The first two term in Eq. (2.114) yield Eq. (2.111) when $\alpha = 1$. The third term is a small correction term that vanishes when $\alpha = 1$. The important observation is that the second term, which is the dominant nonlinear term, is independent of α. Figure 2.23 shows the resistance per unit length R_{N+1} and reactance per unit length ΔX_{N+1} $[\omega = \omega_1]$ as well as the third-order mixer products R_{N+3} and X_{N+3} $[\omega = 2\omega_1 - \omega_2]$ versus I for the elliptical geometry.

A similar analysis can be applied to the strip geometry. Let the position of the moving front be given by $a_1(t)$. The voltage drop per unit length is given by

$$V(t) = \frac{d}{dt}\left[-\int_0^R dx B_z(x,t)\right] = \frac{da_1}{dt}\left[-\int_0^R dx \frac{\partial}{\partial a_1} B_z(x, a_1)\right], \tag{2.115}$$

where B_z is the normal component of the magnetic field in the $x-y$ plane a distance x from the center of the strip. The magnitude of the partial derivative of B_z is given by

$$\left|\frac{\partial}{\partial a_1} B_z(x, a_1)\right| = \begin{cases} 0, & x < a_1, \\ B_f \dfrac{2a_1}{\sqrt{(W^2 - a_1^2)(x^2 - a_1^2)}}, & x > a_1, \end{cases} \tag{2.116}$$

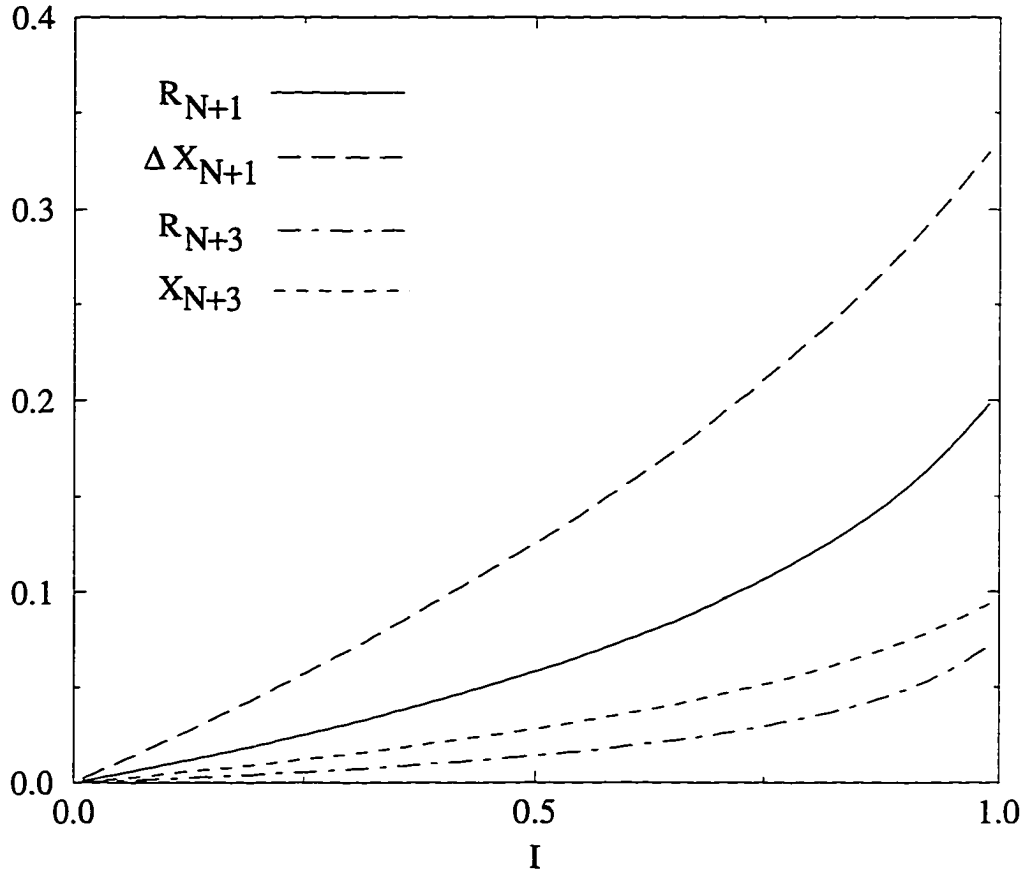

Figure 2.23 The resistance per unit length R_{N+1}, power-dependent part of the reactance per unit length ΔX_{N+1}, and third-order mixer products R_{N+3} and X_{N+3}, in units of $\mu_0\omega_0/2\pi$, versus $I = I_{T0}/I_c$ for a superconducting elliptical wire transmission line.

where the scaling field B_f is given by

$$B_f = \frac{\mu_0 J_c d}{\pi}, \tag{2.117}$$

and the sign is the same as the sign of the current density in the region $a_1 < x < W$. The magnitude of $V(t)$ is

$$|V(t)| = -2B_f a_1 \frac{da_1}{dt} \frac{1}{\sqrt{W^2 - a_1^2}} \ln\left(\frac{R + \sqrt{R^2 - a_1^2}}{a_1}\right), \tag{2.118}$$

and the sign is the same as the sign of the current density in the region $a_1 < x < W$.

The period is divided and subdivided in the same way as for the circular geometry. The expression for $a_1(t)$ during the first interval $0 \le t < \pi/2\Delta\omega$ is given by

$$a_1(t)/W = \sqrt{1 - \frac{I^2}{4}\left(\cos\left(\frac{m\pi}{N}\right) + (-1)^{m+1} I_T(t)/I_{T0}\right)^2}, \tag{2.119}$$

$m\pi \le \omega_0 t < (m+1)\pi$, $m = 0, 1, ..., N/2 - 1$. For $\pi/2\Delta\omega \le t < \pi/\Delta\omega$,

$$a_1(t)/W = \begin{cases} \sqrt{1 - \frac{I^2}{4}\left(\sin\left(\frac{m\pi}{N}\right) + (-1)^m I_T(t)/I_{T0}\right)^2}, & (-1)^m I_T(t)/I_{T0} < \sin\left(\frac{m\pi}{N}\right), \\ \sqrt{1 - \frac{I^2}{4}\left(\sin\left(\frac{(m+1)\pi}{N}\right) + (-1)^m I_T(t)/I_{T0}\right)^2}, & \text{otherwise}, \end{cases} \tag{2.120}$$

$(N/2 + m)\pi \le \omega_0 t < (N/2 + m + 1)\pi$, $m = 0, 1, ..., N/2 - 1$. For $\pi/\Delta\omega \le t < 3\pi/2\Delta\omega$,

$$a_1(t)/W = \sqrt{1 - \frac{I^2}{4}\left(\cos\left(\frac{m\pi}{N}\right) + (-1)^m I_T(t)/I_{T0}\right)^2}, \tag{2.121}$$

$(N + m)\pi \le \omega_0 t < (N + m + 1)\pi$, $m = 0, 1, ..., N/2 - 1$. For $3\pi/2\Delta\omega \le t < 2\pi/\Delta\omega$,

$$a_1(t)/W = \begin{cases} \sqrt{1 - \frac{I^2}{4}\left(\sin\left(\frac{m\pi}{N}\right) + (-1)^{m+1} I_T(t)/I_{T0}\right)^2}, & (-1)^{m+1} I_T(t)/I_{T0} < \sin\left(\frac{m\pi}{N}\right), \\ \sqrt{1 - \frac{I^2}{4}\left(\sin\left(\frac{(m+1)\pi}{N}\right) + (-1)^{m+1} I_T(t)/I_{T0}\right)^2}, & \text{otherwise}, \end{cases} \tag{2.122}$$

$(3N/2 + m)\pi \le \omega_0 t < (3N/2 + m + 1)\pi$, $m = 0, 1, ..., N/2 - 1$. Using these expressions to calculate da_1/dt, I obtain

$$V(t) = -\frac{\mu_0 I_{T0}}{4\pi}\left(\omega_1 \sin(\omega_1 t) + \omega_2 \sin(\omega_2 t)\right) \ln\left(\frac{R + \sqrt{R^2 - a_1^2}}{a_1}\right). \tag{2.123}$$

If I expand around large R, the result is

$$V(t) = -\frac{\mu_0 I_{T0}}{4\pi}\left(\omega_1 \sin(\omega_1 t) + \omega_2 \sin(\omega_2 t)\right)\left[\ln\left(\frac{2R}{W}\right) - \ln\left(\frac{a_1(t)}{W}\right) + O\left(\frac{W^2}{R^2}\right)\right]. \tag{2.124}$$

The first term is proportional to the geometric reactance per unit length

$$X_0 \simeq \frac{\mu_0 \omega_0}{2\pi} \ln\left(\frac{2R}{W}\right). \tag{2.125}$$

The second term arises from the hysteretic behavior and leads to nonlinearities. The third term leads to small corrections and will be neglected. Figure 2.24 shows the resistance per unit length R_{N+1} and reactance per unit length ΔX_{N+1} $[\omega = \omega_1]$ as well as the third-order mixer products R_{N+3} and X_{N+3} $[\omega = 2\omega_1 - \omega_2]$ versus I for the strip geometry.

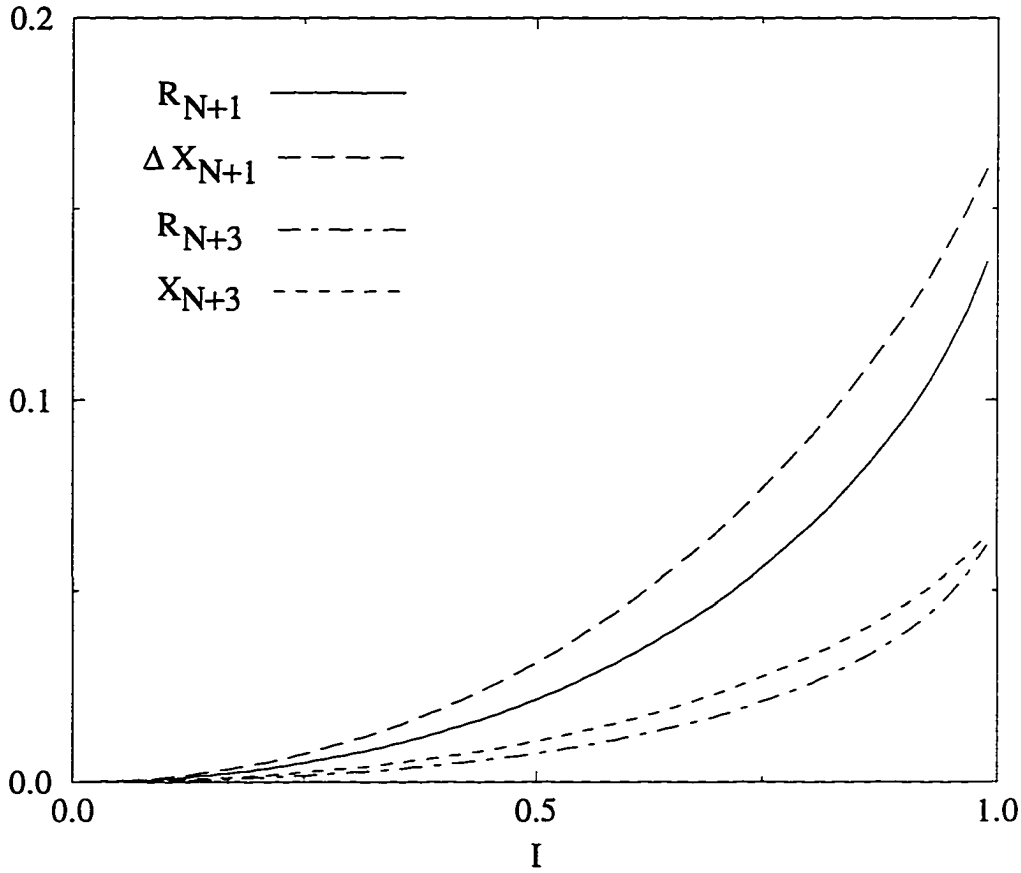

Figure 2.24 The resistance per unit length R_{N+1}, power-dependent part of the reactance per unit length ΔX_{N+1}, and third-order mixer products R_{N+3} and X_{N+3}, in units of $\mu_0\omega_0/2\pi$, versus $I = I_{T0}/I_c$ for a superconducting thin-film strip transmission line.

2.3.3 Applications to resonators

The results of Secs. 2.3.1 and 2.3.2 apply to infinitely long transmission lines. In experimental investigations and in device applications resonators or finite length segments of transmission lines are typically employed [Golosovsky et al., 1995, Nguyen et al., 1995, Oates et al., 1995, Wilker et al., 1995]. In order to apply the results of Secs. 2.3.1 and 2.3.2 to resonators it must be assumed that the fringing effects due to the ends of the resonator can be neglected. This should be an excellent approximation if the length of the resonator ℓ is much larger than the lateral dimension of the center conductor [$\ell \gg W, a$]. The expressions derived in Secs. 2.3.1 and 2.3.2 for $V(t)$, R_n, X_n, and P_{diss} must also be multiplied by ℓ to make them dimensionally correct. It can be shown that the relation between X_0 and the characteristic impedance Z_0 is $\ell X_0 = \pi Z_0$.

In a typical experiment a current given by $I_T = I_{T0}\cos(\omega_0 t)$ (HG) or $I_T = I_{T0}\cos(\omega_0 t)\cos(\Delta\omega t)$ (IM) is established in the center conductor. The output voltage signal is analyzed to determine the distribution of power among the various frequencies inside the resonator. The amount of output power at a given frequency can then be plotted versus the incident power to determine the degreee of nonlinearity in the resonator. The relation between the time-averaged output power P_{out} and the the time-averaged incident power P_{inc} is $P_{out} = r_v^2 P_{inc}$, where r_v is called the voltage insertion ratio. In the S parameter notation, $r_v = |S_{21}|$. The insertion loss IL is defined as IL $= -20\log_{10} r_v$ dB. In HG measurements a well-matched transmission-line sample is typically used and $P_{inc} \simeq (1/2) I_{T0}^2 \ell X_0$ [Shen, 1994]. The power spectrum at frequency $n\omega_0$ is proportional to $R_n^2 + X_n^2$, and the time-averaged output power at that frequency is

$$P_{out}(n\omega_0) = P_{out} \times \left(\frac{R_n^2 + X_n^2}{\sum_{n'=1}^{\infty} (R_{n'}^2 + X_{n'}^2)} \right) . \tag{2.126}$$

In IM measurements the resonator is usually weakly coupled to the input and output lines so that the loaded Q is nearly equal to the unloaded Q [Shen, 1994]. The relation between P_{inc} and I_{T0} has been derived previously [Oates et al., 1990]

$$I_{T0} = \sqrt{\frac{8 r_v (1 - r_v) Q P_{inc}}{\pi Z_0}} , \tag{2.127}$$

where $Q = X_{N+1}/R_{N+1}$ is the unloaded quality factor. The power spectrum at frequency $n\Delta\omega$ is proportional to $R_n^2 + X_n^2$, and the time-averaged output power at that frequency is

$$P_{out}(n\Delta\omega) = P_{out} \times \left(\frac{R_n^2 + X_n^2}{\sum_{n'=1}^{\infty} (R_{n'}^2 + X_{n'}^2)} \right) . \tag{2.128}$$

Figure 2.25 shows plots of $P_{out}(\omega_0)$ and $P_{out}(3\omega_0)$ versus P_{inc} for HG in both the elliptical and strip geometries. The slope of $P_{out}(\omega_0)$ versus P_{inc} curve is equal to one for both geometries. The slope of

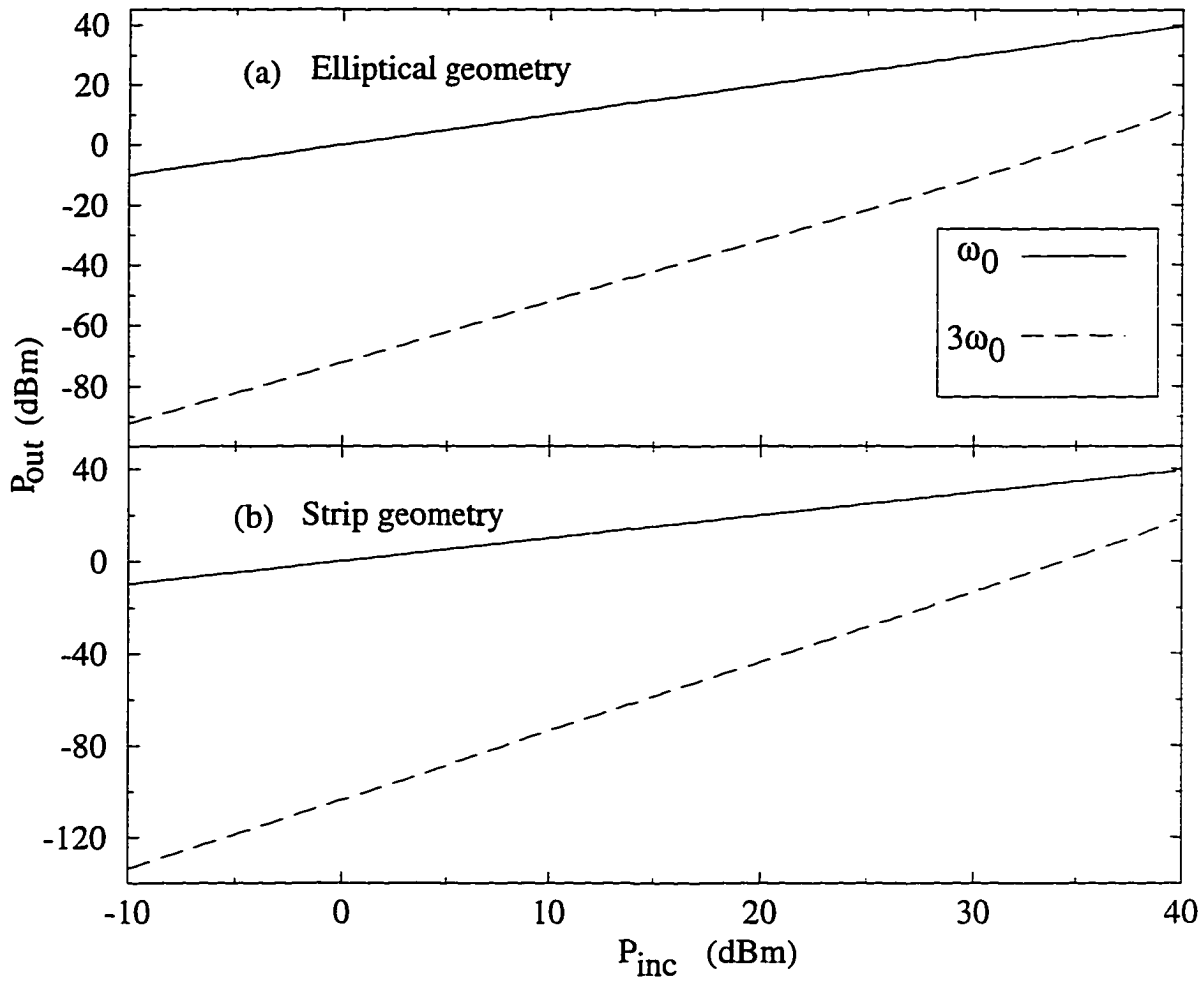

Figure 2.25 $P_{out}(\omega_0)$ and $P_{out}(3\omega_0)$ versus P_{inc} for a resonator, with either an elliptical (a) or strip (b) center conductor. All powers are expressed in dBm [P(dBm) = $10\log_{10}(P(\text{mW})/(1\text{ mW}))$]. The parameter values used were $Z_0 = 50\,\Omega$, $f_0 = \omega_0/2\pi = 1.6$ GHz, $\ell = 3$ cm, W or $a = 75\,\mu$m, d or $2b = 0.3\,\mu$m, and $J_c = 10^6$ A/cm^2. It was assumed that the dielectric constant characterizing the region between the conductors is $\epsilon = 10$.

the $P_{out}(3\omega_0)$ versus P_{inc} curve is equal to two in the elliptical geometry and equal to three in the strip geometry. The value of P_{inc} where $P_{out}(\omega_0)$ and $P_{out}(3\omega_0)$ become equal is denoted as $P_{inc}^{(\mathrm{TOI})}$. It can be shown that for the elliptical geometry

$$P_{inc}^{(\mathrm{TOI})} = \frac{1}{2}\left(\frac{5\pi I_c}{\mu_0(\omega_0/2\pi)\ell}\right)^2 (\pi Z_0)^3 , \tag{2.129}$$

and for the strip geometry

$$P_{inc}^{(\mathrm{TOI})} = \frac{(\pi I_c Z_0)^2/[\mu_0(\omega_0/2\pi)\ell]}{2\sqrt{(1/5\pi)^2+(1/32)^2}} . \tag{2.130}$$

The third order intercept (TOI) is defined as $10\log_{10}[P_{inc}^{(\mathrm{TOI})}/1\mathrm{mW}]$ dBm. Using the parameter values $Z_0 = 50\,\Omega$, $f_0 = \omega_0/2\pi = 1.6$ GHz, $\ell = 3$ cm, W or $a = 75\,\mu$m, d or $2b = 0.3\,\mu$m, and $J_c = 10^6$ A/cm^2. the TOI is equal to +72.2 dBm for the elliptical geometry and +57.7 dBm for the strip geometry.

The values of the TOI calculated from Eq. (2.126) are in reasonable agreement with experimental measurements on coplanar TBCCO lines given in Table II of [Wilker et al., 1995]. A better way to compare the theoretical predictions to the experimental results, however, is to examine how the TOI depends on line width, line length, and temperature, as was done in Table III of [Wilker et al., 1995]. According to Eq. (2.126), the change in the TOI when only the width of the line is changed from $2W_1$ to $2W_2$ is $\Delta\mathrm{TOI} = 20\log_{10}(W_2/W_1)$. When only the length of the line changes from ℓ_1 to ℓ_2, the corresponding TOI difference is $\Delta\mathrm{TOI} = 10\log_{10}(\ell_1/\ell_2)$, and when only the temperature changes is changed from T_1 to T_2, then $\Delta\mathrm{TOI} = 20\log_{10}(J_c(T_2)/J_c(T_1))$. Table 2.1 shows a comparison of experimental and theoretical values for ΔTOI. Excellent agreement is found with regard to the width dependence, and fair agreement is found with the dependencies on length and temperature.

Figure 2.26 shows plots of $P_{out}(\omega_1)$ and $P_{out}(2\omega_1-\omega_2)$ versus P_{inc} for IM both the elliptical and strip geometries. At low powers the slope of $P_{out}(\omega_1)$ versus P_{inc} is equal to one for both geometries and the slope of $P_{out}(2\omega_1-\omega_2)$ is equal to two for the elliptical geometry and three for the strip geometry. At intermediate powers the slope of $P_{out}(\omega_1)$ becomes equal to 1/2 for the elliptical geometry and 1/3 for the strip geometry, while the slope of $P_{out}(2\omega_1-\omega_2)$ is equal to one for both geometries. The change in slope between the low and high power regions is observed experimentally [Chin et al., 1992, Findikoglu, 1996]. Assuming the same parameter values as for the HG case yields a TOI of +29.0 dBm for the elliptical geometry and +18.0 dBm for the strip geometry.

The ratio $r = (\frac{\Delta\omega_0}{\omega_0})/\Delta(\frac{1}{2Q})$ has been stressed as an important figure of merit characterizing the nonlinearity in resonators. This quantity can be determined experimentally from the resonance curve. $\Delta\omega_0$ is the shift in position of the peak of the curve, and Q is the reciprocal of the bandwidth. This ratio is also related to the theoretical quantities R_1 and ΔX_1. The change in the bandwidth $\Delta(1/Q)$ is

Table 2.1 Comparison of the theoretical and experimental results for ΔTOI as the width, length, and temperature are varied independently. The experimental values were taken from [Wilker et al., 1995]. The values for the critical current density at a given temperature were determined by taking the average of all accurately reported values at that temperature.

Parameter	ΔTOI (dBm)	
	experiment	theory
Width		
($W \rightarrow 2W$)	6.2	6.0
($W \rightarrow 4W$)	12.2	12.0
($W \rightarrow 8W$)	18.4	18.1
Length		
(14 mm $\rightarrow$ 1 mm)	9.7	11.5
(14 mm $\rightarrow$ 5 mm)	3.1	4.5
(5 mm $\rightarrow$ 1 mm)	6.5	7.0
Temperature		
(100 K $\rightarrow$ 90 K)	15.6	12.3
(90 K $\rightarrow$ 80 K)	5.4	3.1
(80 K $\rightarrow$ 70 K)	5.5	5.8

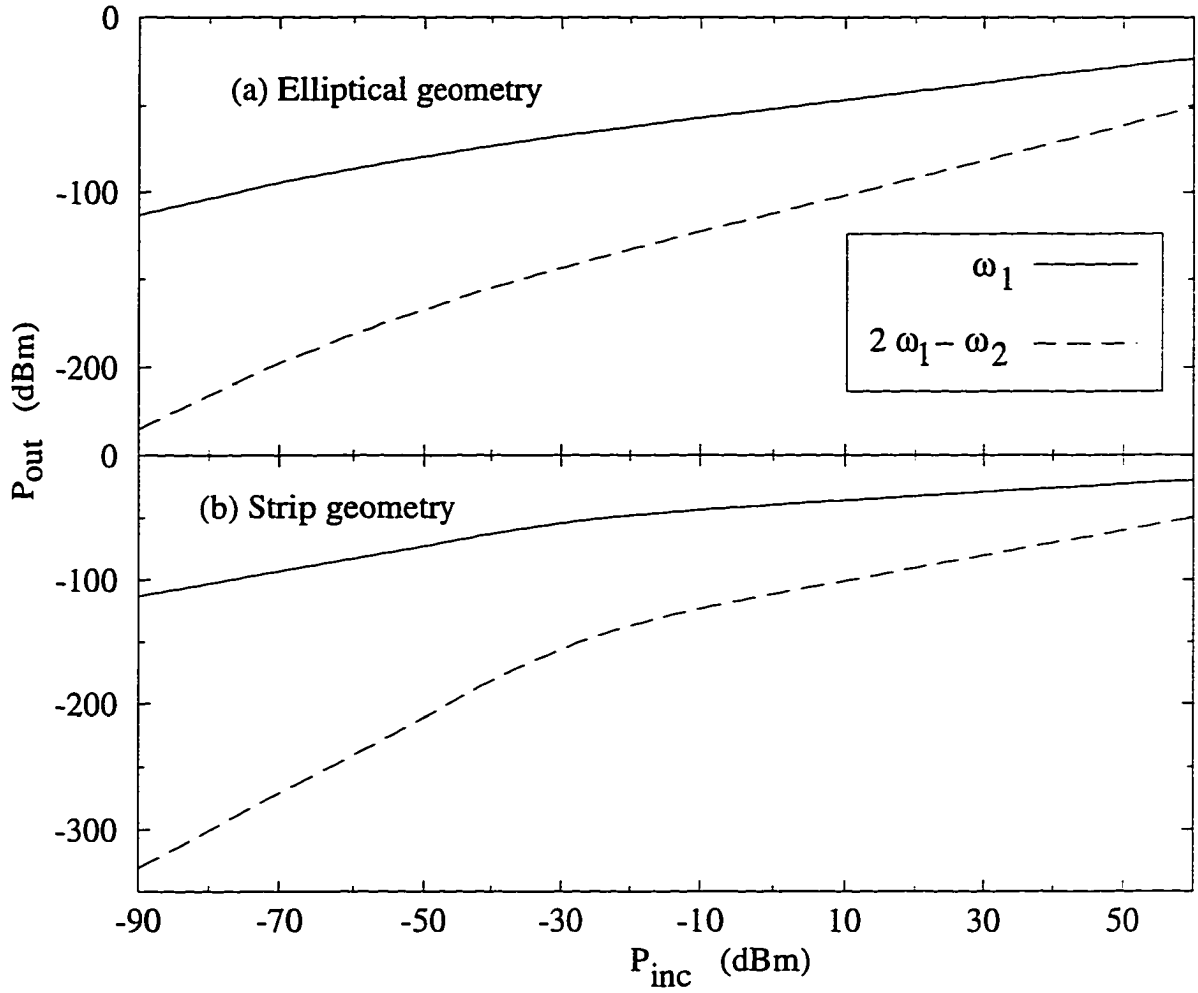

Figure 2.26 $P_{out}(\omega_1)$ and $P_{out}(2\omega_1 - \omega_2)$ versus P_{inc} for a resonator, with either an elliptical (a) or strip (b) center conductor. All powers are expressed in dBm [P(dBm) = $10\log_{10}(P(\text{mW})/(1\text{ mW}))$]. The parameter values used were $Z_0 = 50\,\Omega$, $f_0 = \omega_0/2\pi = 1.6$ GHz, $\ell = 3$cm, W or $a = 75\,\mu$m, d or $2b = 0.3\,\mu$m, and $J_c = 10^6$ A/cm^2. It was assumed that the dielectric constant characterizing the region between the conductors is $\epsilon = 10$.

given by

$$\Delta(\frac{1}{Q}) = \frac{R_1}{X_1}, \tag{2.131}$$

and the relative shift in resonant frequency $\Delta\omega_0/\omega_0$ is given by

$$\frac{\Delta\omega_0}{\omega_0} = \frac{1}{2}\frac{\Delta X_1}{X_1}. \tag{2.132}$$

Substituting these expressions into the expression for r yields

$$r = \frac{\Delta X_1}{R_1}. \tag{2.133}$$

Therefore, r provides a simple way to compare experiment and theory. In Nb microstrip resonators, the quantity r was found to be essentially constant (~ 1) except at temperatures close to T_c [Golosovsky et al., 1995]. In this case a plot of $\Delta\omega_0/\omega_0$ versus $\Delta(1/2Q)$ should be a straight line with slope of order unity at smaller values of I, and should deviate from a straight line at larger I values. Figure 2.27 shows such a plot using the derived expressions for R_1 and ΔX_1.

A frequency-independent r value of order unity is characteristic of the nonlinearity caused by vortex pinning and hysteresis. For other mechanisms the magnitude and frequency dependence of the r value may be quite different. For the case of the low-field behavior of weak links, the r value is often one or two orders of magnitude larger and is inversely proportional to the frequency. This has been observed in granular and polycrystalline samples in small fields [Halbritter, 1996].

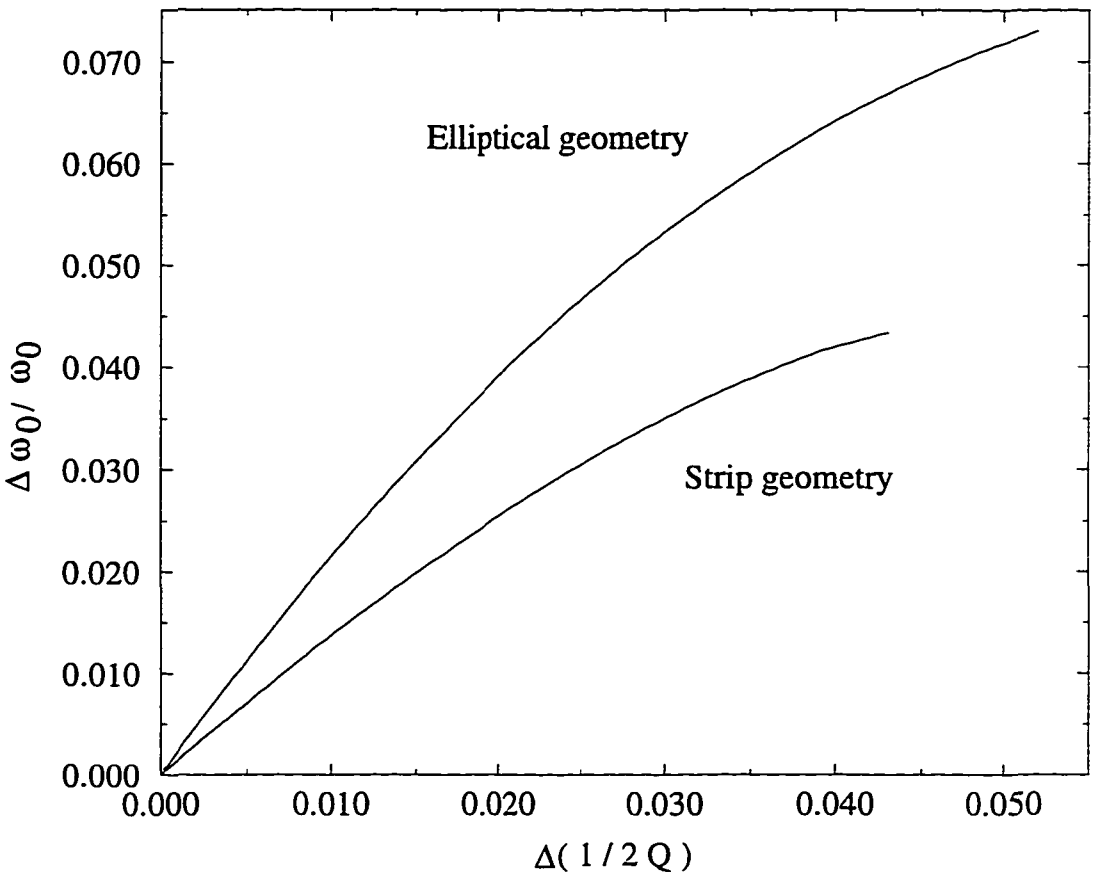

Figure 2.27 Plot of $\Delta\omega_0/\omega_0$ versus $\Delta(1/2Q)$ for a resonator with an elliptical or strip center conductor. The curves end at $I = 1$. The initial slopes of the lines, corresponding to $I \ll 1$, are 2.4 and 1.5 for the ellipse and strip, respectively. This straight-line behavior is observed experimentally [Golosovsky et al., 1995].

3 NONLINEARITIES IN SUPERCONDUCTING WEAK LINKS

3.1 Introduction

In this chapter I will consider the nonlinear effects caused by weak links in superconductors. In Sec. 3.2 I will examine HG in small Josephson junctions. In Sec. 3.3 HG in a long junction will be treated, and in Secs. 3.4 and 3.5 I will investigate the transition from small junction to large junction behaviour for both the slab and circular wire geometries.

3.2 Harmonic generation in small Josephson junctions

Penetration of magnetic flux into a Josephson junction occurs on a length scale characterized by a length λ_J called the Josephson penetration depth. A Josephson junction is small if all its dimensions transverse to the magnetic field are smaller than λ_J. The ac properties of a junction satisfying this criterion are most easily treated using the resistively and capacitively shunted junction (RCSJ) model [Tinkham, 1996, Van Duzer and Turner, 1981]. In this model the Josephson junction is modeled by an ideal junction J shunted by a resistance R and a capacitance C to form a parallel circuit (see Fig. 3.1). The current flowing through the circuit I_T can be thought of as the superposition of a supercurrent I_S, a normal current I_N, and a displacement current I_D. The normal current is caused by the flow of quasiparticles or single electron excitations across the barrier, while the displacement current is due to the time-varying electric field between the superconducting electrodes. The supercurrent, which flows through the ideal junction, is given by the Josephson relation,

$$I_S = I_0 \sin\Delta\gamma\,, \tag{3.1}$$

where I_{T0} is the critical current and $\Delta\gamma$ is the gauge-invariant phase difference across the junction which is related to $\Delta\phi$ by $\Delta\gamma = \Delta\phi - (2\pi/\phi_0)\int \mathbf{A}\cdot d\mathbf{s}$, where the integral is along a path connecting the two superconductors. The normal current and the displacement current are given by

$$I_N = \frac{V}{R}\,, \tag{3.2}$$

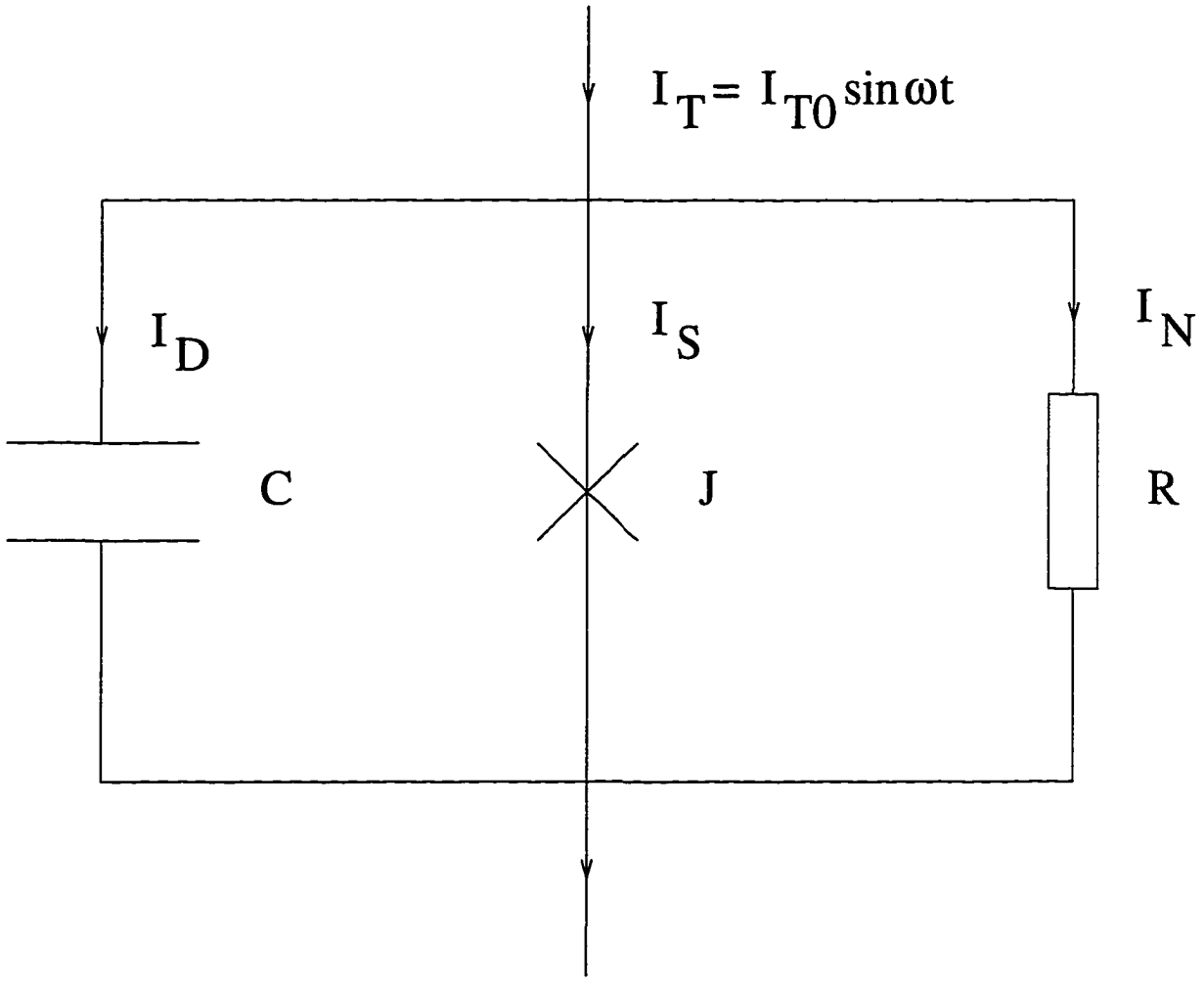

Figure 3.1 The circuit used to represent an actual Josephson junction in the RCSJ model. An ideal junction J is shunted by a resistance R and a capacitance C. The transport current I_T flowing through the junction is the sum of three terms: a supercurrent I_S through the ideal junction, a normal current I_N through the resistance, and a displacement current I_D through the capacitance.

and

$$I_D = C\frac{d}{dt}V\,, \tag{3.3}$$

where V is the voltage drop across the junction. The relation between V and $\Delta\gamma$ is

$$V(t) = \frac{\phi_0}{2\pi}\frac{d}{dt}\Delta\gamma(t)\,. \tag{3.4}$$

Combining Eqs. (3.1-3.4) yields

$$I_T = I_S + I_N + I_D = I_0 \sin\Delta\gamma(t) + \frac{\phi_0}{2\pi R}\frac{d}{dt}\Delta\gamma(t) + \frac{\phi_0 C}{2\pi}\frac{d^2}{dt^2}\Delta\gamma(t)\,. \tag{3.5}$$

For a given transport current we can determine $\Delta\gamma(t)$ by solving Eq. (3.5). In microwave applications I_T typically varies sinusoidally, $I_T = I_{T0}\sin(\omega t)$. In this case Eq. (3.5) becomes

$$\frac{1}{4\pi^2}\left(\frac{\omega}{\omega_p}\right)^2\frac{d^2}{dt'^2}\Delta\gamma(t') + \varepsilon\frac{d}{dt'}\Delta\gamma(t') + \sin\Delta\gamma(t') = I\sin(2\pi t')\,, \tag{3.6}$$

where $t' = t/T = \omega t/2\pi$, $\omega_p = \sqrt{1/L_J C}$, $\varepsilon = \omega L_J/2\pi R$, $L_J = \phi_0/2\pi I_0$, and $I = I_{T0}/I_0$. The frequency ω_p is the plasma frequency of the junction. For low driving frequencies, $\omega \ll \omega_p$, Eq. (3.6) reduces to

$$\varepsilon\frac{d}{dt'}\Delta\gamma(t') + \sin\Delta\gamma(t') = I\sin(2\pi t')\,. \tag{3.7}$$

The steady-state solution of Eq. (3.7) is periodic in the variable t', with a period equal to one. The voltage drop given by Eq. (3.3) will also be periodic with the same period. Therefore, we may expand V in a Fourier series,

$$V(t') = I_{T0}\sum_{n=1}^{\infty}\left[R_n\sin(2\pi n t') + X_n\cos(2\pi n t')\right]\,, \tag{3.8}$$

where the coefficients are given by

$$R_n = \frac{2}{I_{T0}}\int_0^1 V(t')\sin(2\pi n t')dt'\,, \tag{3.9}$$

and

$$X_n = \frac{2}{I_{T0}}\int_0^1 V(t')\cos(2\pi n t')dt'\,. \tag{3.10}$$

The coefficient R_1 is related to the time-averaged dissipated power P_{diss},

$$P_{diss} = \int_0^1 I_T(t')V(t')dt' = \frac{1}{2}I_{T0}^2 R_1\,. \tag{3.11}$$

Equation (3.11) indicates that R_1 is the resistance. The coefficient X_1 is the reactance. For $n > 1$ the coefficients are related to the generation of higher harmonics by the junction.

In the limit of small transport current, $I \ll 1$, $\Delta\gamma \ll 1$, and $\sin\Delta\gamma \simeq \Delta\gamma$. In this case Eq. (3.7) can be linearized,

$$\varepsilon\frac{d}{dt'}\Delta\gamma(t') + \Delta\gamma(t') = I\sin(2\pi t')\,. \tag{3.12}$$

The steady-state solution of Eq. (3.12) is

$$\Delta\gamma(t') = \frac{I}{1+4\pi^2\varepsilon^2}\left[-2\pi\varepsilon\cos(2\pi t') + \sin(2\pi t')\right], \tag{3.13}$$

and the resulting expression for $V(t')$ is

$$V(t') = I_{T0}R\frac{2\pi\varepsilon}{1+4\pi^2\varepsilon^2}\left[2\pi\varepsilon\sin(2\pi t') + \cos(2\pi t')\right]. \tag{3.14}$$

By comparing this with Eq. (3.8) one can see that

$$R_1 = \frac{4\pi^2\varepsilon^2}{1+4\pi^2\varepsilon^2}R \tag{3.15}$$

and

$$X_1 = \frac{2\pi\varepsilon}{1+4\pi^2\varepsilon^2}R. \tag{3.16}$$

These expressions are plotted as a function of ε in Fig. 3.2. There is a local maximum in X_1 at $\varepsilon = 1/2\pi$. At this value of ε the shunting resistance R is equal to the Josephson reactance ωL_J and $R_1 = X_1 = (1/2)R$.

In the opposite limit of large transport current, $I \gg 1$, $I_N \gg I_S$, and I_S can be neglected in Eq. (3.7),

$$\varepsilon\frac{d}{dt'}\Delta\gamma(t') = F\sin(2\pi t'). \tag{3.17}$$

The resulting $V(t')$ is

$$V(t') = I_{T0}R\sin(2\pi t'), \tag{3.18}$$

which implies $R_1 = R$ and $X_1 = 0$. This is also the solution when $\varepsilon \gg 1$.

In general, however, Eq. (3.7) must be solved numerically. This has been done previously by various authors [Auracher and Van Duzer, 1973, Herd et al., 1996, Perpeet et al. 1995, Xie et al., 1996, Zhai et al., 1996]. Figure 3.3(a) shows R_1 versus I for three different values of ε. When $\varepsilon \ll 1$, there are very sharp steps in R_1 for $I > 1$ (A and B, for example). Corresponding steps also are seen in X_1, R_3, and X_3 for small ε, as shown in Figs 3.3(b), 3.4(a), and 3.4(b), respectively. For R_1, the step heights decrease in magnitude with increasing I, and when $I \gg 1$, $R_1 \simeq R$, as expected. The sharp steps occur at values of I for which there are bifurcations in the solutions of Eq. (3.7). Figure 3.5(a) shows the first two bifurcations (marked A and B in Figs. 3.3 and 3.4) for $\varepsilon = 0.01$. These bifurcations cause sudden changes in the voltage drop $V(t)$ given in Eq. (3.4). As shown in Fig. 3.5(b), for $I = 1.064$ there is a negative voltage pulse near $t' = 0.4$ and a positive voltage pulse around $t' = 0.9$, while for $I = 1.065$ there is positive pulse near $t' = 0.4$ and a negative one near $t' = 0.9$. The voltage responses at $I = 1.198$ and $I = 1.199$ also differ from each other by a change in sign of voltage pulses in the neighborhood of

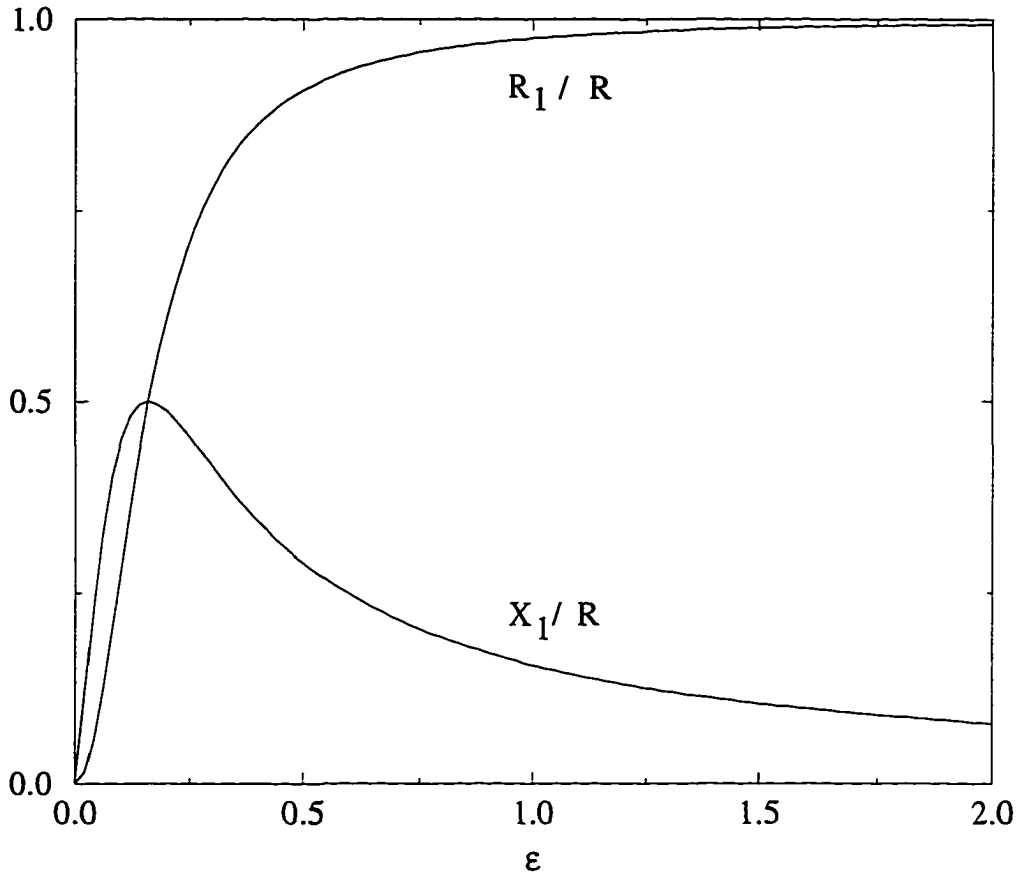

Figure 3.2 The resistance R_1 and reactance X_1 versus ε for the RSJ model when $I \ll 1$ [see Eqs. (3.15) and (3.16)]. R_1 increases from zero quadratically with increasing ε and quickly approaches the shunting resistance R. X_1 initially increases linearly with increasing ε, goes through a maximum at $\varepsilon = 1/2\pi$, and then decreases to zero as $1/\varepsilon$ as $\varepsilon \to \infty$. When $\varepsilon = 1/2\pi$ the shunting resistance is equal to the Josephson reactance ($R = \omega L_J = \phi_0\omega/2\pi I_0$), and $R_1 = X_1 = R/2$.

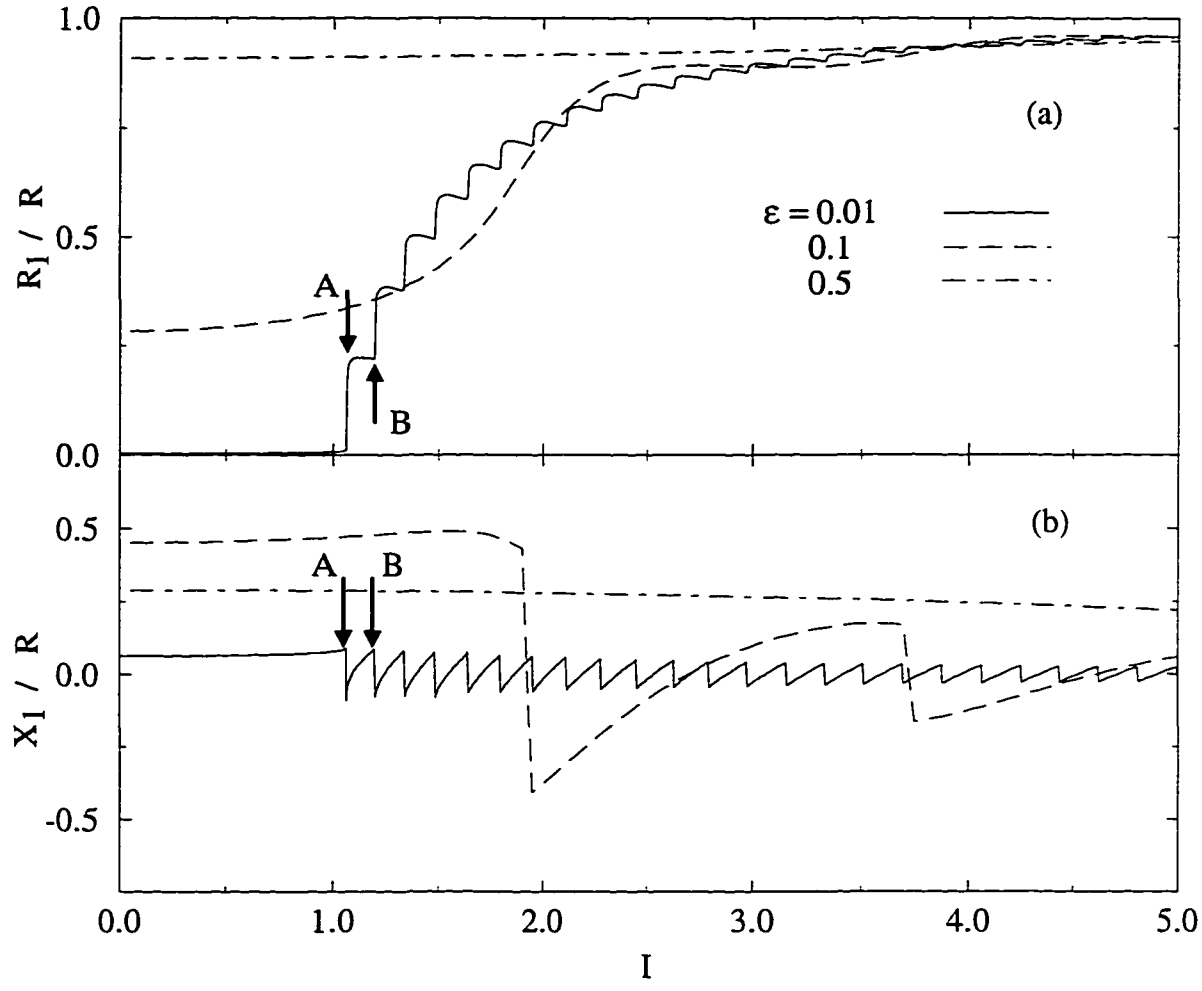

Figure 3.3 The resistance R_1 (top) and reactance X_1 (bottom) versus I in the RSJ model for three different values of ε. When ε is small, there are very sharp jumps. These jumps occur because of bifurcations in the gauge-invariant phase difference $\Delta\gamma$. Arrows indicate jumps at values of I for which bifurcations in $\Delta\gamma$ versus t are illustrated in Fig. 3.5(a). As ε increases, the bifurcations move to larger values of I, and successive bifurcations are spaced further apart. This causes the sharp steps to become broadened, to become less frequent, and eventually to disappear completely.

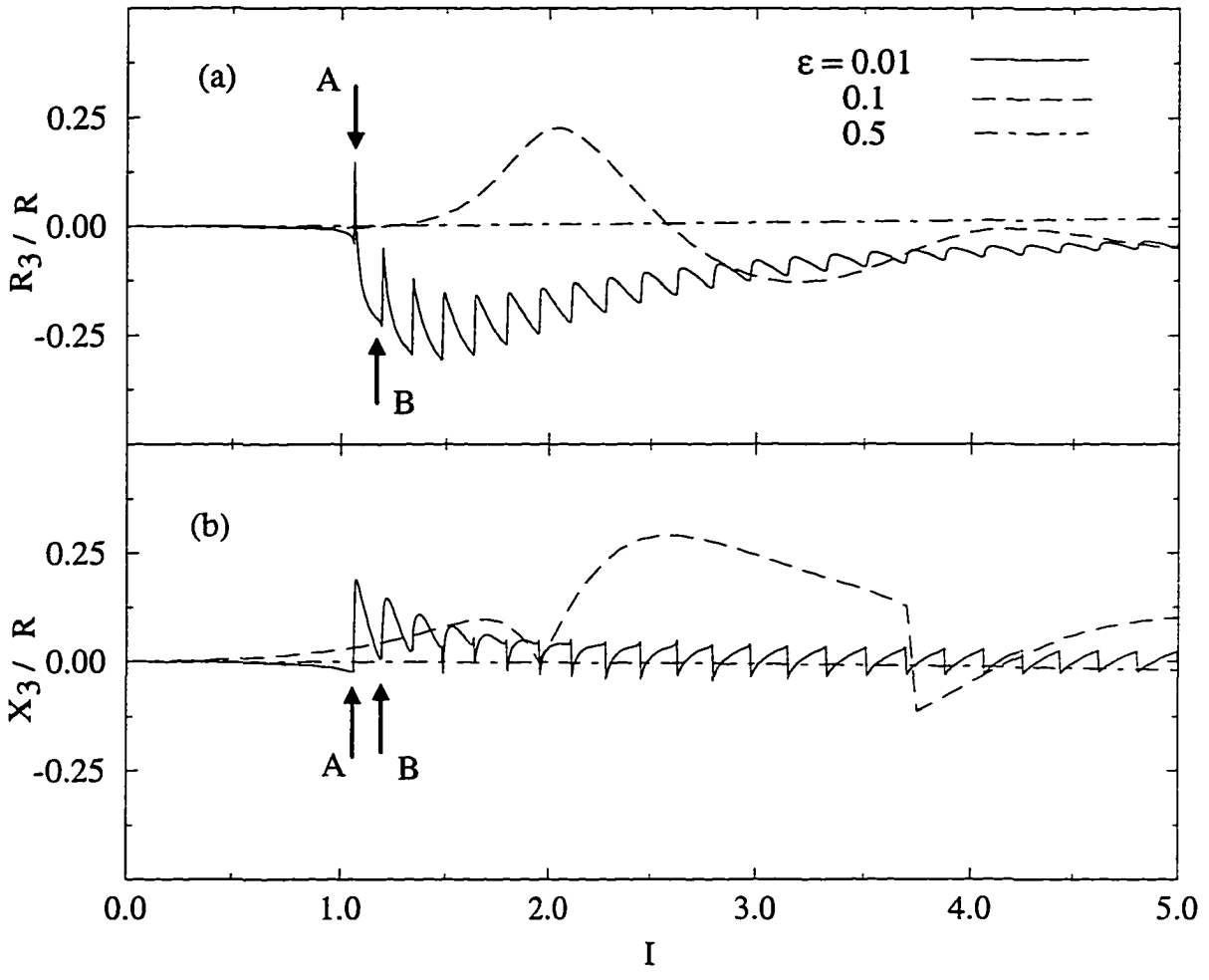

Figure 3.4 The third harmonic responses R_3 (top) and X_3 (bottom) versus I in the RSJ model for the same three values of ε as in Fig. 3.3. When ε is small, there are very sharp oscillations. These oscillations, which occur because of bifurcations in the gauge-invariant phase difference $\Delta\gamma$, have a behavior similar to the behavior described in the caption to Fig. 3.3. Arrows indicate steps at values of I for which the bifurcations are shown in Fig. 3.5(a).

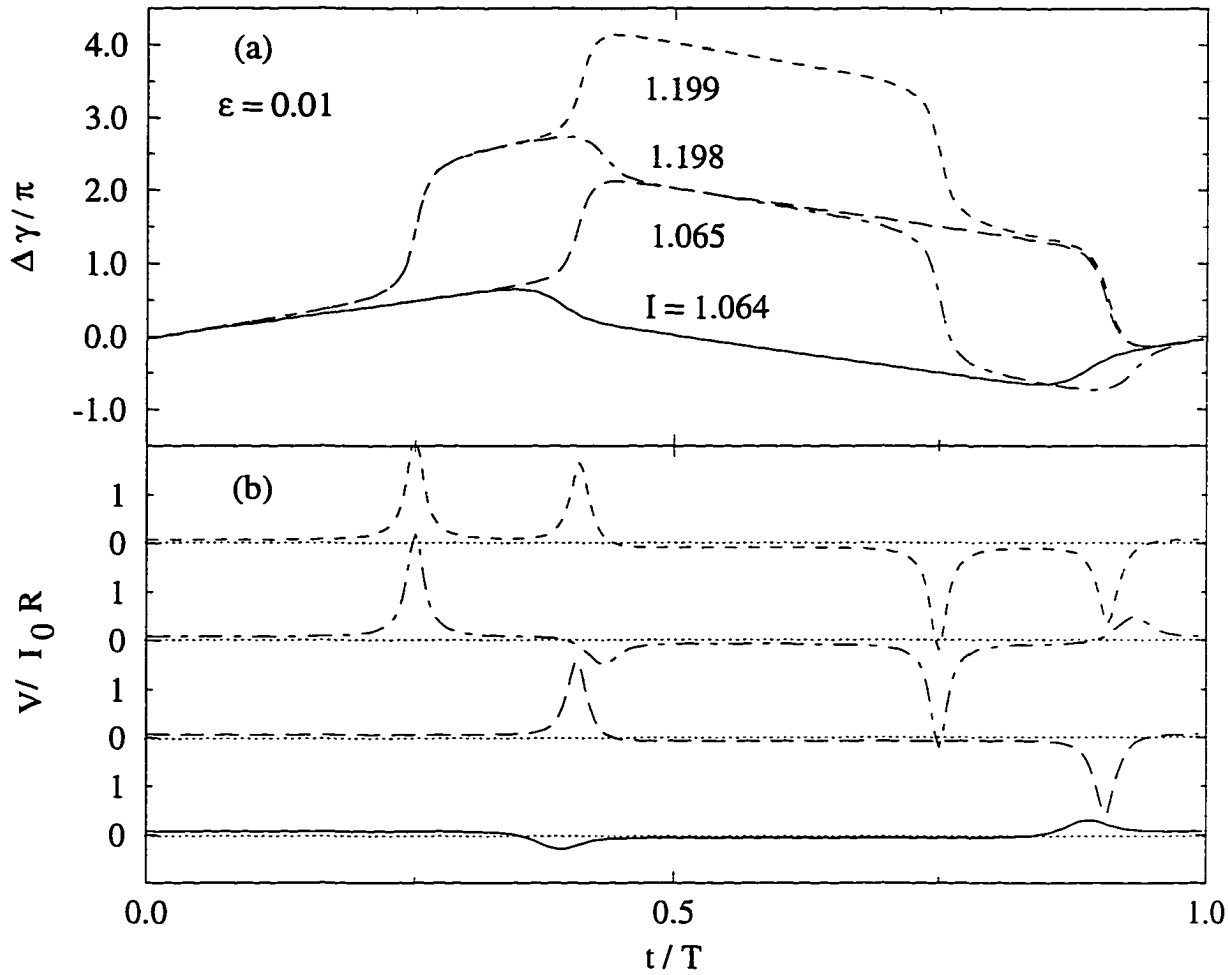

Figure 3.5 Plots of the gauge-invariant phase difference $\Delta\gamma(t)$ (a) and voltage drop $V(t) = (\phi_0/2\pi)d\Delta\gamma(t)/dt$ (b) versus t, for $\varepsilon = 0.01$, showing the first two bifurcations. The first bifurcation occurs between $I = 1.064$ and $I = 1.065$, and the second between $I = 1.198$ and $I = 1.199$. The bifurcations occur because $\Delta\gamma$ slips by 2π. For clarity, the voltage curves are offset in the vertical direction.

$t' = 0.4$ and $t' = 0.9$. Therefore, the sharp features in the curves of R_1, X_1, R_3, and X_3 correspond to the inversion of a voltage pulse at two different times during one cycle of the alternating current. As ε is increased, the bifurcations in the solution move to larger values of I, and the spacing between them becomes larger. The steps in R_1 are therefore broadened [see Fig. 3.3(a)]. As $\varepsilon \to \infty$, all the bifurcations are pushed to infinitely large values of I, and $R_1 \to R$. The curves in Fig. 3.3(a) indicate that this transition is approached quite rapidly.

3.3 Harmonic generation by a long Josephson junction in a superconducting half space

A Josephson junction is long if one of its dimensions transverse to the magnetic field is much larger than λ_J. In this case the RCSJ model no longer gives an adequate description of the ac properties of the junction.

Consider a semi-infinite superconductor ($x > 0$) containing the junction pictured in Fig. 3.6. The entire region $x > 0$, except for a slab of thickness d_i centered on the $x - z$ plane, is occupied by a superconductor with London penetration depth λ. The slab consists of a nonsuperconducting material of resistivity ρ_i and permittivity ϵ. There is an applied field $\mathbf{B_a} = B_{a0}\sin(\omega t)\hat{z}$ in the region $x < 0$. The Josephson penetration depth for this junction is $\lambda_J = \sqrt{\phi_0/(2\pi\mu_0 J_0 d)}$, where the magnetic thickness d is given by $d = 2\lambda + d_i$ and J_0 is the critical current density of the junction. The relation between the gauge-invariant phase difference across the junction $\Delta\gamma(x,t)$ and the magnetic field along the junction $b_z(x,t)$ is given by [Tinkham, 1996]

$$b_z(x,t) = -\frac{\phi_0}{2\pi d}\frac{\partial}{\partial x}\Delta\gamma(x,t)\,. \tag{3.19}$$

The relation between $\Delta\gamma(x,t)$ and the electric field across the junction $e_y(x,t)$ is

$$e_y(x,t) = \frac{\phi_0}{2\pi d_i}\frac{\partial}{\partial t}\Delta\gamma(x,t)\,. \tag{3.20}$$

The current density across the junction $J_y(x,t)$ is given by

$$J_y(x,t) = J_0\sin\Delta\gamma(x,t) + \frac{e_y(x,t)}{\rho_i}\,. \tag{3.21}$$

The first term is the Josephson relation for the supercurrent density and the second term is the normal leakage current density. $J_y(x,t)$ is related to $b_z(x,t)$ and $e_y(x,t)$ by Ampere's law with a displacement current,

$$-\frac{\partial}{\partial x}b_z(x,t) = \mu_0 J_y(x,t) + \mu_0\epsilon\frac{\partial}{\partial t}e_y(x,t)\,. \tag{3.22}$$

By combining Eqs. (3.19-3.22), we obtain a single equation for $\Delta\gamma(x,t)$,

$$\frac{\partial^2}{\partial x'^2}\Delta\gamma(x',t') - \frac{1}{4\pi^2}\left(\frac{\omega}{\omega_p}\right)^2\frac{\partial^2}{\partial t'^2}\Delta\gamma(x',t') - \alpha\frac{\partial}{\partial t'}\Delta\gamma(x',t') = \sin\Delta\gamma(x',t')\,, \tag{3.23}$$

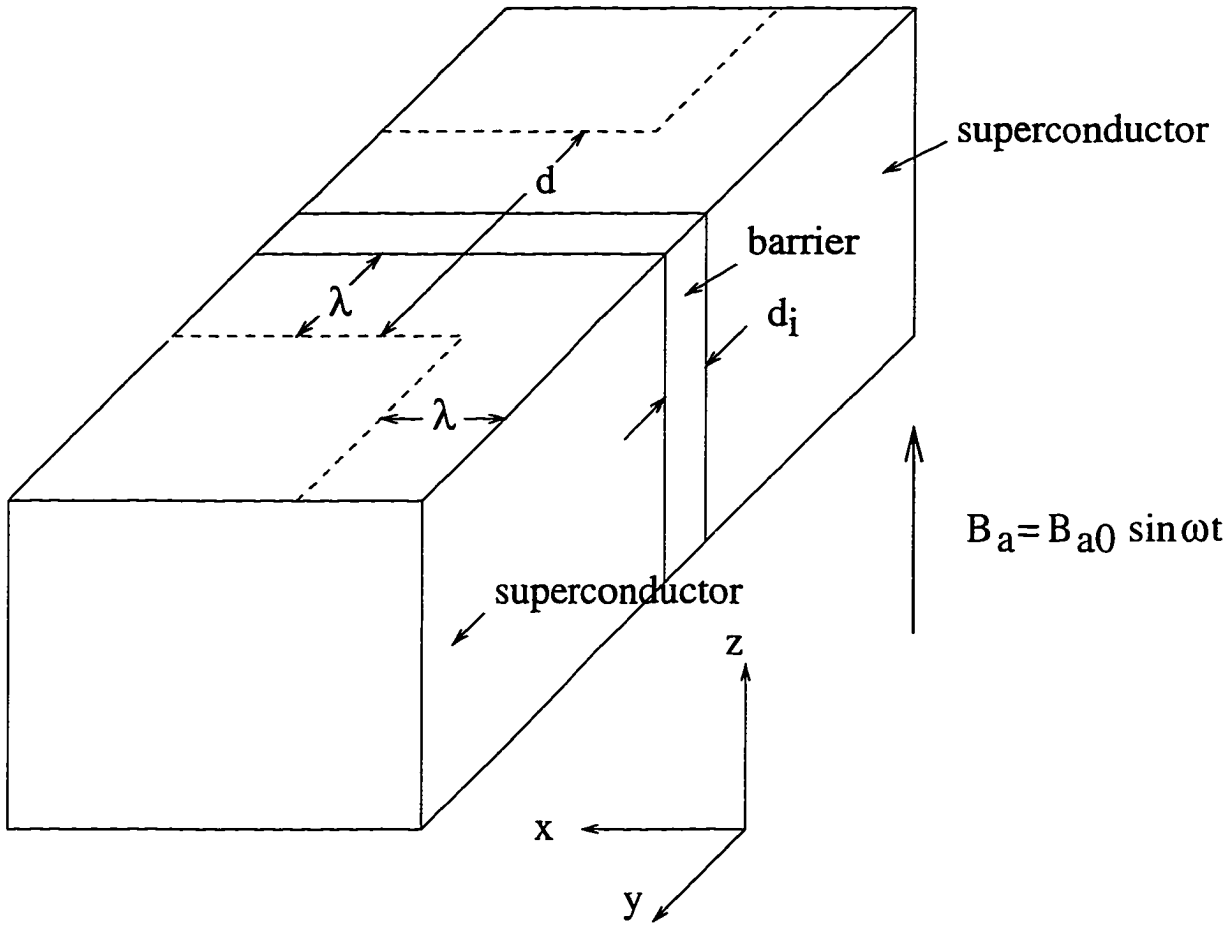

Figure 3.6 Geometry of a long Josephson junction. The region $x > 0$, excluding a slab of thickness d_i centered on the $x - z$ plane, is occupied by a superconductor with London penetration depth λ. The slab-shaped barrier region is characterized by a resistivity ρ_i. An ac magnetic field $\mathbf{B_a}$ is applied parallel to the z axis. A weak field will penetrate into the superconductor a distance λ from the surface $x = 0$. The length of penetration along the barrier region is given by $\lambda_J = \sqrt{\phi_0/2\pi\mu_0 J_0 d}$, where J_0 is the Josephson critical current density of the junction and $d = 2\lambda + d_i$ is the magnetic thickness of the junction.

where $x' = x/\lambda_J$, $t' = t/T = \omega t/2\pi$, $\omega_p = \sqrt{1/\mathcal{L}_J\mathcal{C}_J}$, $\alpha = \omega\mathcal{L}_J/2\pi\rho_i d_i$, $\mathcal{C}_J = \epsilon/d_i$, and $\mathcal{L}_J = \phi_0/2\pi J_0$. There is also a boundary condition at $x' = 0$

$$\left[\frac{\partial}{\partial x'}\Delta\gamma(x',t')\right]_{x'=0} = -2\pi F\sin(2\pi t')\,, \tag{3.24}$$

where $F = (B_{a0}\lambda_J d)/\phi_0$. The coefficient α is a damping parameter which arises because of the electrical connection between the superconductors. In the limit $\rho_i \to \infty$, $\alpha = 0$ and Eq. (3.23) reduces to the usual sine-Gordon equation [Tinkham, 1996]. The frequency ω_p is the plasma frequency of the junction and is usually in the infrared region of the spectrum ($\omega_p \simeq 10^{12}$ rad/s). For microwave applications $\omega \simeq 10^9$ rad/s so $\omega \ll \omega_p$; therefore, Eq. (3.23) reduces to

$$\frac{\partial^2}{\partial x'^2}\Delta\gamma(x',t') - \alpha\frac{\partial}{\partial t'}\Delta\gamma(x',t') = \sin\Delta\gamma(x',t')\,. \tag{3.25}$$

The steady-state solution for $\Delta\gamma(x',t')$ is periodic in t' with period unity. The electric field given by Eq. (3.20) is also periodic with the same period. Therefore, $e_y(x'=0,t')$ may be expanded in a Fourier series,

$$e_y(0,t') = H_{a0}\sum_{n=1}^{\infty}\left[R_n\sin(2\pi nt') + X_n\cos(2\pi nt')\right]\,, \tag{3.26}$$

where $H_{a0} = B_{a0}/\mu_0$, and the coefficients are given by

$$R_n = \frac{2}{H_{a0}}\int_0^1 e_y(0,t')\sin(2\pi nt')dt' \tag{3.27}$$

and

$$X_n = \frac{2}{H_{a0}}\int_0^1 e_y(0,t')\cos(2\pi nt')dt'\,. \tag{3.28}$$

By the Poynting theorem, the power per unit height absorbed by the surface P'_{abs} is given by

$$P'_{abs} = \int_0^1 dt'\int_{-\infty}^{\infty} dy\,[\mathbf{E}\times\mathbf{H}]_{x'=0}\,. \tag{3.29}$$

The only non-zero contribution comes from the region $-d_i/2 < y < d_i/2$, where the electric field is given by Eq. (3.26). Inserting Eq. (3.26) into Eq. (3.29) yields

$$P'_{abs} = \frac{1}{2}d_i H_{a0}^2 R_1\,, \tag{3.30}$$

which implies that R_1 is proportional to the surface resistance R_s. If the length of the sample in the y direction is equal to L, or if there is an array of long junctions spaced along the y direction with periodicity length L, then $R_s = (d_i/L)R_1$. We ignore here the energy dissipated via quasiparticles (normal fluid) within λ of the surface of the superconductor. Similarly, the surface reactance X_s is given by $X_s = (d_i/L)X_1 + (1 - d_i/L)\mu_0\omega\lambda$. The second term in X_s is due to the electric fields that accelerate the screening currents near the surface of the superconductor.

In the limit of small applied field, $F \ll 1$, $\sin\Delta\gamma \simeq \Delta\gamma$, and Eq. (3.25) can be linearized,

$$\frac{\partial^2}{\partial x'^2}\Delta\gamma(x',t') - \alpha\frac{\partial}{\partial t'}\Delta\gamma(x',t') - \Delta\gamma(x',t') = 0\,, \tag{3.31}$$

with the boundary condition given by Eq. (3.24). The steady-state solution for $\Delta\gamma(x',t')$ is

$$\Delta\gamma(x',t') = -\frac{2\pi F}{a^2+b^2}\,e^{-ax'}\left[a\sin(bx'-2\pi t') + b\cos(bx'-2\pi t')\right]\,, \tag{3.32}$$

where

$$a = (1+4\pi^2\alpha^2)^{1/4}\cos\left(\frac{1}{2}\tan^{-1}(2\pi\alpha)\right) \tag{3.33}$$

and

$$b = (1+4\pi^2\alpha^2)^{1/4}\sin\left(\frac{1}{2}\tan^{-1}(2\pi\alpha)\right)\,. \tag{3.34}$$

The electric field at the surface is given by

$$e_y(0,t') = H_{a0}\frac{\rho_i}{\lambda_J}\frac{2\pi\alpha}{a^2+b^2}\left[a\cos(2\pi t') + b\sin(2\pi t')\right]\,, \tag{3.35}$$

so that

$$R_1 = \frac{\rho_i}{\lambda_J}\frac{2\pi\alpha b}{a^2+b^2} = \frac{\rho_i}{\lambda_J}\frac{2\pi\alpha}{(1+4\pi^2\alpha^2)^{1/4}}\sin\left(\frac{1}{2}\tan^{-1}(2\pi\alpha)\right) \tag{3.36}$$

and

$$X_1 = \frac{\rho_i}{\lambda_J}\frac{2\pi\alpha a}{a^2+b^2} = \frac{\rho_i}{\lambda_J}\frac{2\pi\alpha}{(1+4\pi^2\alpha^2)^{1/4}}\cos\left(\frac{1}{2}\tan^{-1}(2\pi\alpha)\right)\,. \tag{3.37}$$

Figure 3.7 shows R_1 and X_1 as functions of α.

In the opposite limit of large applied field, $F \gg 1$, $e_y(x',t')/\rho_i \gg J_0\sin\Delta\gamma(x',t')$, and Eq. (3.25) becomes

$$\frac{\partial^2}{\partial x'^2}\Delta\gamma(x',t') = \alpha\frac{\partial}{\partial t'}\Delta\gamma(x',t')\,, \tag{3.38}$$

with the boundary condition given by Eq. (3.24). The solution for $\Delta\gamma(x',t')$ is

$$\Delta\gamma(x',t') = -F\sqrt{\frac{\pi}{\alpha}}\,e^{-\sqrt{\pi\alpha}\,x'}\left[\sin(\sqrt{\pi\alpha}\,x' - 2\pi t') + \cos(\sqrt{\pi\alpha}\,x' - 2\pi t')\right]\,, \tag{3.39}$$

which gives

$$e_y(0,t') = H_{a0}\frac{\rho_i}{\lambda_J}\sqrt{\pi\alpha}\,e^{-\sqrt{\pi\alpha}\,x'}\left[\cos(2\pi t') + \sin(2\pi t')\right] \tag{3.40}$$

and

$$R_1 = X_1 = \frac{\rho_i}{\delta_J}\,, \tag{3.41}$$

where we have defined the Josephson skin depth $\delta_J = \lambda_J/\sqrt{\pi\alpha} = (2\rho_i d_i/\mu_0 d\omega)^{1/2}$. This is also the result for the limit of large damping, $\alpha \gg 1$. Thus, at high fields or large damping the junction behaves

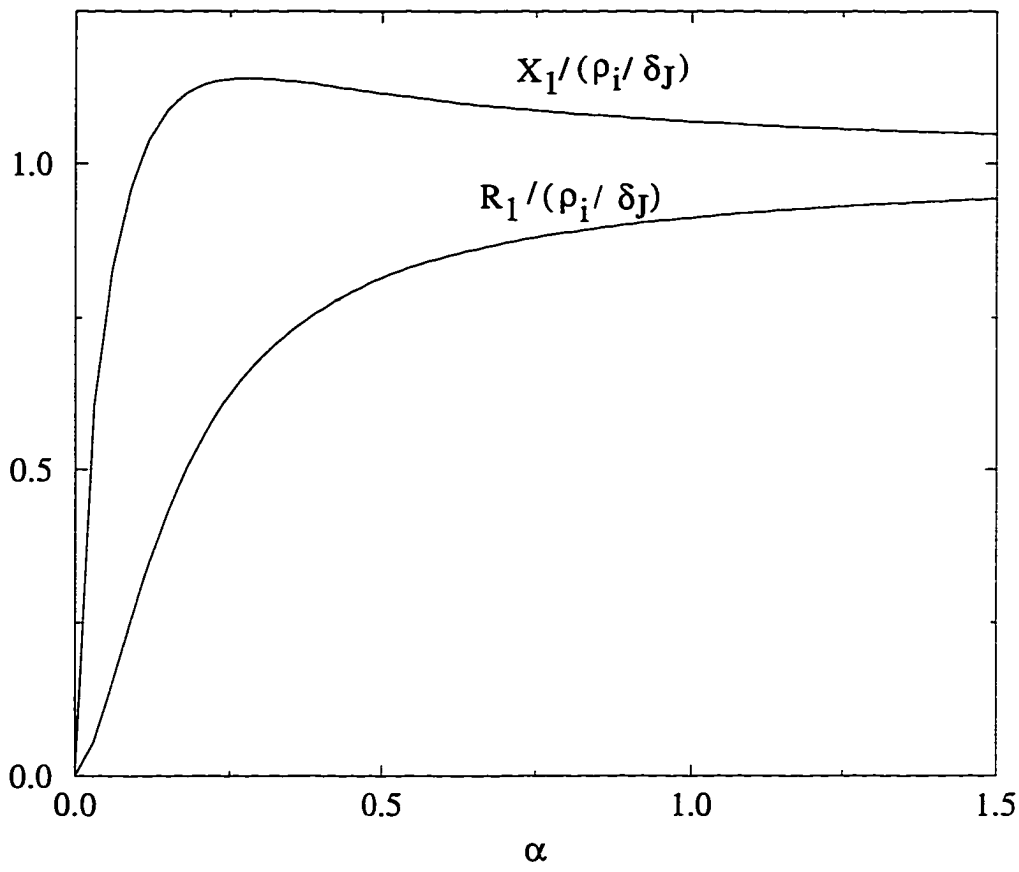

Figure 3.7 Resistance R_1 and reactance X_1 of a long uniform junction versus damping parameter α for $F \ll 1$. R_1 increases from zero with increasing α and quickly approaches the limiting value ρ_i/δ_J. X_1 initially increases with increasing α up to a value larger than the limiting value ρ_i/δ_J, then slowly approaches the limiting value from above as $\alpha \to \infty$.

like a normal metal with resistivity ρ_i and skin depth δ_J. The reason for this is that in these two limits the magnitude of the normal current is much larger than the magnitude of the supercurrent, and the normal current, therefore, dominates the behavior of the junction.

In general Eq. (3.25) must be solved numerically. Figure 3.8(a) shows R_1 versus F for three different values of α. For the smallest value of α, there are sharp jumps in R_1 (C, D, and E, for example) which decrease in amplitude as F increases. For $F \gtrsim 1$, R_1 quickly approaches the saturation value ρ_i/δ_J. As α increases, the sharp steps become broader until they disappear completely and R_1 approaches ρ_i/δ_J for all values of F. From Fig. 3.8(a) it is apparent that this limit is approached even for very modest values of α. The behaviors of X_1, R_3, and X_3 vs. F for the same values of α are shown in Figs. 3.8(b), 3.9(a), and 3.9(b), respectively.

The sharp jumps and fine features (C, D, E, F, and G) in Figs. 3.8 and 3.9 for $\alpha = 0.005$ are caused by changes in the number of Josephson vortices in the junction. The nucleation of a vortex at the first jump (C) in R_1 is depicted in Figs. 3.10 and 3.11. Several field profiles are shown as the field at the surface changes through one period. Just below the jump C shown in Figs. 3.8 and 3.9 ($F = 0.32$) the field decays from the surface (see Fig. 3.10) and there are no vortices visible. However, just above this jump ($F = 0.33$) (Fig. 3.11), there is clearly a vortex trapped in the junction during one half cycle and an antivortex trapped during the other half cycle. The nucleation process at the second jump (D in Figs. 3.8 and 3.9) is shown in Figs. 3.12 and 3.13. Just below the jump ($F = 0.41$) there is either a single vortex or a single antivortex inside the junction. Just above the jump ($F = 0.42$) there are two vortices trapped during one half cycle but only one antivortex trapped during the other half cycle. At the third jump (E in Figs. 3.8 and 3.9), the symmetry between the two half cycles is restored, so that there is a two-vortex two-antivortex state (Figs. 3.14 and 3.15). There is another shift to an asymmetric three-vortex two-antivortex state at the fourth jump (F in Figs. 3.8 and 3.9), and the symmetry is then restored to a three-vortex three-antivortex state at the fifth jump (G in Figs. 3.8 and 3.9). The asymmetry occurring between the second and third jumps (D and E in Figs. 3.8 and 3.9), and between the fourth and fifth jumps (F and G in Figs. 3.8 and 3.9), leads to the generation of second harmonics, as shown in Fig. 3.16. The sign of R_2 and X_2 depend on whether the jump is approached from below (increasing F) or above (decreasing F). This effect occurs because the direction that the symmetry is broken (more vortices than antivortices or vice versa) depends on the previous history of the junction.

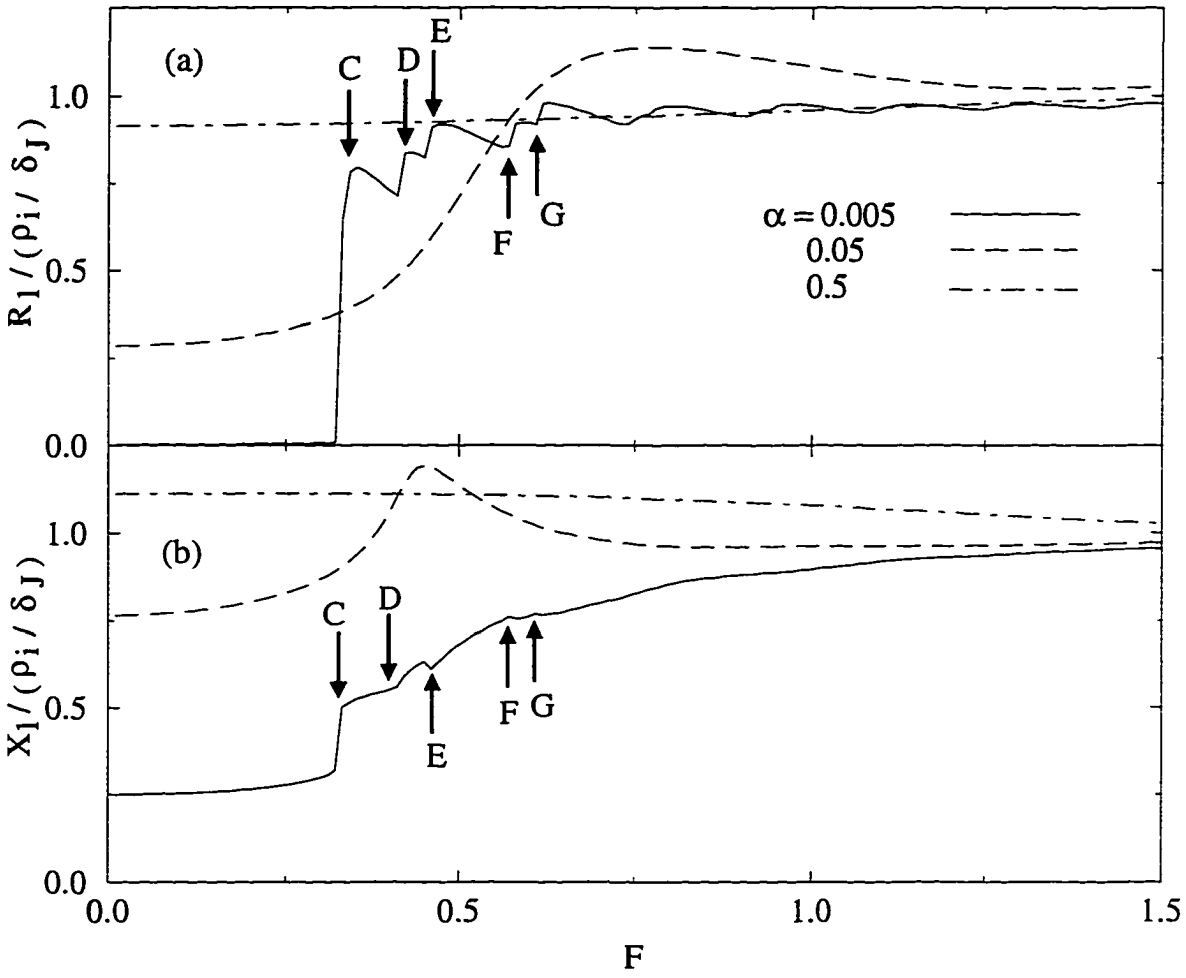

Figure 3.8 Resistance R_1 (a) and reactance X_1 (b) of a long, uniform junction versus F for three different values of α. When α is small, sharp features (C, D, E, F, and G) are visible. These features occur because of changes in the number of Josephson vortices in the barrier region. As the damping parameter α increases, the threshold for vortex nucleation is pushed to larger values of F and the vortex dynamics play a less significant role. This causes the sharp features to become broadened and eventually to disappear completely.

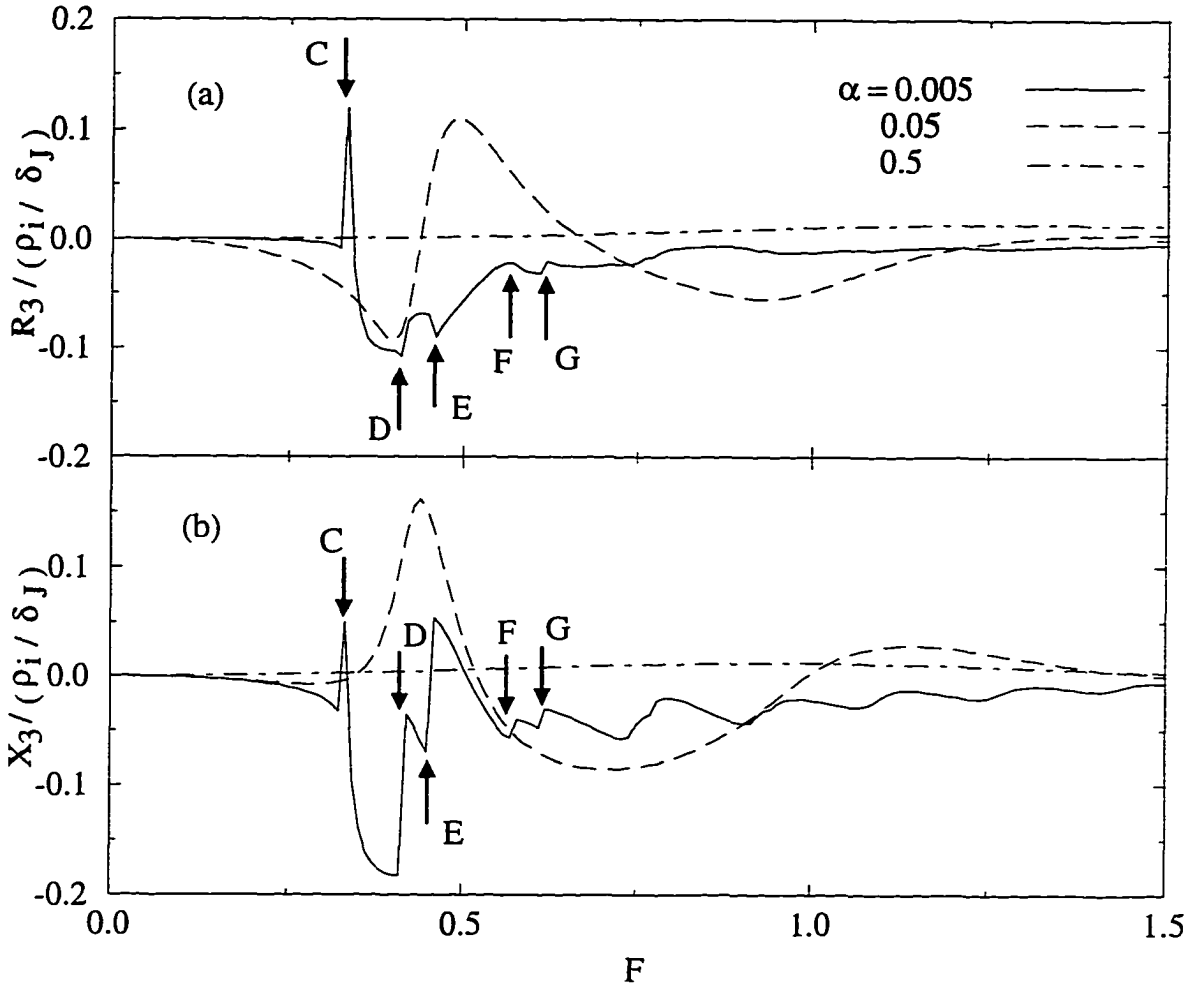

Figure 3.9 Third harmonics R_3 (a) and X_3 (b) versus F for a long, uniform junction for three different values of α. When α is small, there are some sharp features (C, D, E, F, and G) visible that are associated with the nucleation of Josephson vortices in the barrier region. As α increases, the threshold for vortex nucleation is pushed to larger values of F and the vortex dynamics play a less significant role in the electrodynamic properties of the junction. This causes the sharp features to become smoother and eventually to disappear completely.

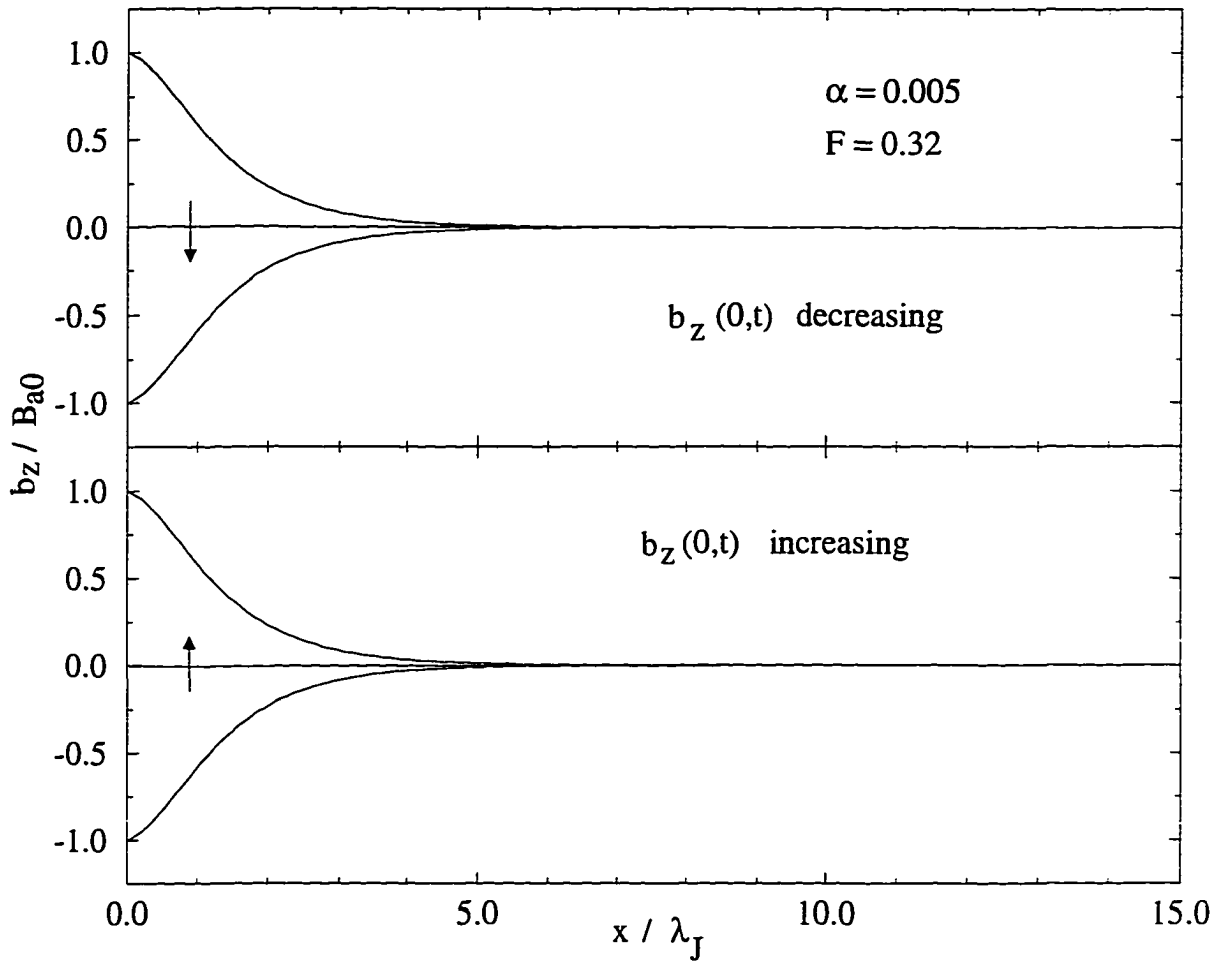

Figure 3.10 Profiles of $b_z(x,t)$ versus x for a long uniform junction with $\alpha = 0.005$ at $F = 0.32$, just before the first vortex nucleation process will occur. The top figure corresponds to the external ac field decreasing from $+B_{a0}$ to $-B_{a0}$, and the bottom figure corresponds to the external ac field increasing from $-B_{a0}$ to $+B_{a0}$. The external field is screened by the junction on a scale of a few λ_J.

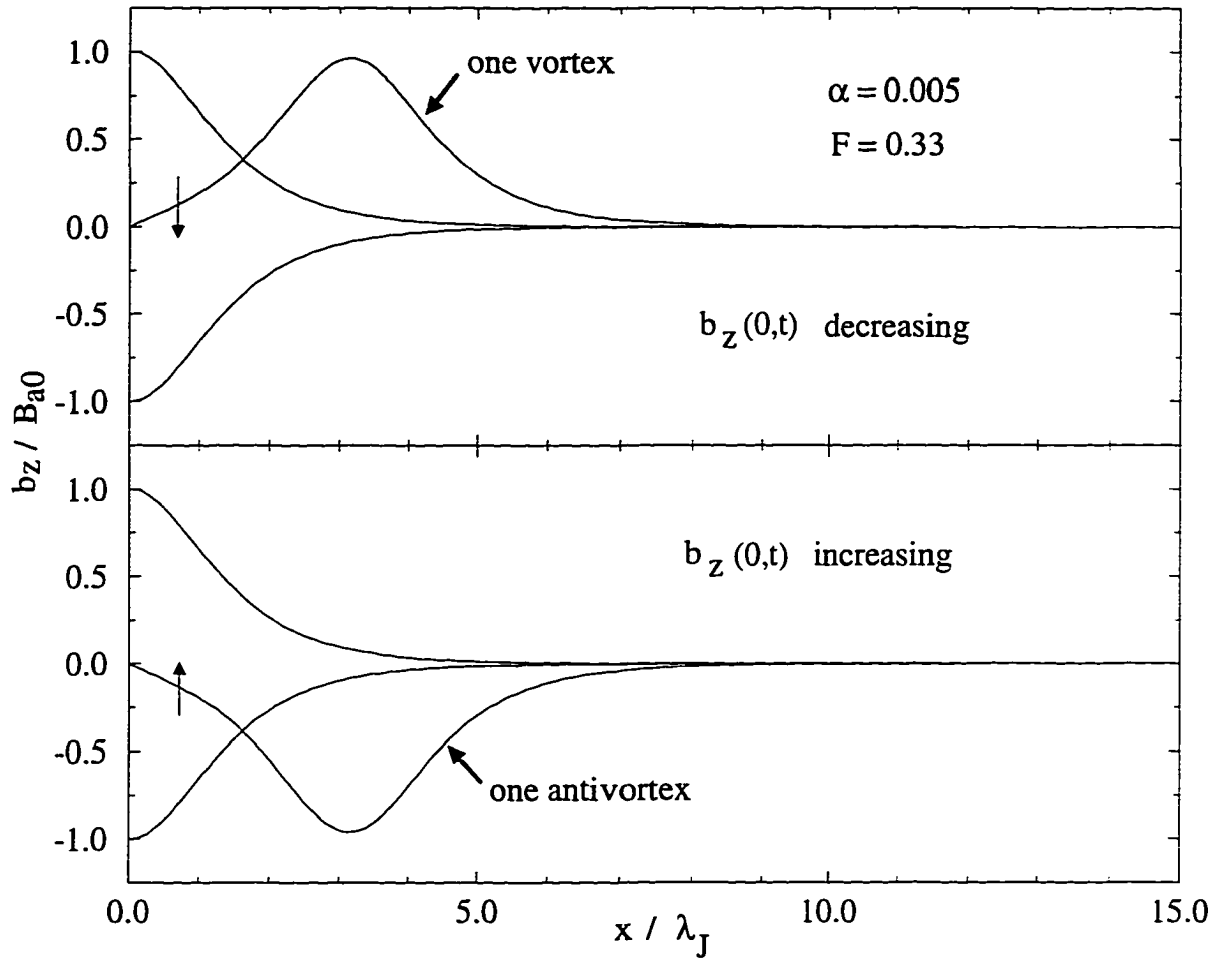

Figure 3.11 Profiles of $b_z(x,t)$ versus x for a long, uniform junction with $\alpha = 0.005$ at $F = 0.33$, just after the first vortex nucleation process (feature C in Figs. 3.8 and 3.9) has occurred. The top figure corresponds to the external ac field decreasing from $+B_{a0}$ to $-B_{a0}$. The bottom figure corresponds to the external ac field increasing from $-B_{a0}$ to $+B_{a0}$. When the external field is zero, there is clearly either a vortex (top figure) or an antivortex (bottom figure) trapped in the junction. The field increasing and field-decreasing profiles of $b_z(x)$ are mirror images of each other.

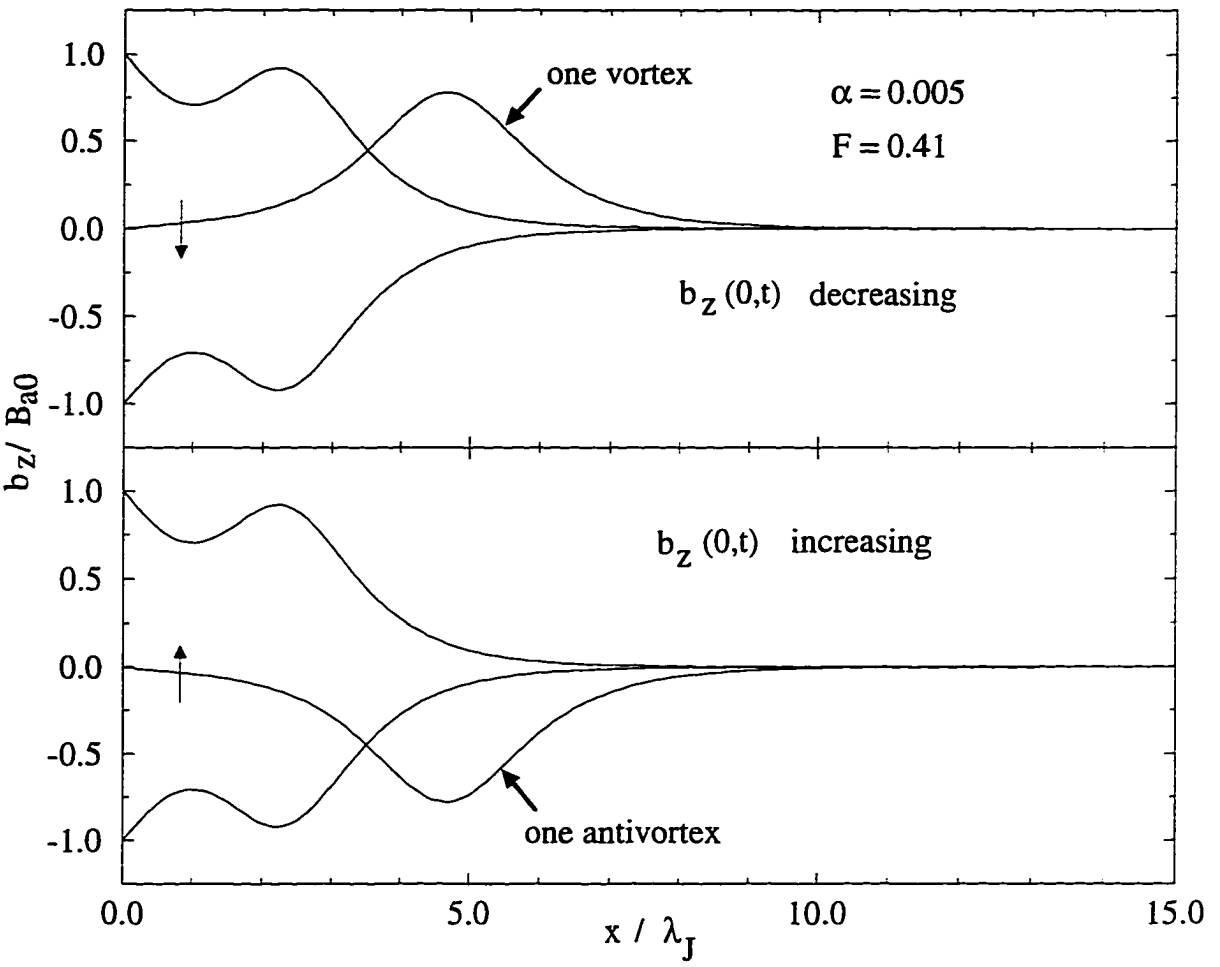

Figure 3.12 Profiles of $b_z(x,t)$ versus x for a long uniform junction with $\alpha = 0.005$ at $F = 0.41$, just before the second vortex nucleation process (feature D in Figs. 3.8 and 3.9) will occur. The top figure corresponds to the external ac field decreasing from $+B_{a0}$ to $-B_{a0}$. The bottom figure corresponds to the external ac field increasing from $-B_{a0}$ to $+B_{a0}$. When the external field is zero there is clearly either a vortex (top figure) or an antivortex (bottom figure) trapped in the junction.

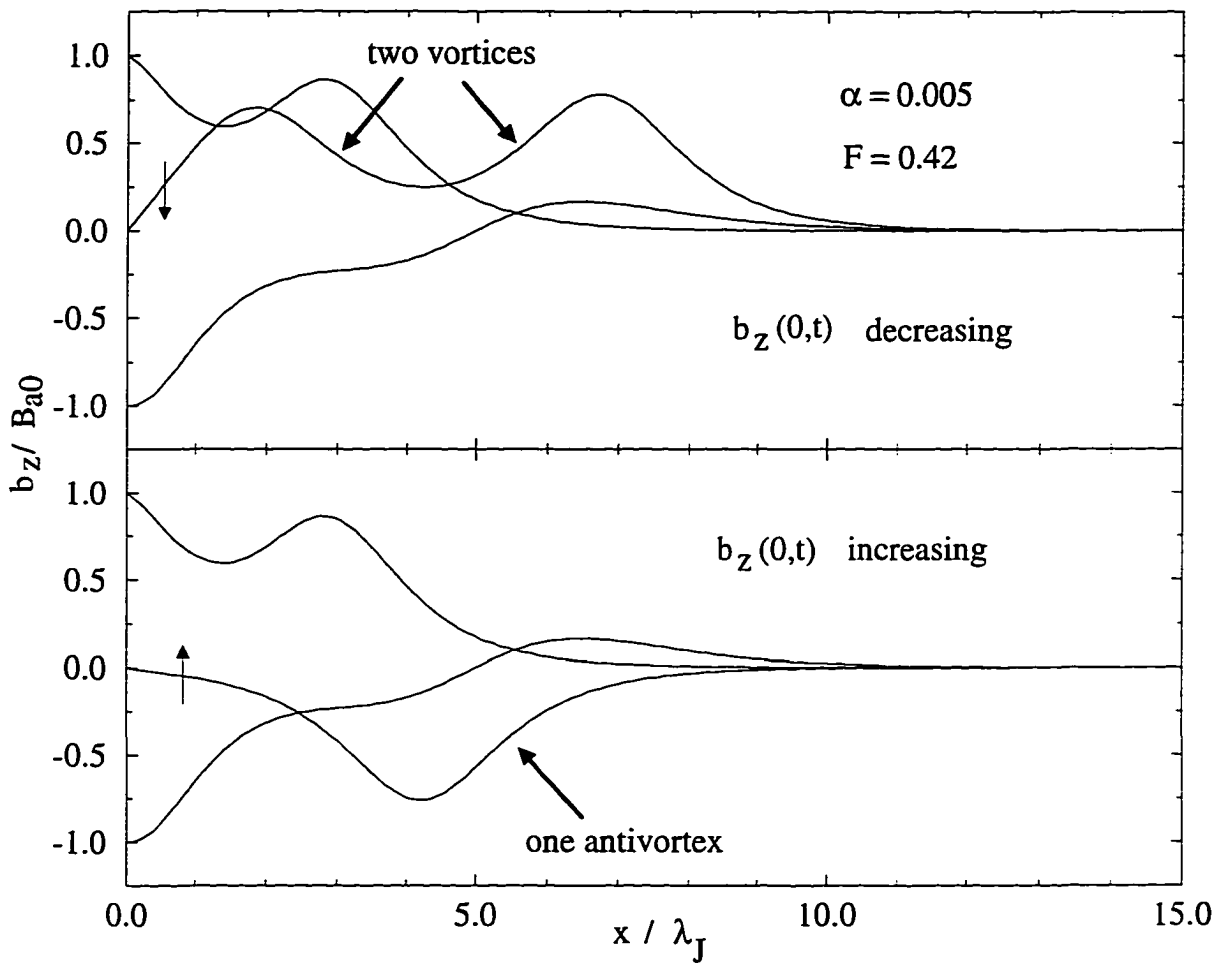

Figure 3.13 Profiles of $b_z(x,t)$ versus x for a long uniform junction with $\alpha = 0.005$ at $F = 0.42$, just after the second vortex nucleation process (feature D in Figs. 3.8 and 3.9) has occurred. The top figure corresponds to the external ac field decreasing from $+B_{a0}$ to $-B_{a0}$. The bottom figure corresponds to the external ac field increasing from $-B_{a0}$ to $+B_{a0}$. When the external field is zero, there is clearly either a pair of vortices (top figure) or a single antivortex (bottom figure) trapped in the junction. The field-increasing and field-decreasing profiles of $b_z(x)$ are no longer mirror images of each other.

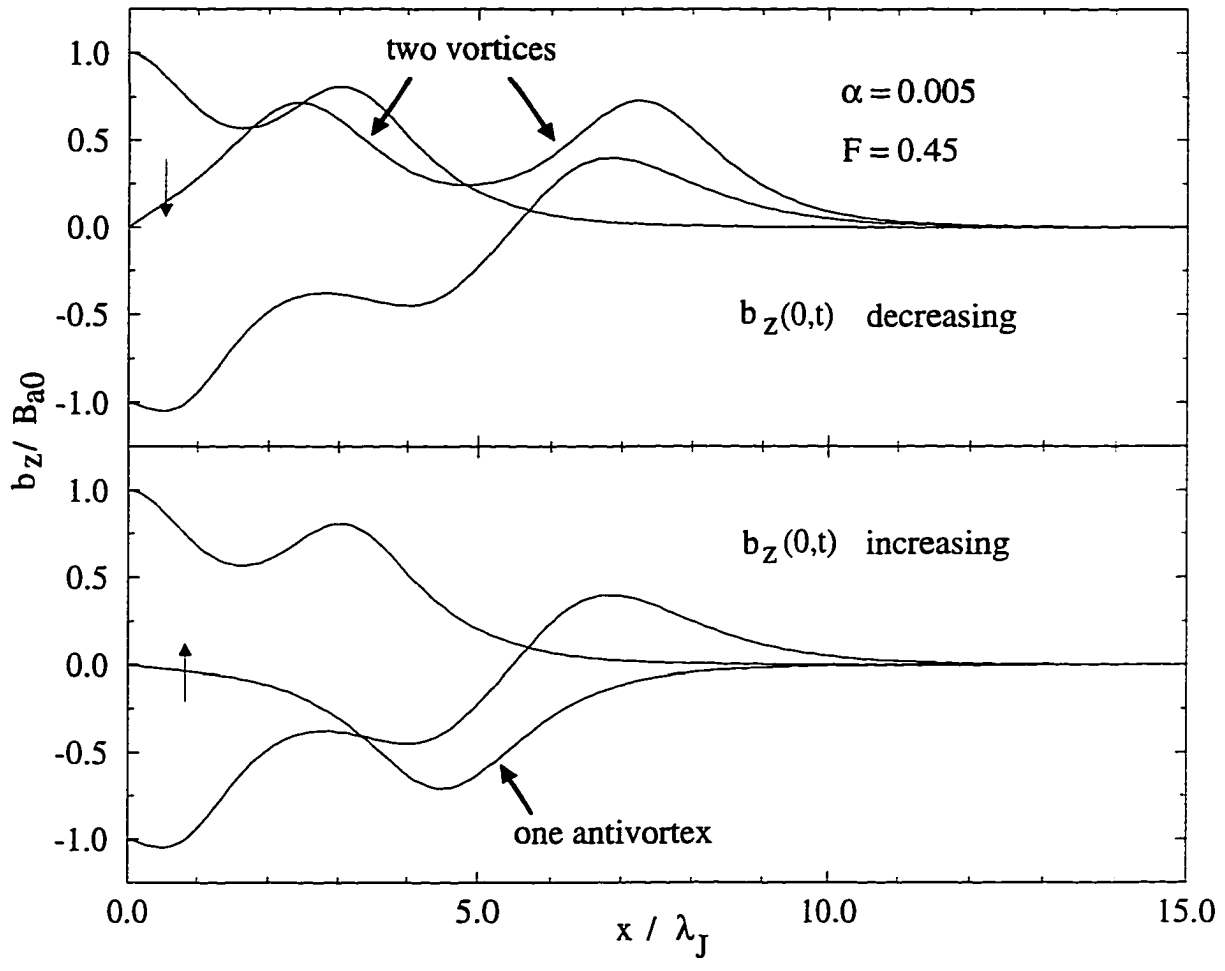

Figure 3.14 Profiles of $b_z(x,t)$ versus x, for a long uniform junction with $\alpha = 0.005$ at $F = 0.45$, just before the third vortex nucleation process (feature E in Figs. 3.8 and 3.9) will occur. The top figure corresponds to the external ac field decreasing from $+B_{a0}$ to $-B_{a0}$. The bottom figure corresponds to the external ac field increasing from $-B_{a0}$ to $+B_{a0}$. When the external field is zero there is clearly either a pair of vortices (top figure) or a single antivortex (bottom figure) trapped in the junction, and the field-increasing and field-decreasing profiles of $b_z(x)$ still are not mirror images of each other.

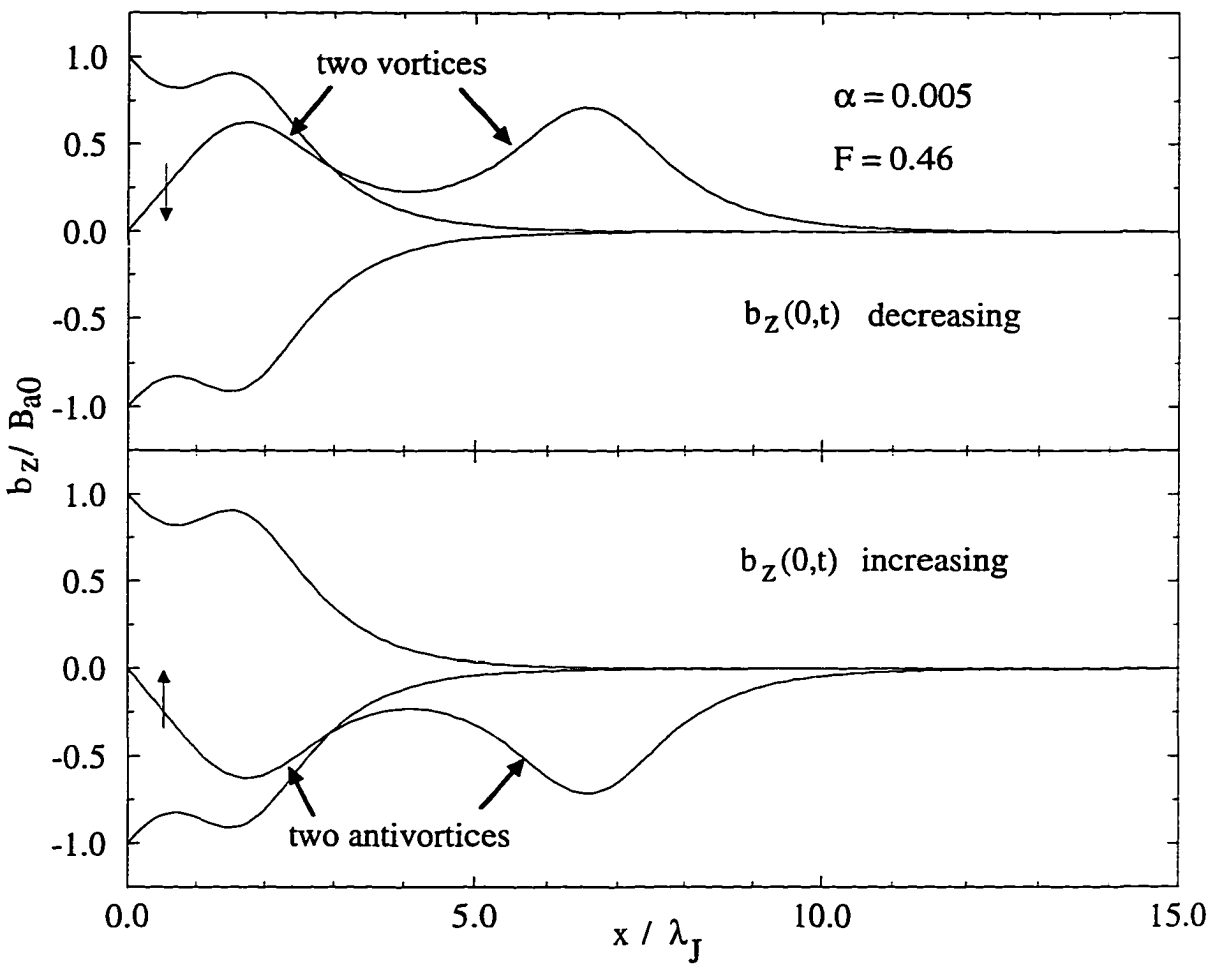

Figure 3.15 Profiles of $b_z(x,t)$ versus x for a long uniform junction with $\alpha = 0.005$ at $F = 0.46$, just after the third vortex nucleation process (feature E in Figs. 3.8 and 3.9) has occurred. The top figure corresponds to the external ac field decreasing from $+B_{a0}$ to $-B_{a0}$. The bottom figure corresponds to the external ac field increasing from $-B_{a0}$ to $+B_{a0}$. When the external field is zero there is clearly either a pair of vortices (top figure) or a pair of antivortices (bottom figure) trapped in the junction, and the field-increasing and field-decreasing profiles of $b_z(x)$ again are mirror images of each other.

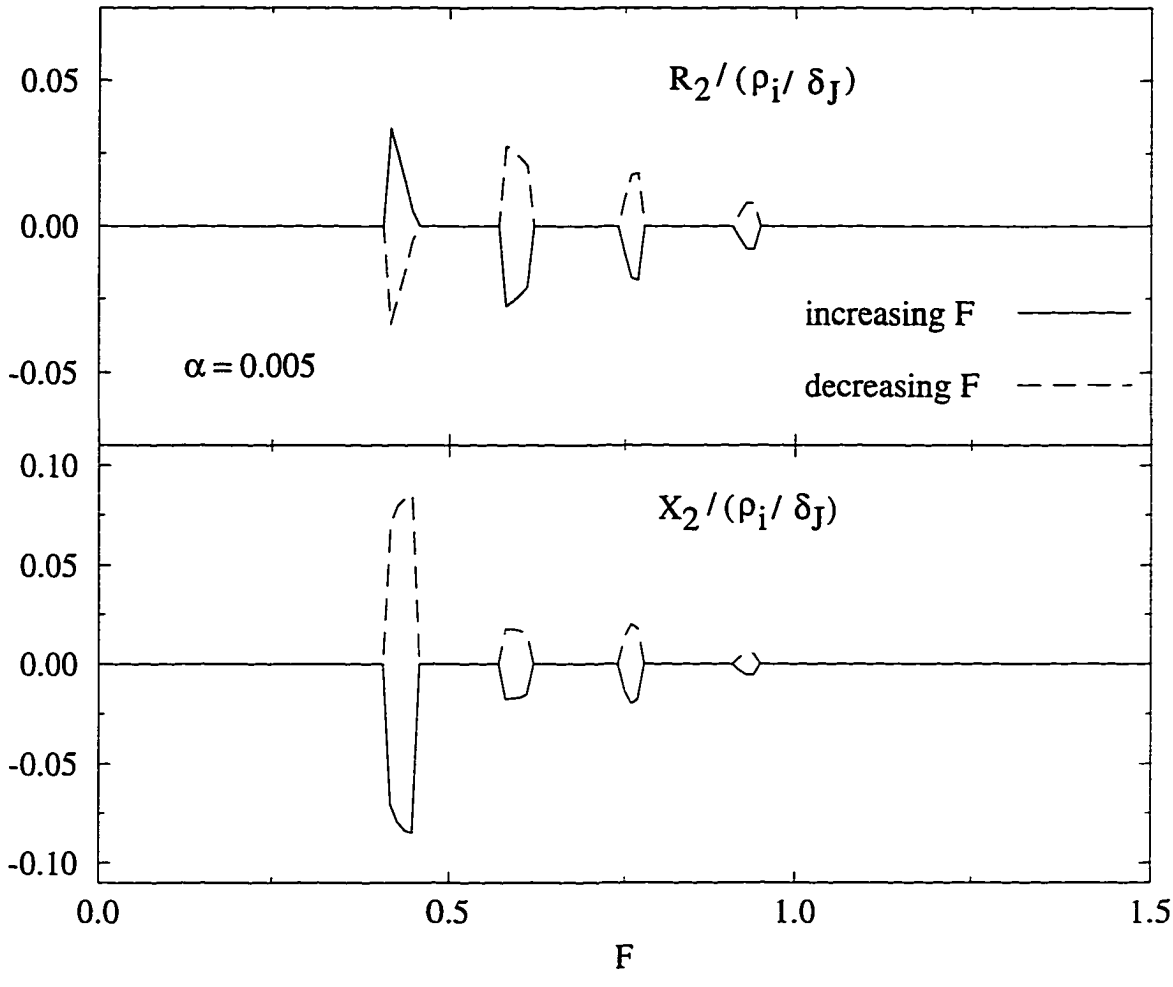

Figure 3.16 Second harmonics R_2 and X_2 versus F, for a long uniform junction with $\alpha = 0.005$. These harmonics are generated by the asymmetry in the field profiles between the two half periods of oscillation of the external field, as illustrated in Figs. 3.13 and 3.14. The signs of these harmonics depends on whether it is a vortex nucleation process (increasing F) or a vortex exit process (decreasing F). The difference in sign occurs because the direction of the asymmetry (more vortices than antivortices or vice versa) depends on the previous history of the junction.

3.4 Harmonic generation by a long Josephson junction in a superconducting slab

3.4.1 Alternating field case

In this section I consider a long junction in a superconducting slab of width W (see Fig. 3.17). The thickness of the barrier region is d_i and its resistivity is ρ_i. There is an applied magnetic field $\mathbf{B_a} = B_{a0}\sin(\omega t)\hat{z}$, and the Josephson penetration depth for the junction is $\lambda_J = \sqrt{\phi_0/(2\pi\mu_0 J_0 d)}$ where $d = 2\lambda + d_i$. The gauge-invariant phase difference $\Delta\gamma(x,t)$ is again given by Eq. (3.23) which reduces to Eq. (3.25) when $\omega \ll \omega_p$. The boundary conditions are

$$\left[\frac{\partial}{\partial x'}\Delta\gamma(x',t')\right]_{x'=0,W'} = -2\pi F\sin(2\pi t')\,, \tag{3.42}$$

where $W' = W/\lambda_J$.

In general Eq. (3.23) must be solved numerically. It is interesting to investigate the effect of the width of the sample on the surface impedance and harmonic generation. It is expected that the results of Sec. 3.3 will be recovered in the limit $W' \gg 1$; however, one would not expect to obtain results analogous to those of Sec. 3.2 for the limit $W' \ll 1$ because there is no net transport current. When $W' \ll 1$ the solution for $\Delta\gamma(x',t')$ is given by

$$\Delta\gamma(x',t') = \pi W' F(1 - 2x'/W')\sin(2\pi t')\,. \tag{3.43}$$

The resulting electric field at the surface is

$$e_y(x' = 0,t') = H_{a0}\left(\frac{\rho_i}{\delta_J}\sqrt{\pi\alpha}W'\right)\cos(2\pi t')\,, \tag{3.44}$$

therefore, $X_1 = (\rho_i/\delta_J)\sqrt{\pi\alpha}W'$ and all other coefficients are zero. In the opposite limit $W' \gg 1$ the coefficients should obviously be given by the results of Sec. 3.3.

Figure 3.18 shows R_1 and X_1 versus F, $\alpha = 0.005$, for several different values of W'. One interesting feature is that the reactance $X_1/(\rho_i/\delta_J)$ saturates at high fields to a value greater than one for intermediate values of W'. This occurs because at intermediate values, $W'/2$ is nearly equal to the Josephson skin depth $\delta_J/\lambda_J \simeq 8$. Figure 3.19 shows R_3 and X_3 versus F for the same values of W'. It is evident from the figure that there are essentially no third harmonics generated in a very small junction placed in an external field. It was also found that second harmonic generation does not occur until the juntion is sufficiently large ($W' \gtrsim 15$). This is not surprising since the second harmonics seem to be generated by the dynamics and interactions of Josephson vortices.

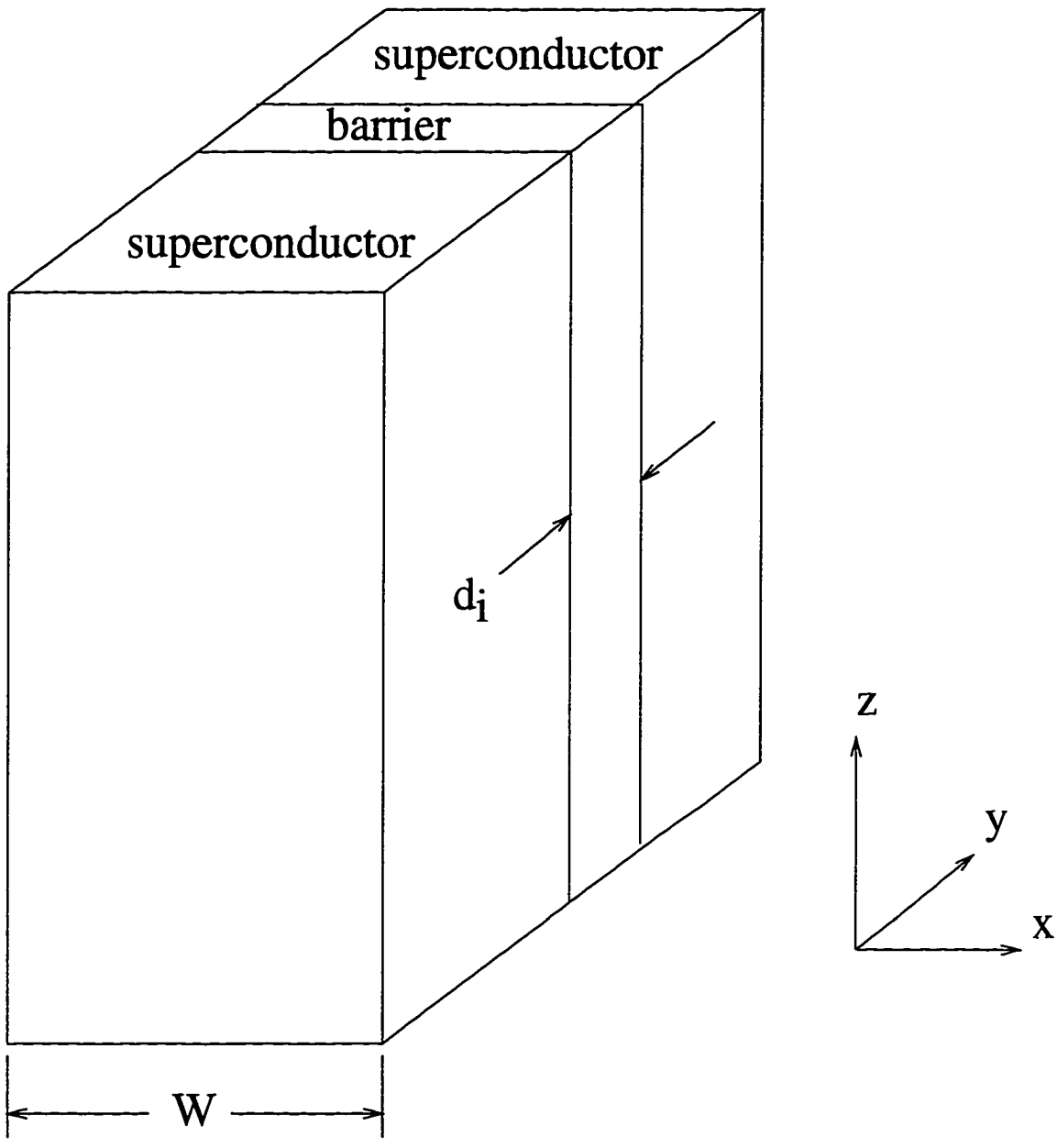

Figure 3.17 Geometry of a long Josephson junction in a slab of width W. The region $0 < x < W$, excluding a slab of thickness d_i centered on the $x - z$ plane, is occupied by a superconductor with London penetration depth λ. The slab-shaped barrier region is characterized by a resistivity ρ_i.

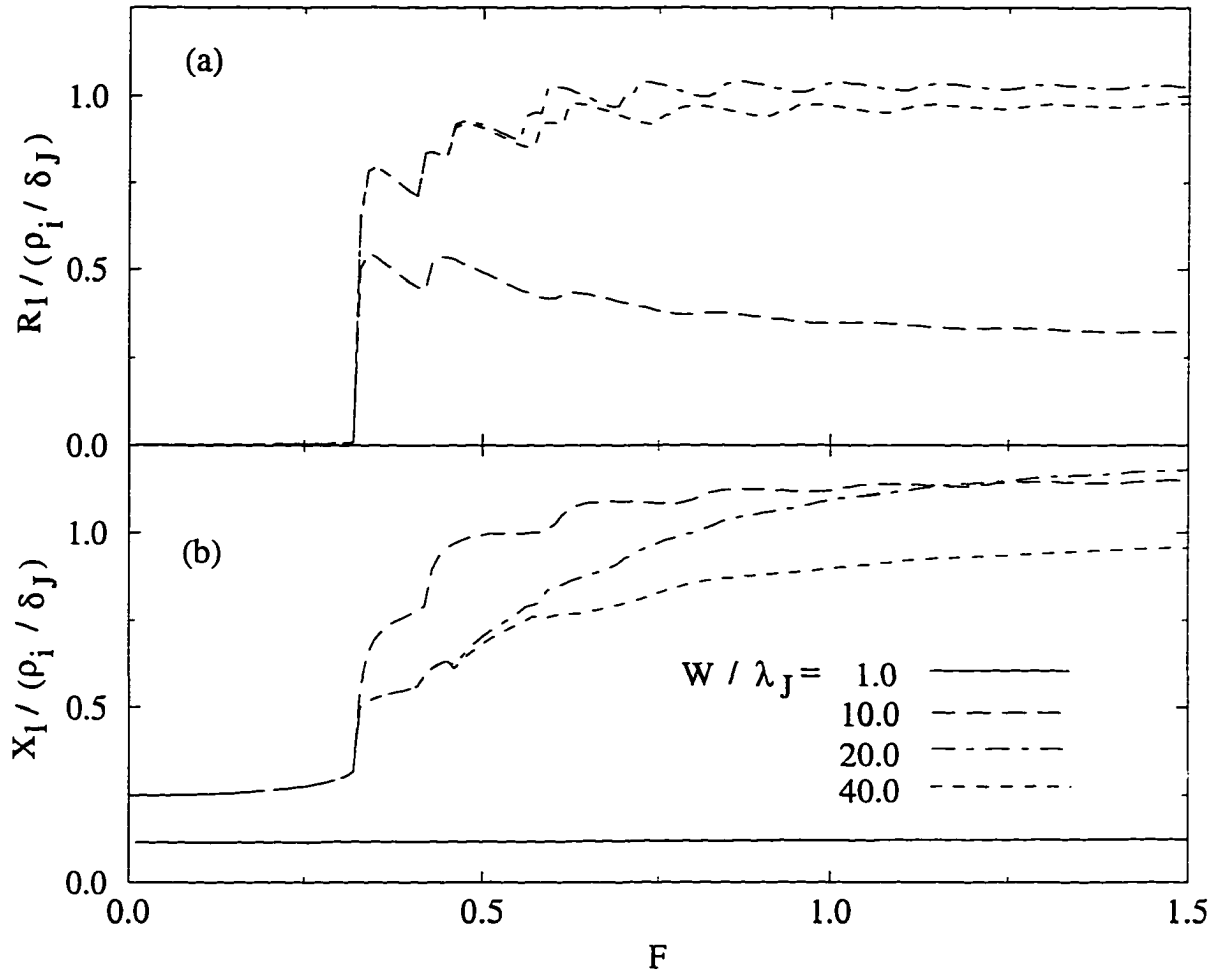

Figure 3.18 Resistance R_1 (a) and reactance X_1 (b), versus F, of a uniform junction of width W and damping parameter $\alpha = 0.005$, in an applied ac field. When $W/\lambda_J \simeq 1$, $R_1 \simeq 0$ and X_1 is nearly constant. When $W/\lambda_J \gg 1$, R_1 and X_1 approach the curves pictured in Fig. 3.8 for a long junction with $\alpha = 0.005$. The curves do not change monotonically as W/λ_J changes from being very small to being very large.

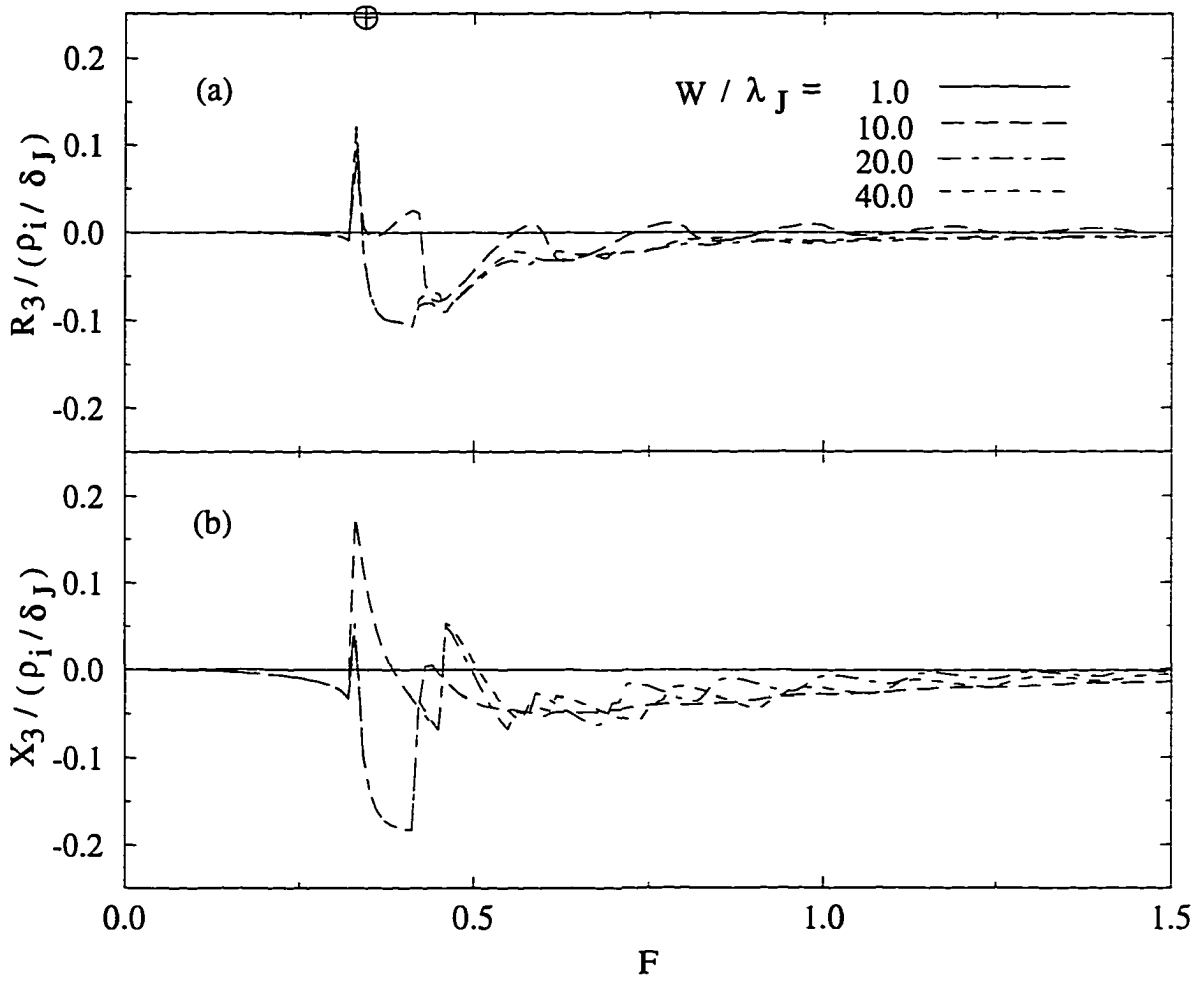

Figure 3.19 Third harmonics R_3 (a) and X_3 (b), versus F, of a uniform junction of width W and damping parameter $\alpha = 0.005$, in an applied ac field. When $W/\lambda_J \simeq 1$, $R_3 \simeq 0$ and $X_3 \simeq 0$. When $W/\lambda_J \gg 1$, R_3 and X_3 approach the curves pictured in Fig. 3.9 for a long junction with $\alpha = 0.005$. The curves do not change monotonically as W/λ_J changes from being very small to being very large.

3.4.2 Alternating current case

In this section I consider the junction pictured in Fig. 3.17 carrying a sinusoidal transport current per unit height in the y direction. The transport current creates a magnetic field external to the slab given by

$$B_z(x',t') = \begin{cases} +B_{a0}\sin(2\pi t'), & x' < 0, \\ -B_{a0}\sin(2\pi t'), & x' > W'. \end{cases} \tag{3.45}$$

Using Eq. (3.25) with the boundary conditions

$$\frac{\partial \Delta\gamma(x',t')}{\partial x'} = \begin{cases} -2\pi F\sin(2\pi t'), & x' = 0, \\ +2\pi F\sin(2\pi t'), & x' = W', \end{cases} \tag{3.46}$$

$\Delta\gamma(x',t')$ can be calculated and the Fourier coeffiecients R_n and X_n determined. In the limit $W' \ll 1$ Eqs. (3.25) and (3.46) reduce to Eq. (3.7) in the RSJ model with the identifications $\alpha = \varepsilon$ and $4\pi F/W' = I$. In the opposite limit $W' \gg 1$ one would expect to recover the results of Sec. 3.3 for a long junction in a half space.

Figure 3.20 shows R_1 and X_1 and Fig. 3.21 shows R_3 and X_3 versus F, $\alpha = 0.005$, for several values of W'. It is interesting to note that for even for W' as large as 10, many of the features exhibited are similar to those of Sec. 3.2 for the RSJ model. One difference, however, is that for the RSJ model X_1 oscillates around zero and here it oscillates around a positive value. Once again there are no second harmonics generated until $W' \gtrsim 15$.

3.5 Harmonic generation by a long Josephson junction in a circular wire

In this section I consider a long junction in a superconducting wire of radius a (see Fig. 3.22) carrying a transport current, $I_T = I_{T0}\sin\omega t$, in the z direction. The transport current creates a tangential magnetic field [$B_\phi = (\phi_0/2\pi d)\partial\Delta\gamma/\partial\rho$] at the surface of the wire given by

$$B_\phi(\rho' = a', t') = B_{a0}\sin(2\pi t'), \tag{3.47}$$

where $a' = a/\lambda_J$ and $B_{a0} = \mu_0 I_{T0}/2\pi a$. In cylindrical coordinates, the equation for $\Delta\gamma(\rho',t')$ is

$$\frac{\partial^2\Delta\gamma}{\partial\rho'^2} + \frac{1}{\rho'}\frac{\partial\Delta\gamma}{\partial\rho'} - \alpha\frac{\partial\Delta\gamma}{\partial t'} = \sin\Delta\gamma, \tag{3.48}$$

with boundary conditions

$$\left[\frac{\partial\Delta\gamma}{\partial\rho'}\right]_{\rho'=0} = 0, \tag{3.49}$$

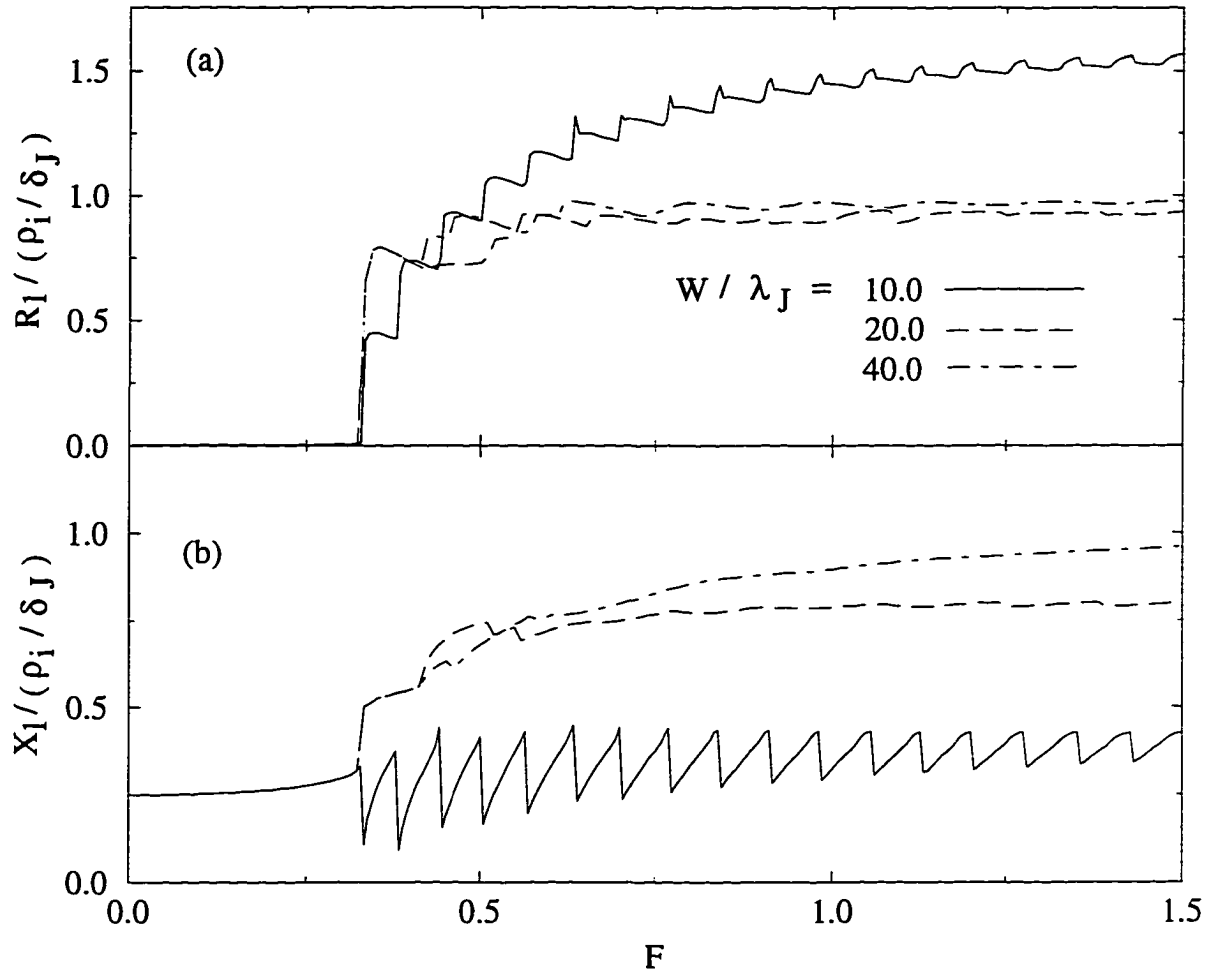

Figure 3.20 Resistance R_1 (a) and reactance X_1 (b), versus F, of a uniform junction of width W and damping parameter $\alpha = 0.005$, carrying a transport current. When $W/\lambda_J = 10$, the curves are similar to those obtained from the RSJ model with a small damping parameter. When $W/\lambda_J \gg 1$, R_1 and X_1 approach the curves pictured in Fig. 3.8 for a long junction with $\alpha = 0.005$. The curves do not change monotonically as W/λ_J changes from being very small to being very large.

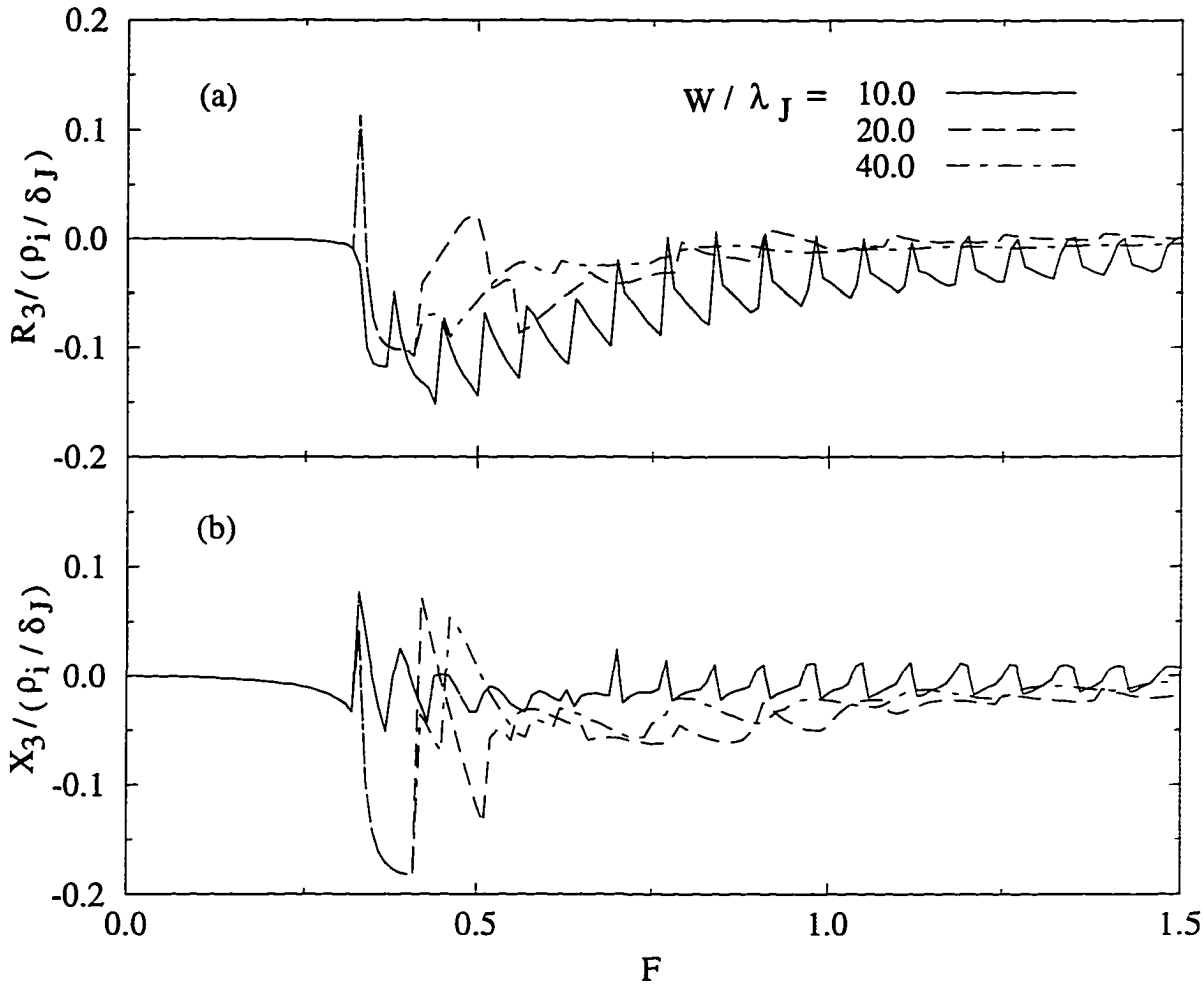

Figure 3.21 Third harmonics R_3 (a) and X_3 (b), versus F, of a uniform junction of width W and damping parameter $\alpha = 0.005$, carrying a transport current. When $W/\lambda_J = 10$, the curves are similar to those obtained from the RSJ model with a small damping parameter. When $W/\lambda_J \gg 1$, R_3 and X_3 approach the curves pictured in Fig. 3.9 for a long junction with $\alpha = 0.005$.

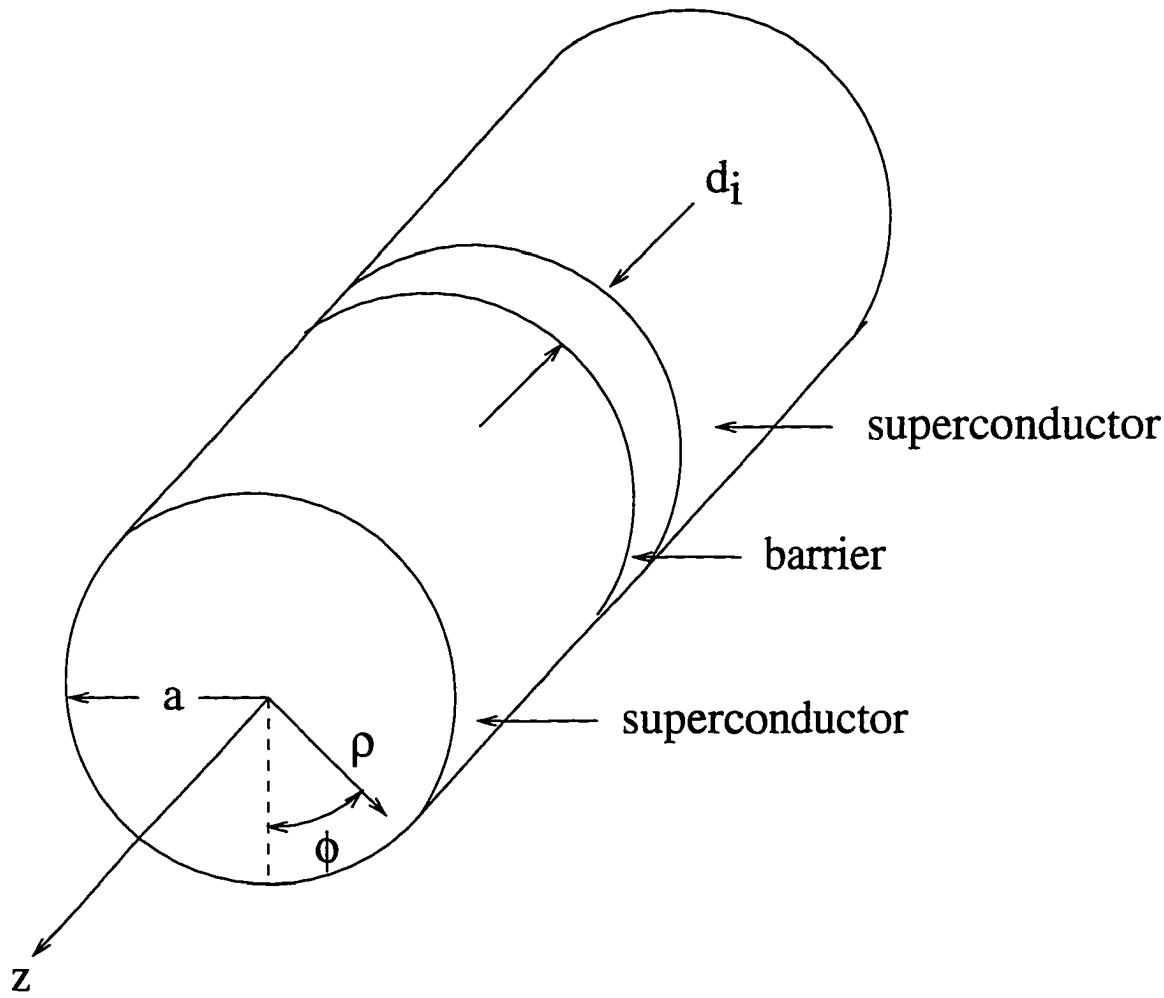

Figure 3.22 Geometry of a long Josephson junction in a circular wire of radius a. The region $0 < \rho < a$, excluding a slab of thickness d_i centered on the $\rho - \phi$ plane, is occupied by a superconductor with London penetration depth λ. The slab-shaped barrier region is characterized by a resistivity ρ_i.

and

$$\left[\frac{\partial \Delta\gamma}{\partial \rho'}\right]_{\rho'=a'} = 2\pi F \sin(2\pi t') \,. \tag{3.50}$$

In the limit $a' \ll 1$ Eqs. (3.48-3.50) reduce to Eq. (3.7) for the RSJ model with the identifications $\alpha = \varepsilon$ and $2\pi F/a' = I$. In the opposite limit $a' \to \infty$ the results of Sec. 3.3 should be realized because the second term on the left hand side of Eq. (3.48) will go to zero, and Eq. (3.48) will reduce to Eq. (3.25).

Figure 3.23 shows R_1 and X_1 and Fig. 3.24 shows R_3 and X_3 versus F, $\alpha = 0.005$, for several values of a'. Once again even in the intermediate regime, $a' = 10$, many of the features are similar to those seen in the RSJ model of Sec. 3.2. Once again, however, X_1 oscillates around a positive value rather than around zero. As in the slab geometry, second harmonics are not generated until $a' \gtrsim 15$. Figure 3.25 shows R_2 and X_2 for $a' = 40.0$ and $\alpha = 0.005$. It is interesting that the curves in Fig. 3.25 are markedly different from those in Fig. 3.16. This is in contrast to the slab geometry where the limit $W' \to \infty$ is approached much more quickly. This difference can be attributed to the difference between the dynamics of ring fluxons and straight-line fluxons.

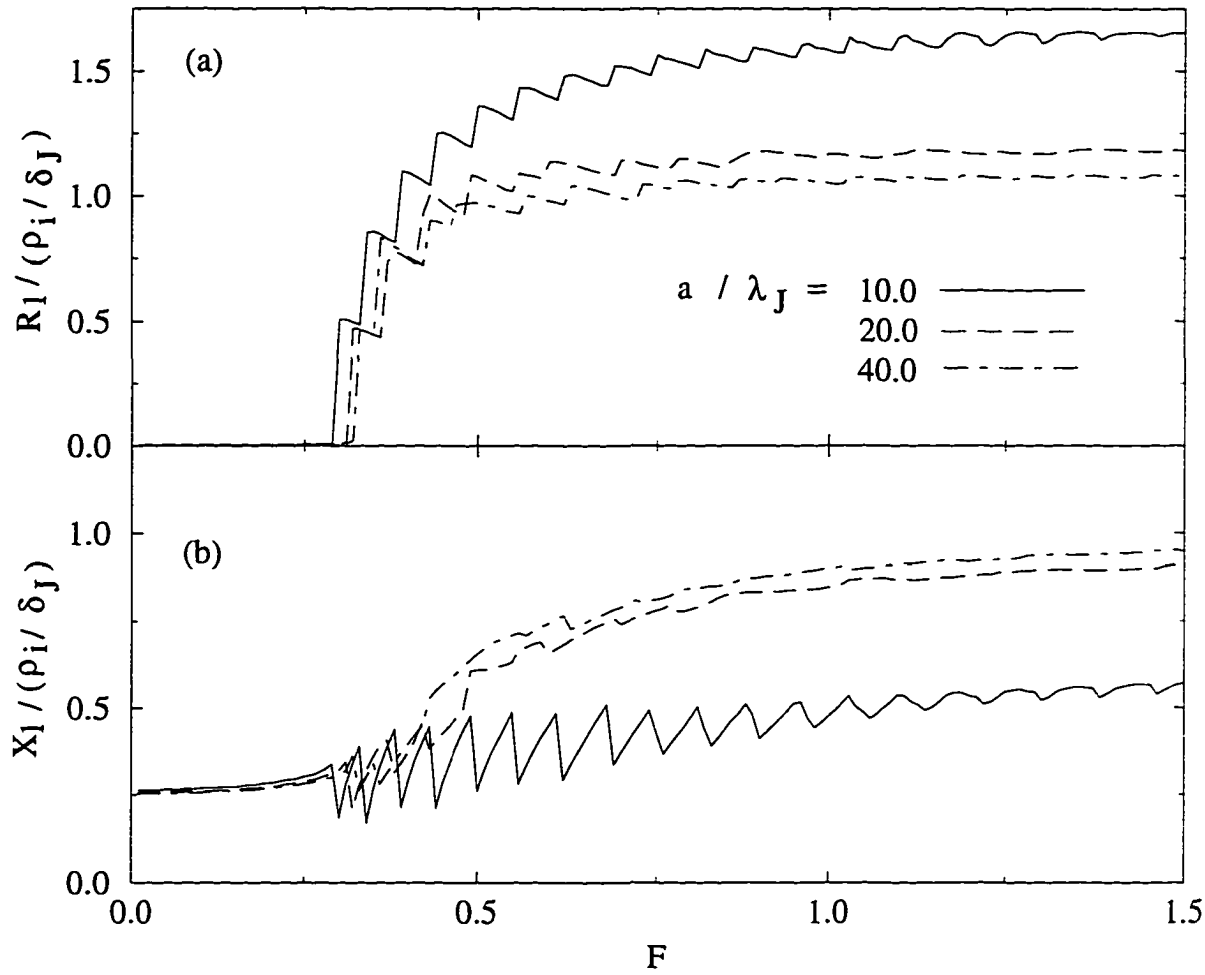

Figure 3.23 Resistance R_1 (a) and reactance X_1 (b), versus F, of a uniform, circular junction of radius a and damping parameter $\alpha = 0.005$, carrying a transport current. When $a/\lambda_J = 10$, the curves are similar to those obtained from the RSJ model with a small damping parameter.

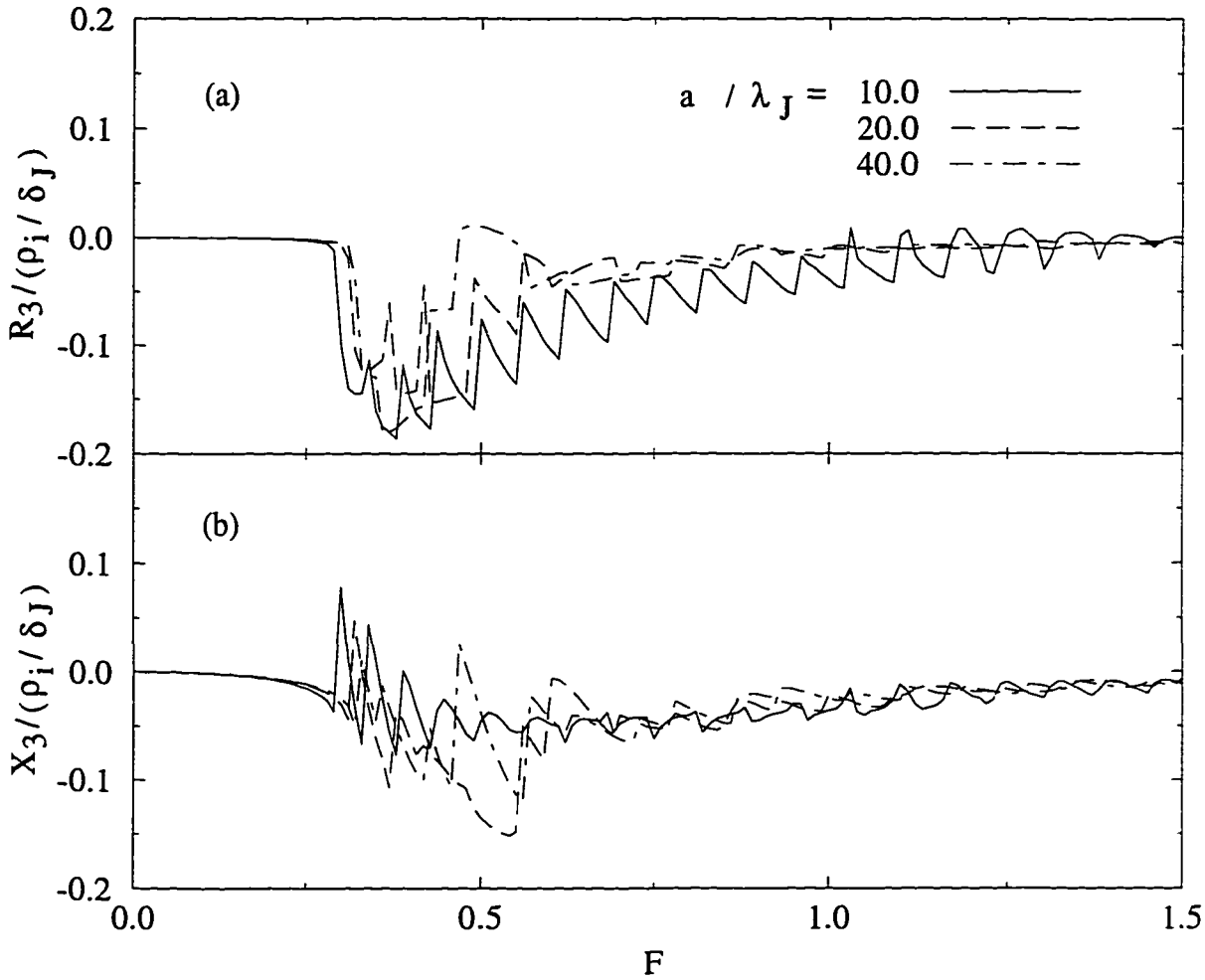

Figure 3.24 Third harmonics R_3 (a) and X_3 (b), versus F, of a uniform, circular junction of radius a and damping parameter $\alpha = 0.005$, carrying a transport current. When $a/\lambda_J = 10$, the curves are similar to those obtained from the RSJ model with a small damping parameter.

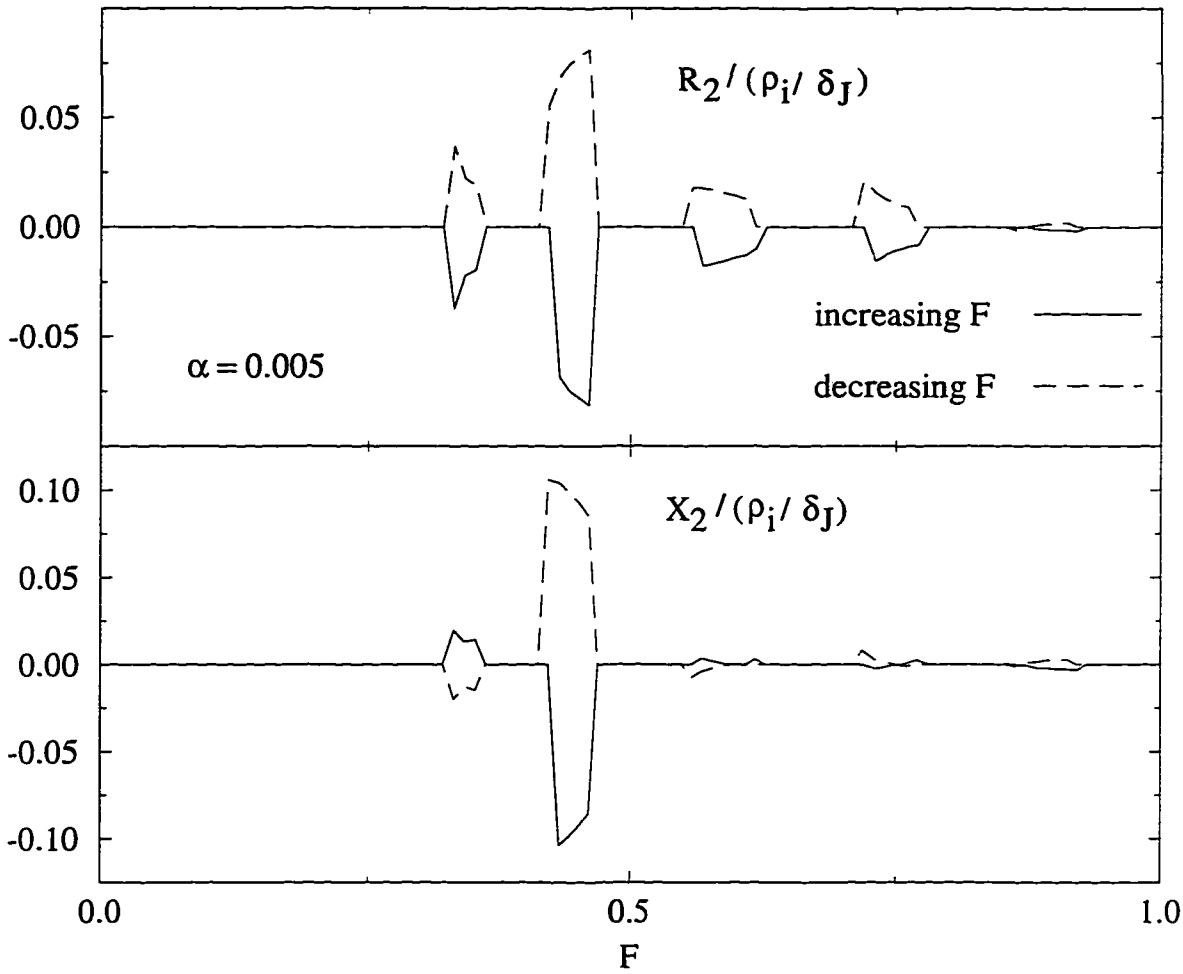

Figure 3.25 Second harmonics R_2 and X_2 versus F, for a uniform junction in a round wire with $a/\lambda_J = 40.0$ and $\alpha = 0.005$. The signs of these harmonics depends on whether F is increasing or decreasing (the previous history of the junction). These curves are significantly different from those of Fig. 3.16 due to the difference in geometry between the two cases.

4 SUMMARY

4.1 Nonlinearities due to flux pinning

The nonlinear response, caused by vortex pinning and hysteresis, of a hard type-II superconductor was investigated in both the parallel and perpendicular geometries. The surface impedance was found to be proportional to the amplitude of the applied magnetic field. This is in stark contrast to convential metals which have a field-independent surface impedance. The resistance and reactance of an elliptical wire and a thin-film strip, carrying an ac transport current, were calculated analytically. For small current amplitudes, the resistance and reactance were found to be proportional to the current amplitude in an elliptical wire, and to the square of the current amplitude in a strip. Analytical expressions were also found for the third harmonics, and all even harmonics were found to be zero. The third-order intermodulation products were calculated numerically. An analytical formula was derived for the input power at the third-order intercept for harmonic generation, in a coaxial-type strip line, in terms of the width, length, characteristic impedance, and critical current density. From this formula, scaling rules for the change in the third-order intercept, upon changes in various parameters (length, width, and temperature), was obtained and compared with experimental results. The agreement between theory and experiment was found to be excellent with regard to the width dependence, and fair with regard to the length and temperature dependence.

4.2 Nonlinearities due to weak links

The nonlinear response of both small and long, uniform Josephson junctions to ac fields and currents, with frequencies much smaller than the Josephson plasma frequency, was analyzed. For the case of long junctions various geometries were considered including a half space, a slab, and a round wire. For both small and long junctions, the behavior was found to be strongly dependent on the strength of the resistive damping. For small damping, sharp features were found in the resistive, reactive, and higher harmonic responses as a function of the ac field or current amplitude. In the case of small junctions,

the sharp features are caused by bifurcations, or 2π phase slips, in the gauge-invariant phase difference across the junction. In the case of long junctions, the sharp features are due to changes in the number of Josephson vortices in the junction. In both cases, the resistive response saturates at large current or field amplitudes. This is in contrast to the case of flux pinning where the resistive response grows with the field amplitude. Long junctions also show second harmonic generation due to asymmetric field profiles between the two half periods of oscillation of the external field. This effect appears to be related to Josephson fluxon dynamics and is not seen in smaller junctions. The signs of the second harmonics are different for increasing applied field than for decreasing applied field. The structure of the second harmonics is significantly different for a large junction in a wire than for a large junction in a slab. This difference is due to the difference in dynamics between ring fluxons and straight-line fluxons.

BIBLIOGRAPHY

A. A. Abrikosov, Zh. Eksperim. i Teor. Fiz. **32**, 1442 (1957).

F. Auracher and T. Van Duzer, J. Appl. Phys. **44**, 848 (1973).

J. Bardeen, L. N. Cooper, and J. R. Schrieffer, Phys. Rev. **108**, 1175 (1957).

C. P. Bean, Phys. Rev. Lett. **8**, 250 (1962).

G. Bednorz and K. A. Müller, Z. Phys. **B64**, 189 (1986).

E. H. Brandt and M. Indenbom, Phys. Rev. B **48**, 12893 (1993).

A. M. Campbell, IEEE Trans. Appl. Supr. **5**, 687 (1995).

C. C. Chin, D. E. Oates, G. Dresselhaus, M. S. Dresselhaus, Phys. Rev. B **45**, 4788 (1992).

J. R. Clem, in *Proceedings of the ICTPS '90 International Conference on Transport Properties of Superconductors*, edited by R. Nicolsky (World Scientific, Singapore, 1990), p. 64.

J. R. Clem, in *Magnetic Susceptibility of Superconductors and Other Spin Systems*, edited by R. A. Hein, T. L. Francavilla, and D. H. Liebenberg (Plenum Press, New York, 1992), p. 177.

J. R. Clem, in *Proceedings of the 7th International Workshop on Critical Currents in Superconductors*, edited by H. W. Weber (World Scientific, Singapore, 1994), p. 117.

J. R. Clem, M. Benkraouda, T. Pe, and J. McDonald, Chn. J. of Phys. **34**, 284 (1996).

A. T. Findikoglu, D. W. Reagor, P. N. Arendt, S. R. Foltyn, J. R. Groves, Q. X. Jia, E. J. Peterson, L. Boulaevskii, and M. P. Maley, Appl. Phys. Lett (submitted, 1996).

L. M. Fisher, V. S. Gorbachev, N. V. Il'in, N. M. Makarov, I. F. Voloshin, V. A. Yampol'skii, R. L. Snyder, S. T. Misture, M. A. Rodriguez, D. P. Matheis, V. R. W. Amarakoon, J. G. Fagan, J. A. T. Taylor, and A. M. M. Barus, Phys. Rev. B **46**, 10986 (1992).

S. Fleshler, L. T. Cronis, G. E. Conway, A. P. Malozemoff, T. Pe, J. McDonald, J. R. Clem, G. Vellego, and P. Metra, Appl. Phys. Lett. **67**, 3189 (1995).

V. L. Ginzburg and L. D. Landau, Zh. Eksperim. i Teor. Fiz. **20**, 1064 (1950).

M. A. Golosovsky, H. J. Snortland, and M. R. Beasley, Phys. Rev. B **51**, 6462 (1995).

L. P. Gorkov, Zh. Eksperim. i Teor. Fiz. **36**, 1918 (1959).

J. Halbritter, J. Appl. Phys. **68**, 6315 (1990).

J. Halbritter, J. Supercond. **8**, 691 (1995).

J. Halbritter, invited talk at 4th Symposium on High-Temperature Superconductors in High-Frequency Fields, Asilomar, CA, 1996.

J. S. Herd, D. E. Oates, and J. Halbritter, contributed paper at the Applied Superconductivity Conference, Pittsburgh, 1996.

R. P. Huebener, R. T. Kampwirth, and J. R. Clem, J. Low Temp. Phys. **6**, 275 (1972).

J. D. Jackson, *Classical Electrodynamics* (John Wiley and Sons, Inc., New York, 1975).

B. D. Josephson, Phys. Lett. **1**, 251 (1962).

H. Kamerlingh Onnes, Leiden Comm. **120b**, **122b**, **124c** (1911).

G.-C. Liang, D. Zhang, C.-F. Shih, M. E. Johansson, R. S. Withers, W. Ruby, D. E. Oates, A. C. Anderson, P. A. Polakos, P. M. Mankiewich, E. DeObaldia, and R. E. Miller, IEEE Trans. on Micro. Th. and Tech. **43**, 3020 (1995).

F. and H. London, Proc. Roy. Soc. (London) **A149**, 71 (1935).

G. B. Lubkin, Physics Today, Vol. 48, No. 3, 20 (1995).

W. Meissner and R. Ochsenfeld, Naturwissenschaften **21**, 787 (1933).

P. P. Nguyen, D. E. Oates, G. Dresselhaus, M. S. Dresselhaus, A. C. Anderson, Phys. Rev. B **51**, 6686 (1995).

W. T. Norris, J. Phys. D **3**, 489 (1970).

D. E. Oates, A. C. Anderson, and P. M. Mankiewich, J. Supercond. **3**, 251 (1990).

D. E. Oates, P. P. Nguyen, G. Dresselhaus, M. S. Dresselhaus, G. Koren, and E. Polturak, J. Supercond. **8**, 725 (1995).

M. Perpeet, M. A. Hein, H. Piel, S. Beuven, M. Siegel, and E. Sodtke, contributed paper at Applied Superconductivity, Ebinburugh, 1995.

Z.-Y Shen, *High-Temperature Superconducting Microwave Circuits* (Artech House, Boston, 1994).

S. Sridhar, Appl. Phys. Lett. **65**, 1054 (1994).

G. W. Swan, J. Math. Phys. **9**, 1308 (1968).

M. Tinkham, *Introduction to Superconductivity*, 2nd ed., (McGraw-Hill, New York, 1996).

T. Van Duzer and C. W. Turner, *Principles of Superconductive Devices and Circuits* (Elsevier North Holland, Inc., New York, 1981).

C. Wilker, Z.-Y. Shen, P. Pang, W. L. Holstein, and D. W. Face, IEEE Trans. Appl. Supr. **5**, 1665 (1995).

L. M Xie, J. Wosik, and J. C. Wolfe, Phys. Rev. B **54**, 15494 (1996).

E. Zeldov, J. R. Clem, M. McElfresh, and M. Darwin, Phys. Rev. B **49**, 9802 (1994).

Z. Zhai, H. Srikanth, S. Sridhar, A. Erb, E. Walker, and R. Flukiger, proceedings of M2 HTSC-V, Bejing, 1996.